Search for populations of unresolved sources of high energy neutrinos with the ANTARES neutrino telescope

Rodrigo Gracia Ruiz

To cite this version:

Rodrigo Gracia Ruiz. Search for populations of unresolved sources of high energy neutrinos with the ANTARES neutrino telescope. Astrophysics [astro-ph]. Université Sorbonne Paris Cité, 2016. English. NNT : 2016USPCC150 . tel-01662335

HAL Id: tel-01662335

https://theses.hal.science/tel-01662335

Submitted on 13 Dec 2017

Thèse préparée
à l'Université Paris Diderot
Ecole doctorale STEP'UP — ED N°560
Laboratoire AstroParticule et Cosmologie

Search for populations of unresolved sources of high energy neutrinos with the ANTARES neutrino telescope.

---

présentée et soutenue publiquement le
23 novembre 2016 par

Rodrigo G. Ruiz

Pr. Etienne PARIZOT	Président du jury
Pr. Antoine KOUCHNER	Directeur de thèse
Dr. Isabelle L'HENRY-YVON	Rapporteur
Pr. Annarita MARGIOTTA	Rapporteur
Dr. Juan Antonio AGUILAR	Examinateur
Dr. Bruny BARET	Examinateur
Dr. Dorothea SAMTLEBEN	Examinateur

Résumé

La physique des astroparticules est un domaine de la physique lié a l'étude des phénomènes astrophysiques les plus violents de l'univers comme les trous noirs dans les galaxies actives (AGN) ou les sursauts de rayons gamma (GRB), qui émettent plusieurs messagers cosmiques comme des neutrinos, des ondes gravitattionnelles, des rayonnements électromagnétiques et des particules chargées. Pour mieux comprendre ces objets une approche multi-messagers est mise en place au sein de laquelle, l'observation de neutrinos cosmiques est devenue un enjeu majeur. Grâce à ses caractéristiques physiques, les neutrinos permettent d'ouvrir une nouvelle fenêtre d'observation sur l'univers lointain et de mieux comprendre les phénomènes physiques qui se produisent dans les environnements astrophysiques les plus denses.

Cette thèse comporte trois grandes parties. La première partie est composée par trois chapitres consacrés au contexte scientifique dans lequel se développe le reste de la thèse. Dans le premier chapitre sont décrites les motivations scientifiques de la recherche de neutrinos cosmiques de haute énergie. Puis, dans le chapitre 2 sont décrites les caractéristiques principales des noyaux actifs de galaxie (AGN) comme sources potentielles de neutrinos. Ces sources ont été choisies comme objets "test" dans la recherche de sources potentielles. Enfin, le troisième chapitre est consacré au principe de détection et aux principaux résultats des télescopes à neutrinos en opération. La deuxième partie de la thèse est consacrée à la description technique du télescope à neutrinos ANTARES, et est composée de deux chapitres. Le chapitre 4 décrit le télescope ANTARES, l'acquisition et la sélection des données. Dans la dernière partie de ce chapitre, le travail effectué pour mesurer la perte d'efficacité des phpotomultiplicateurs (PMTs) en utilisant la ligne de base des taux de comptage des signaux est décrite. Le chapitre 5 est consacré à la simulation Monte Carlo. Les différents programmes de simulation utilisés par la collaboration ANTARES sont présentés, et les différents processus simulés sont décrits. Une contribution au programme officiel de génération des événements est décrite, relative à l'implémentation de la propagation des taus ainsi que l'ajout dans la simulation de 15 canaux de décroissance.

La troisième partie est consacrée à la recherche de signaux cosmiques potentiels dans les événements enregistrés par ANTARES. Elle comporte 4 chapitres. Le chapitre 6 est une description de la méthode de recherche de signal, le chapitre 7 est dédié présente les principes d'une analyse fondée sur une fonction de corrélation à 2 points qui sera effectuée dans le chapitre 9 afin de chercher un éventuel excès de neutrinos cosmiques dont la distribution spatiale attendue est différente de celle des neutrinos atmosphériques. Cette méthode est particulièrement adaptée pour détecter l'effet collectif produit par des populations de sources ponctuelles faibles. Le chapitre 8 décrit la simulation du flux de neutrinos émis par des sources de type AGN. En utilisant la fonction de luminosité pour plusieurs classes d'AGN obtenu à partir d'observations en rayonnement X de ces objets et l'acceptance d'ANTARES, un ensemble de simulations de neutrinos provenants de populations d'AGN est obtenu en fonction de deux paramètres liés au nombre d'AGN dans la population et à leurs luminosités. L'analyse de ces événements avec la fonction de corrélation à deux points est détaillée dans le chapitre 9.

Summary

Astroparticle physics is a branch of physics related to the study of the most violent astrophysical phenomena in the Universe such as Active Galactic Nuclei (AGN) or Gamma Ray Bursts (GRB), which emit different cosmic messengers such as neutrinos, gravitational waves, electromagnetic radiation and charged particles. A proper understanding of these objects involves then a multi-messenger approach, in which neutrinos play a fundamental role. Thanks to their physical properties, neutrinos allow us to explore the physical phenomena produced in the densest astrophysical environments and to observe the Universe at large distances.

This thesis is divided into three main parts. The first part is composed by three chapters dedicated to the scientific context in which the rest of the thesis is developed. In the first chapter, the scientific motivations for the search of high energy cosmic neutrinos are described. In chapter 2, a description of the main properties of AGN are given. These sources have been chosen as "test" objects in the research of potential neutrino sources. Finally, the third chapter is dedicated to the detection principle and main results of the currently operating neutrino telescopes. The second part of the thesis is dedicated to the technical description of the ANTARES neutrino telescope, and composed of two chapters. Chapter 4 describes the ANTARES telescope, the data acquisition and the data selection. In the last part of this chapter, the work made to measure the efficiency loss of the photomultipliers (PMTs) by using the baseline rates is described. Chapter 5 is dedicated to the Monte Carlo simulations. The different simulation packages used by the ANTARES collaboration are presented, and the different simulated processes are described. A contribution to the official package for the generation of neutrino interactions, relative to the implementation of the propagation and decay of the tau leptons, is described.

The third part is dedicated to the search of potential cosmic signals in the events recorded by ANTARES. It comprises four chapters. Chapter 6 is a description of the signal search method, chapter 7 presents the principles of an analysis based on a 2 point correlation function that will be applied in chapter 9 with the purpose of searching for an excess of

cosmic neutrinos characterized by an expected spatial distribution which is different from that of atmospheric neutrinos. This method is well suited for the detection of the collective effect produced by populations of weak point-like sources. Chapter 8 describes the simulation of the neutrino flux emitted by AGN. By using the luminosity function for different AGN classes obtained from X-ray observations, and the ANTARES acceptance, neutrinos coming from AGN populations are simulated as a function of two parameters which are related to the number of sources in the population, and to their luminosities. The analysis of these populations with the 2 point correlation function is detailed in chapter 9.

Contents

Part I

Scientific Motivation

Chapter 1

High energy neutrino astronomy

1.1 Introduction

A remarkable technological development took place during the XX$^{\text{th}}$ Century, after which the sky can be observed through the detection of electromagnetic radiation along different regions of the electromagnetic spectrum, and also through the detection of cosmic rays, neutrinos and gravitational waves. The field of astroparticle physics is related to the study of the most violent events in the Universe through a multi-messenger approach. In this context, the detection of high energy cosmic neutrinos has become a particularly important subject, since due to their physical properties they are unique probes for exploring the physical processes that take place in dense and remote astrophysical environments, which are likely to be opaque to photons or other particles.

The first steps towards neutrino astronomy were given in the late 1960s with the detection of solar neutrinos in the MeV range by the Homestake experiment which provided a direct confirmation of the nuclear mechanisms by which energy is produced in the core of the Sun, and which also allowed to study the fundamental physical properties of neutrinos [22]. Around 20 years later, in 1987, the detection of 25 neutrinos in a time window of 12 s coming from the supernova 1987A was another important step in neutrino astronomy, since it provided fundamental information for the understanding of the stellar evolution, as well as new constrains on the physical properties of neutrinos [76]. These pioneering observations were awarded with the Nobel prize in physics in the year 2002.

The detection of cosmic neutrinos from sources further away from the Earth and at higher energies remains a challenge for the astroparticle physics community, since the associated fluxes are weaker by several orders of magnitude (see figure 1.1). It is the main goal of the new generation of neutrino telescopes which being sensitive to higher energies ($E_\nu >$TeV), open a window for the detection of cosmic neutrino sources whose existence is proven by the observation of ultra high energy ($E > 10^{19}$ eV) cosmic rays (UHECR) and by the observation of an extraterrestrial flux of high energy neutrinos by the IceCube neutrino telescope.

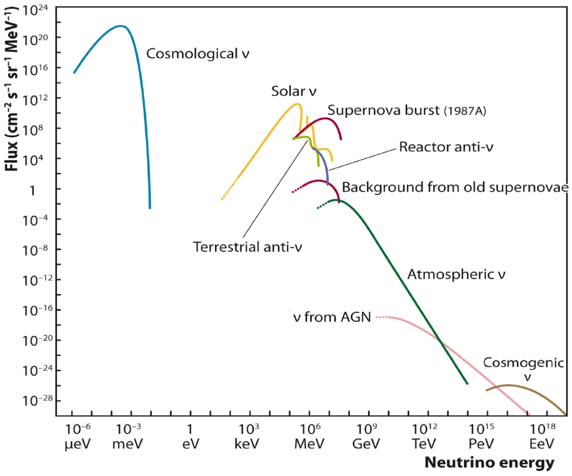

Figure 1.1: Spectrum of neutrinos produced in different sources in the Universe.

The rest of this chapter provides a general presentation of neutrino astronomy, including the main scientific motivations.

1.2 Scientific motivations

1.2.1 The origin of ultra high energy cosmic rays

Primary cosmic rays constitute an isotropic flux of atomic nuclei and of elementary particles that arrive at the Earth's atmosphere at a rate of around 1000 per squared meter per second. When these particles penetrate the atmosphere and collide with nuclei present in the air, they produce secondary particles that are detectable at the sea level.

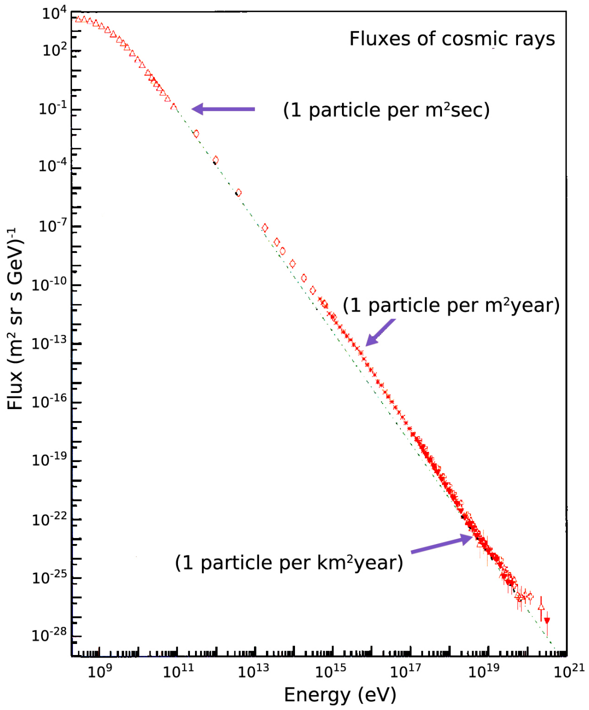

Figure 1.2: Cosmic ray energy spectrum.

The energy spectrum of the observed particles, which is shown in figure 1.2, extends over a large energy range, and varies over more than 32 orders of magnitude. It is characterised by a power law of spectral index γ:

$$I(E) = \frac{dN(E)}{dE} \propto E^{-\gamma} \text{ where } \gamma \simeq \begin{cases} 2.7 \text{ for } E < E_1 \\ 3.0 \text{ for } E_1 < E < E_2 \\ 2.7 \text{ for } E > E_2 \end{cases} \tag{1.1}$$

Experimental observations show two changes on the spectral index. The first change happens around 10^{15}eV (E_1) and it is called the "knee", and the second one happens at around 10^{19}eV (E_2) and is called the "ankle".

Determining the origin of the cosmic rays is not an easy task, because their arrival directions measured in the Earth, do not point back to their sources of production: since they have a net electric charge, cosmic rays are deflected by the interstellar and intergalactic magnetic fields. Even at the highest energies, the expected deviation between the direction of the source and the arrival direction of the particles can be of several degrees. These deviations depend on the electric charge of the cosmic rays or in other words, on their chemical composition, which tends to be dominated by heavy elements (Fe nuclei) at the highest energies [2], [51].

Yet another interesting feature about cosmic rays, is that of their abundance at the highest energies. Confirmed by experimental observations, the cosmic ray spectrum is suppressed for energies higher than $5 \cdot 10^{19}$ eV. This suppression is a combination of the GZK effect (which stands for Greisen-Zatsepin-Kuz'min) [52] and [100], which is originated by the interactions of cosmic rays of highest energies with the diffuse microwave background radiation remaining from the formation of the Universe, and of the physics of the astrophysical sources. As explained for instance in reference [29], protons propagating through the intergalactic medium lose their energy by interacting with the cosmic microwave background via two possible processes,

$$p + \gamma_{\mathsf{CMB}} \rightarrow \Delta^{+} \tag{1.2}$$

$$p + \gamma_{\mathsf{CMB}} \rightarrow p + e^{+} + e^{-}. \tag{1.3}$$

At energies of $\sim 10^{19}$ eV, the main free path for pair production is around 10 times longer than for the production of a Δ resonance for which the mean free path is ~ 50 Mpc, which is a short distance compared with the dimensions of the observable Universe. The latter process is therefore considered as a main responsible of the GZK effect.

1.2.2 Cosmic rays, gamma rays and neutrinos

The current knowledge about astrophysical objects relies on observations made through photons (electromagnetic radiation), which have been, for centuries, the most essential messengers in astrophysics. The relation between the electromagnetic emission from the different astrophysical sources and their intrinsic physical properties is so rich, that dedicated branches of astrophysics are required to study the different regions of the electromagnetic spectrum, from the lowest energies corresponding to radio frequencies, up to the highest energies in the gamma domain. The emission of radiation in the highest energies of the electromagnetic spectrum is particularly interesting in the context of both neutrino astronomy and cosmic ray physics, since it is believed that there exists a direct relation between the acceleration of cosmic rays and the production of high energy neutrinos and gamma radiation.

Cosmic ray acceleration

The main CR acceleration mechanism involves the collision of different plasmas, in which a shock front is produced. The presence of magnetic inhomogeneities in the media where these shock fronts propagate leads to the acceleration of charged particles as it is explained for instance in [87]. In these CR acceleration model, a charged particle crosses the shock front back and forth several times, each time interacting with an inhomogeneity in the magnetic field and gaining some energy. In its most simple version, this mechanism predicts that the resulting spectrum for a population of particles that get accelerated in a shock front is a power law $\sim E^{-\gamma}$ with $\gamma = 2$, consistent with the CR observations. In reference [55], M. Hillas set an upper limit on the maximum energy up to which a particle of electric charge $q = Z \cdot e$ can be accelerated, which depends on the size R of the source, and on its typical magnetic field B. This condition is obtained by requiring the Larmor radius of the particles, $r_L = E/qBc$ to be smaller than the dimension of the acceleration site. The maximum energy up to which a source can accelerate a particle is given by the relation

$$E_{\mathsf{max}} = Z \cdot e \cdot B \cdot R \tag{1.4}$$

Figure 1.3 has been extracted from reference [33] and shows the so called Hillas diagram, where the diagonal lines represent the condition 1.4 for different particle types and different energies in the plane $\log(R/1\mathrm{Km}) - \log(B/1\mathrm{G})$. As well, several source types are represented in the diagram, according to their observed properties. This diagram allows to identify potential CR accelerators. Sources falling above a certain diagonal line, can accelerate the corresponding particle up to the corresponding energy.

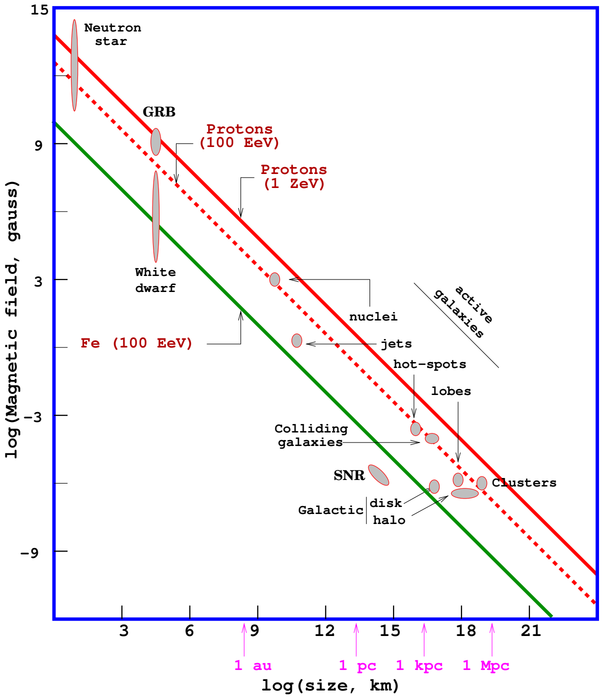

Figure 1.3: The Hillas diagram.

Emission of non thermal high energy gamma rays

The emission of high energy electromagnetic radiation from sources where charged particles are accelerated is contemplated in two different scenarios.

In the so-called leptonic scenario, high energy photons are produced in radiative processes associated to electrons or positrons, such as inverse Compton scattering

$$e^- + \gamma^{\text{low E}} \rightarrow e^- + \gamma^{\text{high E}}, \tag{1.5}$$

where the scattered photons can be either low energy photons emitted in thermal processes, or synchrotron photons emitted by the accelerated electrons. In the latter case, the photon acceleration mechanism is known as Synchrotron Self Compton (SSC).

On the other hand, high energy photons can also be produced in what is called the hadronic scenario, when cosmic rays interact with matter present in the acceleration region, or with ambient radiation. In this scenario, a proton can interact with ambient radiation producing pions through the processes

$$p + \gamma \rightarrow \Delta^{+} \rightarrow \pi^{0} + p \tag{1.6}$$

$$p + \gamma \rightarrow \Delta^{+} \rightarrow \pi^{+} + n \tag{1.7}$$

where the produced neutrons can also interact with the ambient radiation producing pions in the analogue reactions

$$n + \gamma \rightarrow \Delta^{0} \rightarrow \pi^{0} + n \tag{1.8}$$

$$n + \gamma \rightarrow \Delta^{0} \rightarrow \pi^{-} + p \tag{1.9}$$

As just mentioned above, pions can also be produced in the nucleon nucleon interactions,

$$p + p \rightarrow p + p + \pi^{0} \tag{1.10}$$

$$\rightarrow p + n + \pi^{+} \tag{1.11}$$

$$p + n \rightarrow p + n + \pi^{0} \tag{1.12}$$

$$\rightarrow p + p + \pi^{-} \tag{1.13}$$

Pions are short-lived particles whose decays lead to the production of high energy photons and neutrinos as follows

$$\pi^{0} \rightarrow \gamma + \gamma \tag{1.14}$$

$$\pi^{+} \rightarrow \mu^{+} + \nu_{\mu} \rightarrow e^{+} + \nu_{e} + \nu_{\mu} + \bar{\nu}_{\mu} \tag{1.15}$$

$$\pi^{+} \rightarrow \mu^{-} + \bar{\nu}_{\mu} \rightarrow e^{-} + \bar{\nu}_{e} + \nu_{\mu} + \bar{\nu}_{\mu} \tag{1.16}$$

Up to now, electromagnetic observations have not provided with an unambiguous way for knowing whether the origin of the high energy gamma radiation is hadronic or leptonic. Nevertheless, the fact that neutrinos are produced in the hadronic scenario but not in the leptonic processes opens the possibility of using neutrino astronomy for obtain information about the origin electromagnetic emission from astrophysical sources.

1.2.3 The role of neutrinos as cosmic probes

The detection of high energy neutrinos coming from a source of high energy gamma rays would prove that at least a component of its non thermal electromagnetic emission has a hadronic origin. In addition, detecting high energy neutrinos would also allow to identify sources of high cosmic rays: the processes listed in the previous paragraph suggest that the mere existence of high energy neutrinos implies the existence of accelerated cosmic rays.

Compared to photons and accelerated charged particles, neutrinos are unique astrophysical messengers since they present two advantages: on the one hand, they don't have electric charge and therefore they travel along straight trajectories without being deflected by magnetic fields. Unlike charged particles, neutrinos point to their sources. On the other hand, they are weakly interacting particles and they can travel long distances without interacting with matter or radiation. This is not the case for photons, that although are electrically neutral they get absorbed by matter or radiation and can hardly escape from dense regions. Indeed, the photons that we detect at the Earth are emitted from the periphery of the sources and do not carry any information about their cores. Besides, those photons that are emitted from the sources can also get absorbed by the interstellar radiation or with the cosmic microwave background.

Provided that neutrinos can be detected with a large enough statistics, they are ideal candidates for doing high energy astronomy which give access to cosmological distances and to the denser regions of astrophysical sources.

1.3 Potential neutrino sources

From the considerations mentioned in the previous paragraphs, every astrophysical source able to accelerate charged particles up to high energies is also a potential source of high energy neutrinos. There exists a wide variety of such sources, some of which are present in our galaxy and some of which are extragalactic. In the following paragraphs, some of them are briefly described.

1.3.1 Galactic sources

Among the galactic neutrino sources one can find supernovae remnants **(SNR)**, resulting from explosions of stars in which the matter expelled towards the interstellar medium creates shock fronts. A particular type of supernova remnant is the so-called Pulsar Wind Nebulae **(PWN)**, which hosts a pulsar with a strong and rapidly rotating magnetic field able to produce winds of relativistic charged particles that stream into the interstellar medium producing shock fronts.

Binary systems where a compact object such a black hole or a neutron star accrete matter from a companion star are also considered potential sources of high energy neutrinos. The most interesting among them are the microquasars, which exhibit photon emission along two relativistic jets aligned where the necessary ingredients for accelerating charged particles are present: magnetic fields, and shock fronts produced by the ejection or matter.

1.3.2 Extragalactic sources

Neutrinos from extragalactic origin can be produced in several types of sources. **Starburst galaxies** are galaxies showing an abnormally high star formation rate. The collective effect of supernova explosions combined with winds from massive stars in their central regions, contribute to the ejection of matter towards the interstellar medium where protons and electrons are accelerated. In reference [65], the observation of synchrotron radiation from such galaxies in the radio band, is used to compute a lower limit on the cumulative neutrino flux produced in accelerated pp interactions, which is of the order of $\phi_\nu = 10^{-7}E_\nu^{-2}\text{GeV}^{-1}\text{cm}^{-1}\text{s}^{-1}\text{sr}^{-1}$.

Extragalactic neutrinos are also expected to be produced as a consequence of the interactions of protons with the cosmic microwave background. As a consequence of these interactions, Δ resonances can be produced according to equation 1.2, which later decay producing neutrinos (equations 1.6). In reference [29] it is shown that from the two possible interaction channels of protons with CMB photons, the production of Δ resonances dominates for energies $> 5 \cdot 10^{19}$eV, resulting in a neutrino flux that ranges from $E_\nu \sim 10^{16}$ eV to $E_\nu \sim 10^{21}$ eV. This neurino flux is often referred to as **GZK neutrinos** or **cosmogenic neutrinos**.

Gamma Ray Bursts (GRBs) are also potential neutrino sources. GRBs are violent photon eruptions detected by satellites at a rate of about one per day. Their spatial distribution appears to be isotropic, suggesting their extragalactic origin. The most accepted model for explaining the observations of such events is the so-called fireball model which assumes that a large amount of matter is ejected from the core of an astrophysical source. The matter is ejected in shells that slow down as they propagate away from the core. When the outer shells are hit by the inner shells, shock fronts are created where charged particles can be accelerated up to high energies. Neutrino emission from these phenomena has been calculated for instance in references [96], [77] or [98].

This thesis is related to the detection of neutrinos from **Active Galactic Nuclei (AGN)**, which is another potential source of high energy neutrinos. They can be considered the large scale version of microquasars, and consist on a black hole in the center of a galaxy, which accretes matter from its innermost region, emitting jets. The next chapter is dedicated to a more detailed description of these objects.

Chapter 2

Active Galactic Nuclei

2.1 Introduction

Galaxies can be classified into two main classes: active galaxies and inactive galaxies. This classification is possible thanks to the analysis of their electromagnetic radiation over different frequencies. The electromagnetic radiation of galaxies (and of any astrophysical object in general) is described by their Spectral Energy Distribution (SED) or spectrum, which is a graphical representation of their monochromatic luminosity $L_\nu[\text{erg s}^{-1}]$. This is the energy emitted by a source per unit time and unit frequency. Some times, the monochromatic flux $F_\nu[\text{erg s}^{-1}\text{cm}^{-2}]$, which is the monochromatic luminosity per unit area, is also used. The SED has a fundamental role in the classification of galaxies, since its shape can reveal features that can be identified with particular physical processes taking place in the different galactic regions. In particular, it shows that active and inactive galaxies are quite different.

The radiation emitted by inactive galaxies is thermal radiation dominated by stars, with small contributions from interstellar gas and dust. Since the stellar radiation is emitted from the stars atmospheres which are in thermodynamical equilibrium, it can be described at a first approximation by a black body spectrum whose temperature depends on the stellar mass and evolutionary state [80]. Inactive galaxies spectra are observed as a superposition of stellar spectra spanning energies from the near infrared to the near ultraviolet. On the other hand, the spectrum of active galaxies suggest that their emission has a different origin. Basically, two differences can be observed between the spectrum of active galaxies and that of inactive galaxies. First, the active galaxies spectra span a much wider energy range that extends from the radio wavelengths up to the gamma ray wavelengths. Second, their total luminosity is larger than that of inactive galaxies. These two differences can be seen in figure 2.3, which shows the typical continuum spectra of an active galaxy and an inactive one.

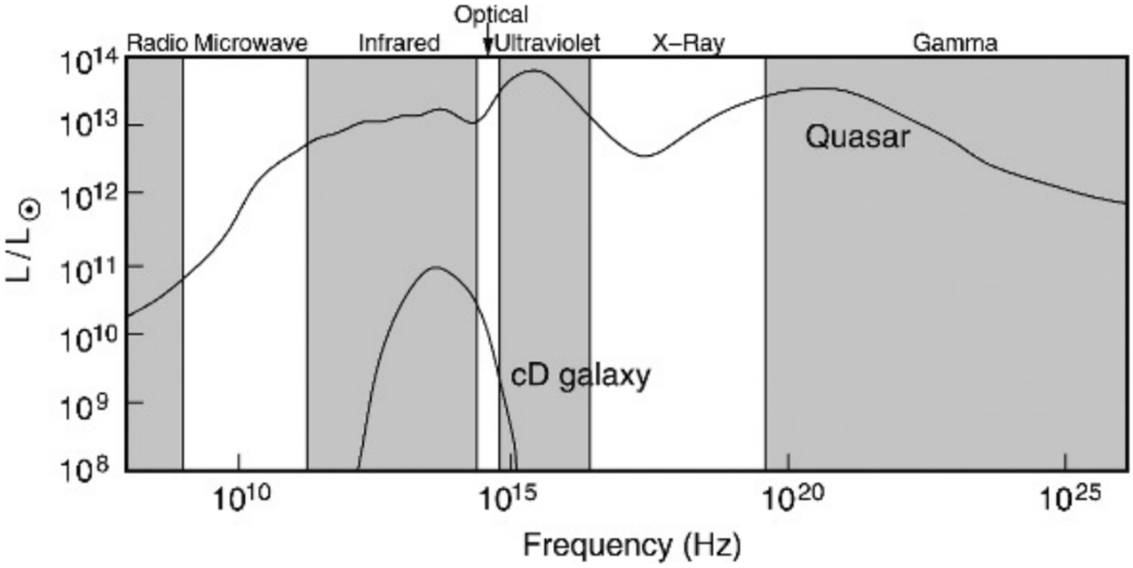

Figure 2.1: Comparison of the Spectral Energy Distribution (SED) of an active galaxy (labeled as Quasar) to that of an inactive galaxy (labeled as cD galaxy). Active galaxies emit radiation in a much wider energy range than inactive galaxies, and their luminosities are significantly higher.

The distinction between these two classes of galaxies came after the late 1940s when the astronomer Carl Seyfert observed a few particularly bright galaxies (compared to the standard ones) in which a significant fraction of the emitted radiation was not coming from stars as one would expect to happen in normal galaxies, but from a small central region. Observations of these galaxies at different wavelengths have been made since the latest decades of the XXth century, which confirm that their central regions host sources of energy production different from stars. These observations point to the possibility that the origin of such a particular energy spectrum, is on the gravitational activity related to the accretion process of matter onto a super massive black hole. The nuclei of these galaxies are therefore called Active Galactic Nuclei (AGN).

This chapter is dedicated to give a general description of AGN. In section 2.2, a review of the AGN observations along the electromagnetic spectrum is given, and the main components of these objects are described. In section 2.3, a summary of the different AGN classes is given.

2.2 AGN: Multi-wavelength observations

Since their discovery, AGN have been observed in a wide range of wavelengths in the electromagnetic spectrum. The morphology of these objects is so complex compared to that of stars, that observations of the same AGN at different wavelengths reveal their different morphological components. Figure 2.2 shows images of the *Centaurus A* galaxy recorded at infrared, optical, X-ray and radio wavelength bands, as well as a multi-wavelength composition. This example shows how AGN observations from different surveys provide complementary information about their morphology, and therefore allow to build models for the physical processes taking place in the different regions.

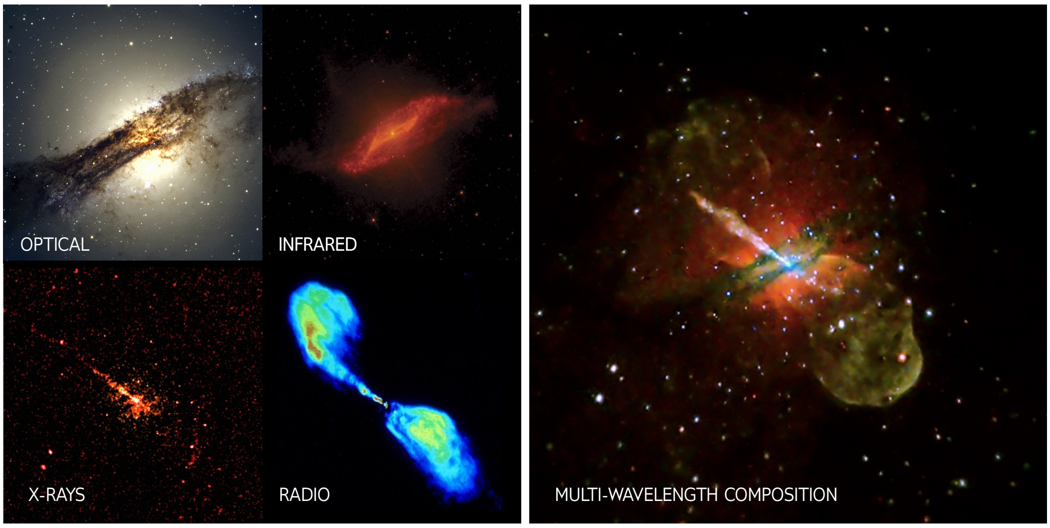

Figure 2.2: Observations of Centaurus A in different wavelengths.

Although not all the observed AGN present the same features as Centaurus A, figure 2.2 shows the most representative morphological characteristics of these objects and can help to understand their physics and classification. After decades of study and observations of AGN it turns out that not only the wavelength at which they are observed, but also the angle from which these objects are observed has an influence in their observed spectral properties. Indeed, each wavelength band has its own AGN classification system into different categories that depend on the observation angle. This has led to an AGN classification system into a large number of categories and sub categories that are not mutually exclusive, which may seem chaotic at first glance and which may lead the non-experts to confusion and disorientation.

After decades of observations and research in the field, the AGN unification paradigm emerged to simplify the understanding of these objects [94]. This paradigm holds that AGN falling into the different subclasses mentioned before, share essentially the same intrinsic physical properties, and that the differences that make them to be classified as objects of different classes come mainly from observational aspects such as their relative orientation with respect to the observer, or the choice of the wavelength at which they are observed. According to this paradigm, AGN transform gravitational potential energy into heat by the accretion of matter onto a rotating super massive black hole located at the center of the host galaxy. In this process, the particles in the gas are arranged into an accretion disk that lays in the plane perpendicular to the black hole's rotation axis, and which is in turn surrounded by an obscuring torus of gas and dust. Additionally, AGN are characterized for having a high gas velocity region and a lower gas velocity region called broad-line region (BLR) and narrow-line region (NLR) respectively, where gas clouds that are orbiting around the black hole, absorb and re-emit the radiation coming from the accretion disk producing the spectral lines that characterize the AGN spectra. These regions are located between the accretion disk and the dust torus, and the origin of their names is related to the relation between the width of the observed spectral lines and the velocity of the atoms responsible for their emission. In addition, some AGN present radio jets oriented perpendicular to the plane containing the accretion disk.

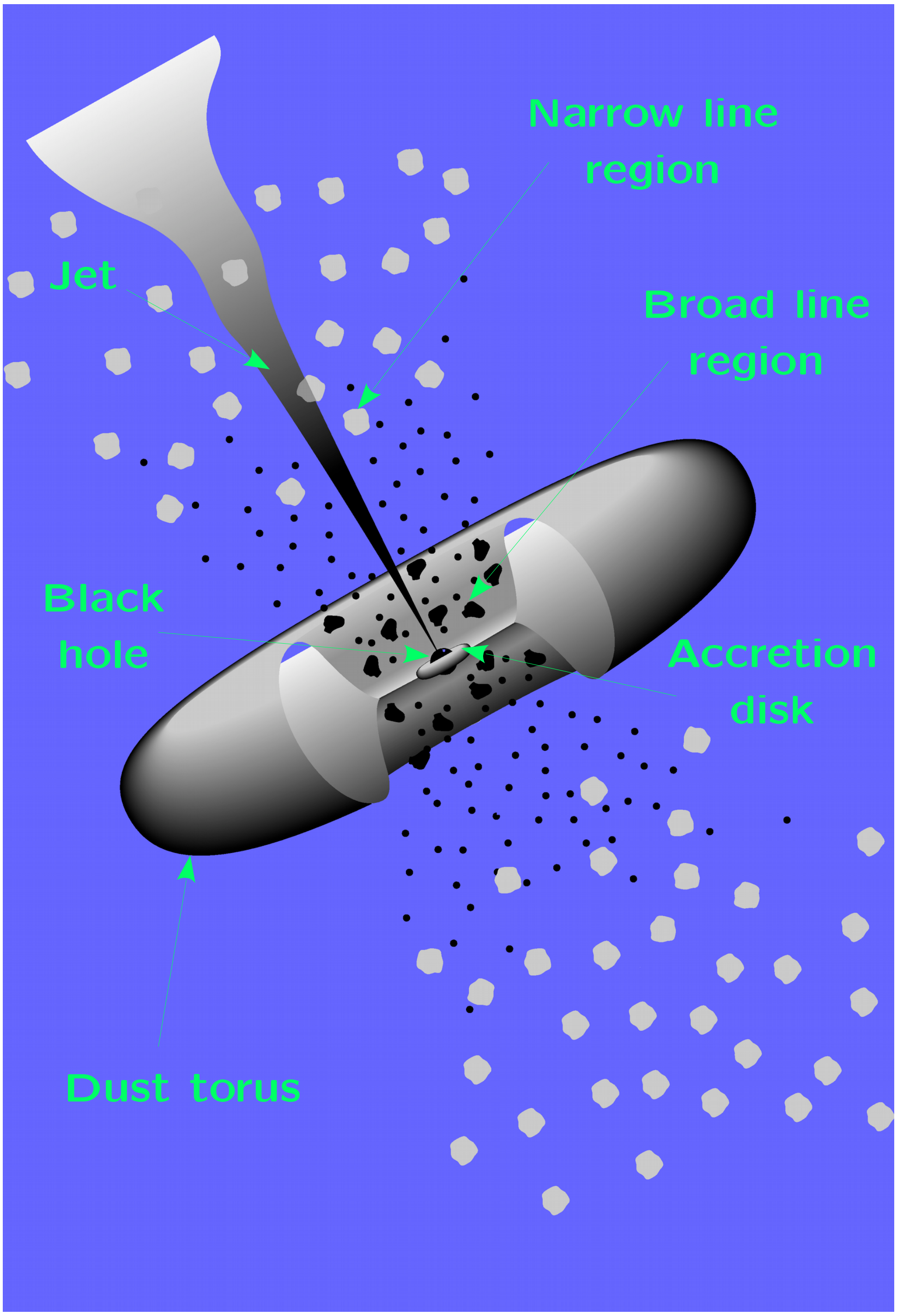

Figure 2.3: Schematic view of an AGN as described in the AGN unification paradigm. A black hole accretes matter from its neighbourhood arranged in an accretion disk, and surrounded by a dust torus. The broad line region appears obscured by the torus when the viewing angle is close to 90º with respect to the rotation axis, while the narrow line region is not.

In the rest of this section, an overview of the AGN observations in the different wavelength bands will be given.

2.2.1 Optical observations

The optical spectra of AGN show that they can be mainly classified into two categories called Type I and Type II AGN. Figure 2.4, show the spectra of a type I and a type II AGN between 4000Å and 7000Å where the spectral lines from the atomic recombination processes can be

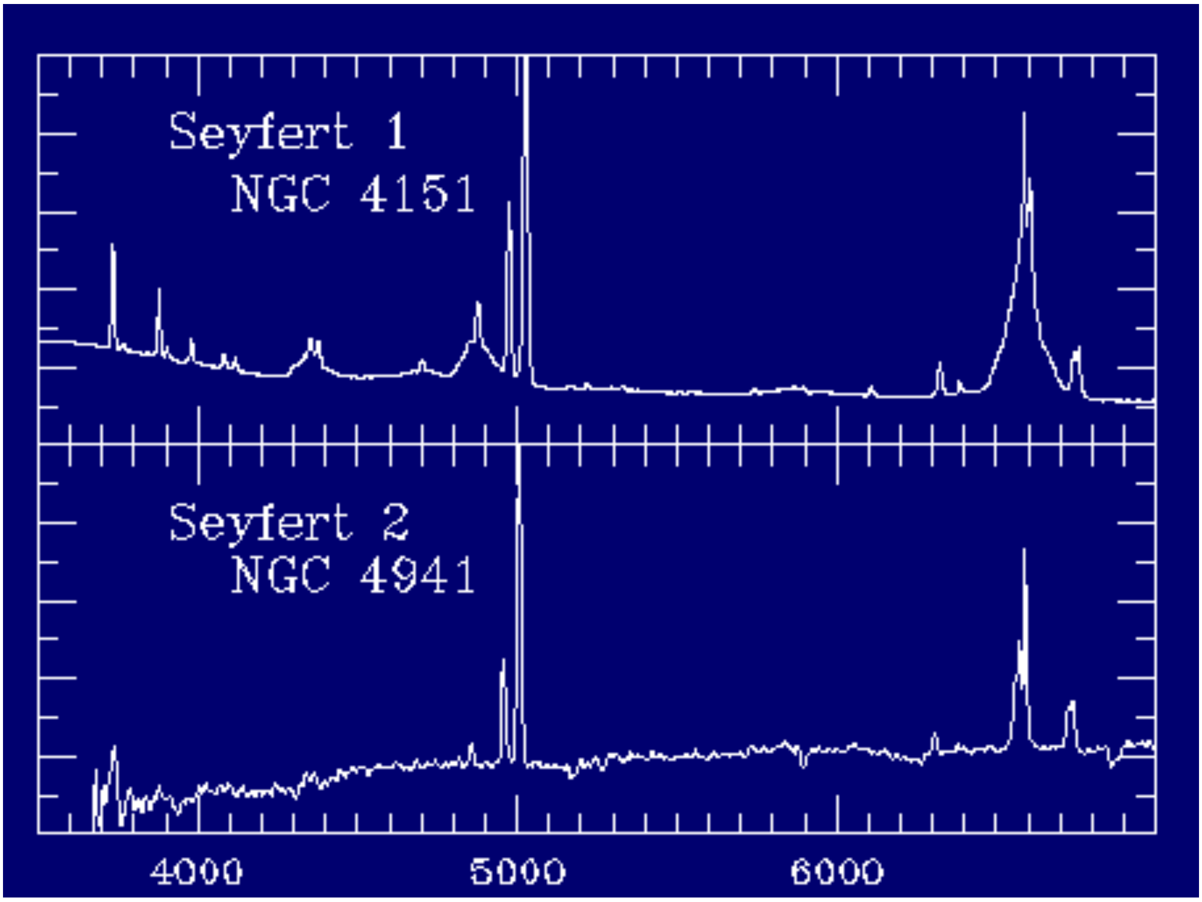

Figure 2.4: Spectra of a type I and a type II AGN. The units are in Å. Image taken from http://pages.astronomy.ua.edu/keel/agn/spectra.html

The broadening of the spectral lines can be interpreted as a Doppler shift in the wavelength of the radiation emitted by the atoms, caused by their motion with respect to the observer frame. Assuming that atoms of a certain type are emitting radiation corresponding to a spectral line of wavelength λ_0 in their rest frames, and that their velocities follow a distribution characterized by a width Δv, the observed width of the spectral line $\Delta\lambda$ is related to the previous quantities by

$$\frac{\Delta\lambda}{\lambda_0} = \frac{\Delta v}{c} \tag{2.1}$$

where c is the speed of light in vacuum. Δv is a quantity often used in astronomy to characterize the width of the observed lines, and is usually given in km/s. The broadest lines present in type I AGN reach widths that correspond to large-scale velocities of the order of ~ 10.000 km/s, while the broadest lines in type II AGN correspond to velocities up to ~ 800 km/s. Such a broadening in the spectrum cannot be explained by the thermal motion of the atoms, and supports the idea that the energy emitted by AGN is not of thermal origin [1]. In the AGN unification paradigm, type I and type II AGN are not very different objects and the observed differences between them are explained by their orientation relative to the observer. In the unification scenario, both type I and type II AGN have a region near the accretion disk where the gas is moving at high velocities (the BLR mentioned above), and a region further away from the accretion disk where the gas moves at lower velocities (NLR). The difference between both types of AGN is their orientation relative to the observer. Type II AGN, are oriented in such a way that the radiation emitted by the BLR towards the observer is absorbed by the dust torus whereas type I AGN are oriented in such a way that there is a direct line of sight between the observer and the BLR, and the radiation emitted by this region is not absorbed. Additionally, there is a third group of AGN called Type 0 AGN characterized by unusual spectral properties. In particular, they present very weak emission lines.

---

[1] If a velocity of ~ 10000 km/s is associated to the thermal motion of a gas, it follows from the kinetic theory that $k_B T \sim m_p(\Delta v)^2/2$, from where the corresponding temperature would reach values of $T \sim 10^{10}$K. But that is not possible, since all the atoms would be fully ionized at such high temperatures.

2.2.2 Radio observations

When observed in the radio regime, a dichotomy arises between those AGN that are strong radio-emitters, and those that are weak radio-emitters. The weak radio-emitters are called *Radio Quiet* (RQ) AGN, and the strong radio-emitters are normally called *Radio Loud* (RL) AGN. AGN are classified as RL or as RQ according to the value of their radio-loudness parameter R, which is defined as the ratio of radio $L_{\nu}(\nu = 5$ GHz) to optical $L_{\lambda}(\lambda = 4400$Å) monochromatic luminosities. Observations, show that only about the 10% of AGN are radio-loud. Radio loud AGN usually present a peculiar morphology consisting on a compact central region that coincides with the center of the galaxy, and an extended region that can exceed the dimensions of the parent galaxy by a large factor. The extended region consists on single or double radio lobes situated more or less symmetrically around the center and connected to it by radio jets which are believed to be related to the energy transport from the center to the lobes. These features are clearly visible in the radio image of Centaurus A, in figure 2.2.

In second place, radio loud AGN can be further classified according to their spectral energy distribution. Their flux in the radio band is well described by a power law, $F_{\nu} \propto \nu^{-\alpha_R}$ where the spectral index α_R has a different value for each source. According to its value, radio loud AGN are classified as *flat spectrum radio sources* if $\alpha_R < 0.5$, or *steep spectrum radio sources* in the opposite case. The value of the observed α_R appears to be related with the observed morphological structure in the radio regime. Steep-spectrum radio sources show lobes while flat-spectrum radio sources appear to be more luminous in their cores, and show weak or undetected lobes. As in the optical regime, the AGN unification paradigm associates these differences to a dependence on the relative orientation of the AGN to the observer. Steep-spectrum radio sources are viewed from large angles with respect to their rotation axes and the observed spectrum is dominated by the radio-lobes, while flat-spectrum radio sources are detected in directions that form small angles with the AGN rotation axes and the observed spectrum is dominated by their cores [93].It is believed that the radiation emitted in the radio wavelengths, is synchrotron radiation emitted by relativistic electrons moving through a magnetic field, and whose energies also follow a power-law distribution [70], [82].

2.2.3 X-ray observations

Since the latest 1970s it has become evident that AGN are X-ray emitters [44]. X-rays constitute an important component of the AGN electromagnetic emission reaching up to a 40 $\%$ of their bolometric luminosity. Being in the high energy region of the electromagnetic spectrum, X-rays are thought to be produced in the central most regions of AGN (see [82] [31] and references therein). Figure 2.5 shows the typical X-ray spectrum of a type I AGN, which is the result of several components associated to different physical processes [79]. The primary component is believed to be originated in the internal part of the accretion system, where optical and UV photons emitted from the accretion disk are inverse-Compton scattered by a surrounding corona of relativistic electrons [42]. The change in the photon spectrum after being inverse-Compton scattered by hot electrons is called Comptonization, and it can be shown [90] that the outgoing photon spectrum follows a power-law distribution. Observations seem to converge to a power-law spectrum that extends from the lowest energy X-rays up to a high energy cut around $\sim$100 keV. The material standing in the line of sight between the source of the primary X-ray photons and the observer, may leave an imprint in the X-ray spectrum after reprocessing a fraction of the primary component. This reprocessing can take place through different physical processes: an X-ray photon can be either Compton scattered by free or bound electrons, it can undergo a photoelectric absorption followed by either a fluorescent line emission or an Auger de-excitation. For low energy X-rays the total cross section is dominated by the photoelectric absorption, whereas the highest energy X-rays are most likely Compton scattered. The resulting spectrum after the primary component reprocessing shows a broad hump peaked at around $\sim$ 30 keV [78], which in figure 2.5 is marked as *reflection hump*. In addition a peak corresponding to the iron Kα spectral line can be observed at $\sim 6.4keV$. A large fraction of type I AGN also show an excess at low energies called *the soft X-ray excess* whose origin is not yet clear [34]. The Chandra X-ray observatory discovered that most of the AGN jets that are observed in radio surveys, have an X-ray counterpart as it is shown in fig 2.2.

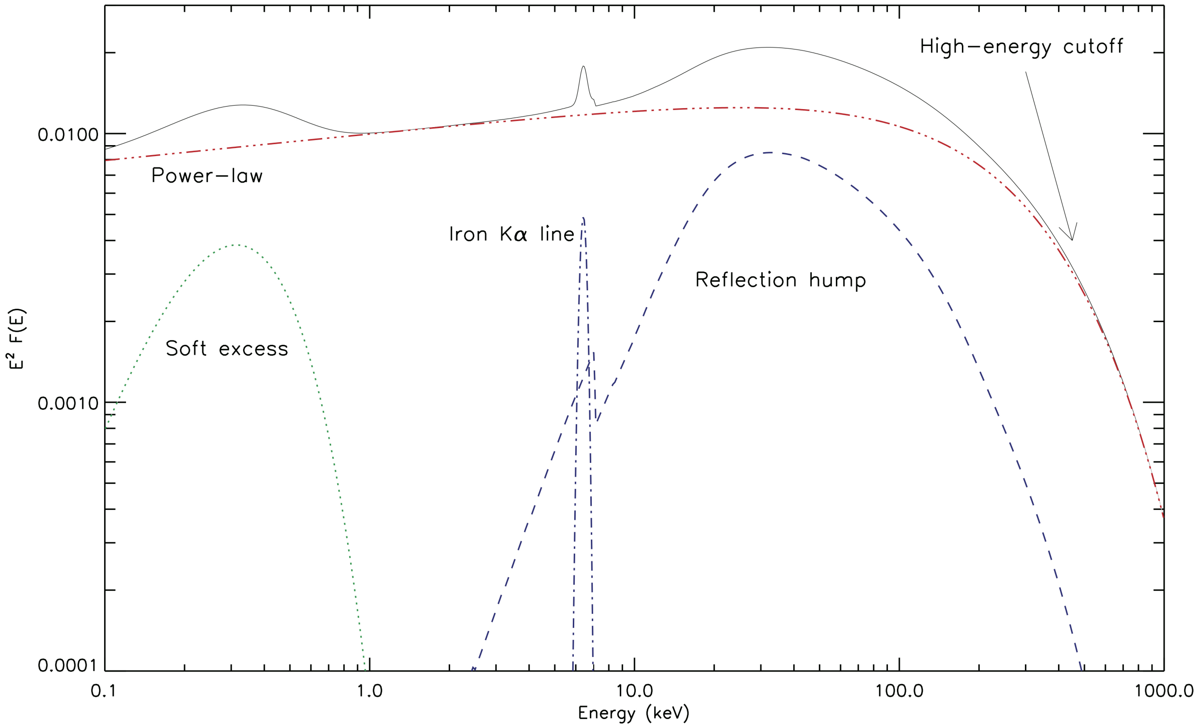

Figure 2.5: AGN X-ray spectrum

2.2.4 Infrared observations

It is believed that the radiation emitted by AGN in the infrared wavelength range is originated by thermal emission in the dust in the torus after being heated by the radiation emitted during the accretion process. Figure 2.6 taken from [99] shows how black body spectra at different temperatures can be used to describe the IR spectrum of the galaxy PG1351+640. In the AGN unification scenario, the IR thermal emission is well described by a clumpy torus model with dimensions of the order of (~ 10pc) in which the temperature of the dust varies from ~ 10 K to $\sim 10^3$K [101] [36]. The thermal IR emission allows for the discovery of highly obscured AGN that would be miss-classified based on their optical or X-ray spectra [70], [56].

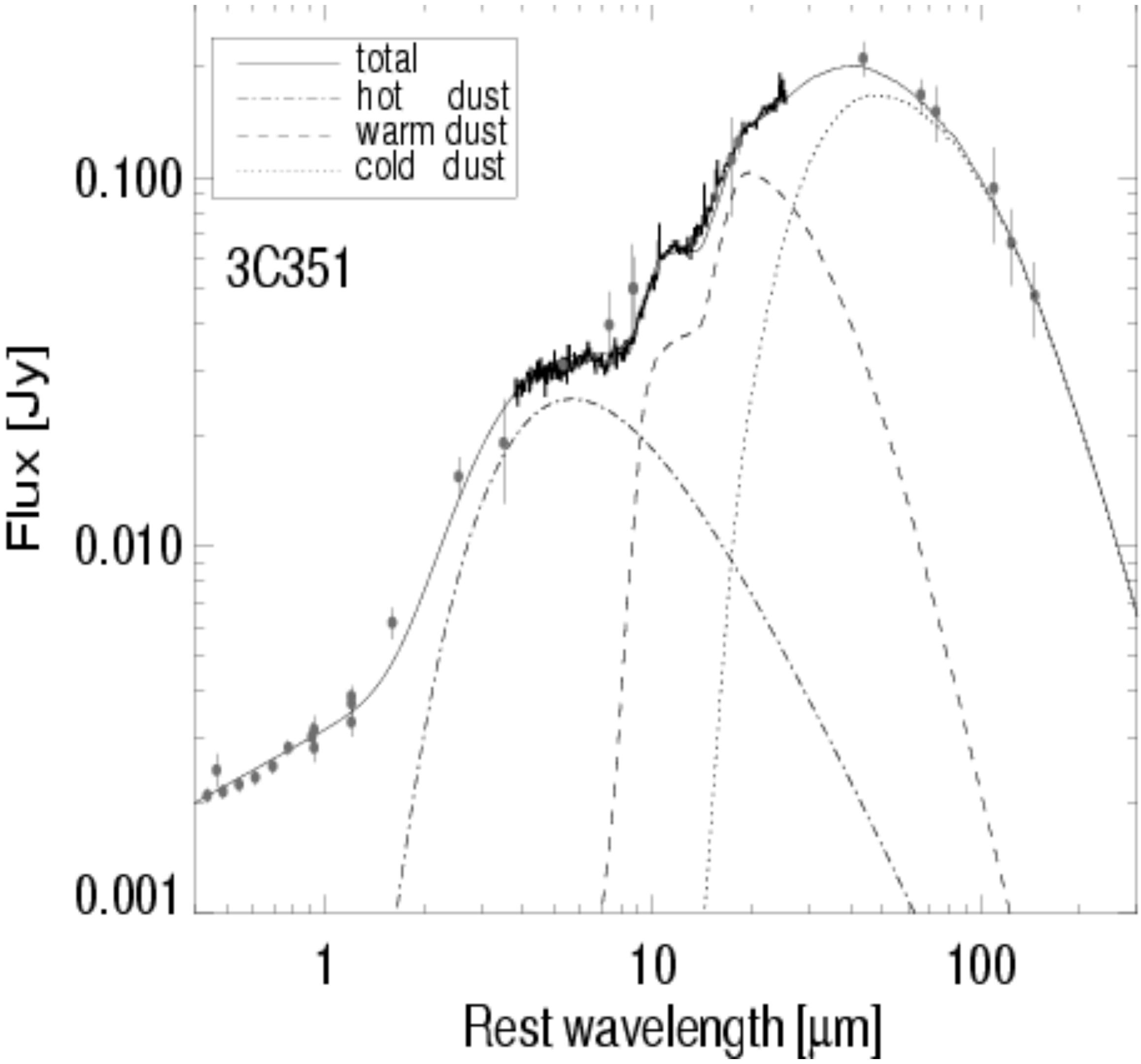

Figure 2.6: Infra-red spectrum of AGN, fitted to blackbody spectra.

2.2.5 Gamma-ray observations

The operation of the Compton Gamma Ray Observatory (CGRO) by NASA during the decade of the 1990s, supposed a revolution in gamma ray astrophysics. Following the Hubble space telescope, CGRO was the second of the so-called NASA's great observatories and was dedicated to the observation of the Universe at high energies. While the Hubble telescope is mainly sensitive to optical and ultra-violet wavelengths, CGRO was sensitive to an unprecedented broad range of high-energy electromagnetic radiation, covering from $\sim$20 keV to $\sim$30 GeV. The coverage of such a broad energy range was achieved by four independent instruments, each of which covered its own energy range with a sensitivity of better than a factor 10 with respect to previous experiments. The Burst and Transient Source Experiment (BATSE), covered the 15 keV - 1MeV energy range and was dedicated to the detection and location of transient gamma ray sources such as Gamma Ray Bursts (GRB). The Oriented Scintillation Spectrometer Experiment (OSSE) was oriented to the study nuclear lines in solar flares, radioactive decay of nuclei in supernova remnants, and matter-antimatter annihilation taking place near the center of our galaxy. OSSE was sensitive to gamma rays with energies ranging from $\sim$50 keV to $\sim$10 Mev. Finally, the Compton Telescope (COMPTEL) and the Energetic Gamma Ray Experiment Telescope (EGRET), covered energies ranging from 1MeV to 30 MeV, and from 20 MeV to 30 GeV respectively. The identification of almost 100 AGN in the gamma ray spectrum was one among the different scientific results achieved by the CGRO. Until Compton was launched, only one AGN had been observed in the gamma ray domain. Nowadays, the most relevant AGN observations in gamma rays, are made by the Fermi Large Area Telescope (Fermi-LAT), whose sensitivity ranges from 20 MeV to 300 GeV, and whose latest catalogue includes more than 1500 AGN [7].

The currently available technology doesn't allow to resolve most of the sources in gamma rays since their angular sizes are smaller than the detectors resolution, and therefore the current gamma ray detectors don't provide any new information on the morphology of AGN. Nevertheless, the gamma ray observations not only of AGN but also of other astrophysical objects such as GRBs are of great physical interest since the gamma rays emitted by AGN may be linked to the cosmic ray acceleration and emission. As it is explained in chapter 1, neutrinos may play a fundamental role in understanding the origin of gamma ray emission.

2.3 AGN classification

As it has been already said, AGN have been classified into various families according to their observed properties in different wavelengths. Some of these families were mentioned in section 2.2, and others were not mentioned. In this section, a simple classification of AGN based on the AGN unification framework will be described, naming only those classes that are relevant for the following chapters.

A common general classification of AGN can be made into radio loud and radio quiet AGN, as explained in sec 2.2.2. Since the high energy radiation is thought to be emitted from the radio jets [94] radio loud AGN are the most interesting candidates from the point of view of neutrino astronomy. According to the orientation of their jets with respect to the observer, radio-loud AGN are classified into 2 sub categories: On the one hand, Radio Galaxies (RG) are those RL AGN with the jet oriented close to 90º with respect to the observer. On the other hand, Blazars are those AGN with the jet oriented in the direction of the observer. Additionally, two types of blazars are the Flat Spectrum Radio Quasars (FSRQ) and BL Lac objects. The main differences between these last two families are in their energy spectrum. While FSRQ show strong broad emission lines, BL Lac objects present very weak emission lines.

2.4 Neutrinos from AGN

In a hadronic acceleration scenario one can assume the electromagnetic emission from AGN to be correlated to the emission of high energy neutrinos. In the past, several models of neutrino emission from AGN have been proposed. For instance, in reference [88] a model of neutrino emission from AGN cores is proposed, and in reference [89] an estimated flux and neutrino spectrum expected from that model is given. Models for neutrino emission from AGN jets have also been proposed in several references. For instance, in reference [60], a neutrino emission model is proposed in which protons which are accelerated at the base of the

AGN jets, interact with X-ray photons that have been Compton scattered near the base of the jet. In reference [30], another neutrino emission model from AGN jets is proposed, in which shock fronts propagating along the jets accelerate protons which interact with synchrotron photons emitted by relativistic electrons present in the jet.

In this thesis, no particular neutrino emission model from AGN is used. Instead, a simple relation of proportionality between the neutrino and electromagnetic emission from AGN is assumed, and based on this model, the neutrino emission from AGN populations is studied. To do so, it is necessary to use the information provided by AGN observations in the electromagnetic spectrum. Following the work presented in reference [59], and under the assumption that the neutrino emission and the electromagnetic emission are related by a proportionality law, observations in the X-ray band are used to infer how AGN of different classes are distributed according to their redshift and neutrino luminosities. These results will be used in chapters 8 and 9 to search for neutrinos from AGN populations with the ANTARES neutrino telescope which is introduced in detail in chapter 4. Before doing so, neutrino telescopes, and some of the latest results in neutrino astronomy (in particular the detection of cosmic neutrinos by the IceCube observatory), are introduced in the following chapter.

Chapter 3

Neutrino Telescopes

3.1 Detection principle

Reconstructing the arrival directions and energies of cosmic neutrinos is not an easy task, which is achieved by overcoming several challenges associated to the physical properties of neutrinos. The detection of high energy neutrinos is indirect and is done through the use of three dimensional matrices of photomultiplier tubes generally called **Optical Modules (OM)** that embedded in a transparent medium, detect the Cherenkov light induced by relativistic charged particles produced in the interactions of neutrinos with the nuclei of the environmental matter. In addition to be transparent, the medium where the OMs are embedded should also be dark in order to reduce the detection of optical background, and, since the flux of high energy neutrinos is low and their interaction cross section is weak, the instrumented volume is required to be large. The typical size of high energy neutrino telescopes is around 1 km^3, and they can be placed deep under ice or sea water.

The interactions of high energy neutrinos with matter produce different distributions of particles that depend on the interaction channel, and which are presented in detail in chapter 5. The most interesting interaction channel for high energy neutrino telescopes is the ν_μ charged current interaction, in which a muon is produced. Unlike the rest of the particles that are produced in neutrino interactions, muons travel long distances through the detector producing a distribution of light in the OMs that allows to reconstruct their trajectories with an angular resolution better than 1°. In addition, the angle between the muon and the neutrino directions at high energies is very small, making of ν_μ the best suited candidates for doing neutrino astronomy. Nevertheless, the products of cosmic neutrino interactions are not the only particles detectable by neutrino telescopes. As it is explained in section 3.1.2, the interactions of cosmic rays in the atmosphere produce the so-called atmospheric background which is constituted by neutrinos and muons. The main challenge for neutrino telescopes is to discriminate between cosmic and atmospheric events.

3.1.1 Cherenkov effect

As mentioned above, the charged particles produced in the neutrino interactions are detected thanks to the emission of the Cherenkov light that they induce. This light, which is observable in a transparent medium, is induced by every charged particle that propagates at a speed higher than the speed of light in the medium. This effect shows up as a luminous spark whose properties are related to the speed of the propagating particles, and the propagation medium. In particular, the light is emitted in a direction θ_{Ch} with respect to the direction of propagation of the particle, given by

$$\cos\theta_{\mathsf{Ch}} = \frac{1}{\beta\cdot n} \tag{3.1}$$

where $\beta = v/c$ represents the Lorentz factor of the particle, and n is the refractive index of the medium. At high energies, the particles produced in the neutrino interactions are highly relativistic and therefore $\beta \sim 1$. The Cherenkov angle in water, where $n =$ 1.364, has a value of θ ≈43°. The number of Cherenkov photons emitted by a particle can be computed from

$$\frac{\mathsf{dN}_\gamma}{\mathsf{d}x\mathsf{d}\lambda} = \frac{2\pi\alpha}{\lambda^2}\left(1-\frac{1}{\beta^2 n^2}\right) \tag{3.2}$$

where $\alpha = 1/137$ is the fine structure constant, and λ is the wavelength of the emitted photons. In the wavelength range where ANTARES OMs are sensitive (from 300 to 600 nm), $\sim 10^4$ photons per meter are emitted.

3.1.2 Atmospheric background

Apart from cosmic neutrinos, the physical events which are likely to produce high energy muons in the detector, and therefore of constituting a background source, are the interactions of cosmic rays in the atmosphere, which produce cascades of secondary particles. Among the particles present in the air showers produced by the cosmic ray interactions, the ones with more probability of propagating several kilometres underwater are muons and neutrinos (hereafter called atmospheric muons and atmospheric neutrinos, in order to distinguish them from the cosmic neutrinos, and from the muons produced by neutrino interactions near the detector). Both of them constitute a background source that can mask the signal produced in the detector by astrophysical neutrinos. Since the Earth is opaque to muons and transparent to neutrinos, the atmospheric muon background can be significantly reduced by allowing only upward going events, therefore opening an instantaneous observation window of half of the sky. Due to the rotation of the Earth, the integrated observation window varies as a function of the geographical coordinates as it is shown in figure 3.1, which represents in galactic coordinates, the fraction of the visible sky (for upward-going neutrinos) integrated on time for a telescope placed in the Mediterranean sea and a telescope placed in the south pole. While a telescope situated in the South Pole is permanently sensitive to the northern hemisphere sky and only covers a fraction of the galactic plane, the full visible zone for a telescope placed in the Mediterranean sea (like ANTARES), subtends a solid angle of $\sim$3.5π sr. This complementarity is a strong argument to build a neutrino telescope in each hemisphere[1].

---

[1] Note that large neutrino telescopes can also monitor the sky above, but at the expense of reducing the effective volume and the energy range of interest.

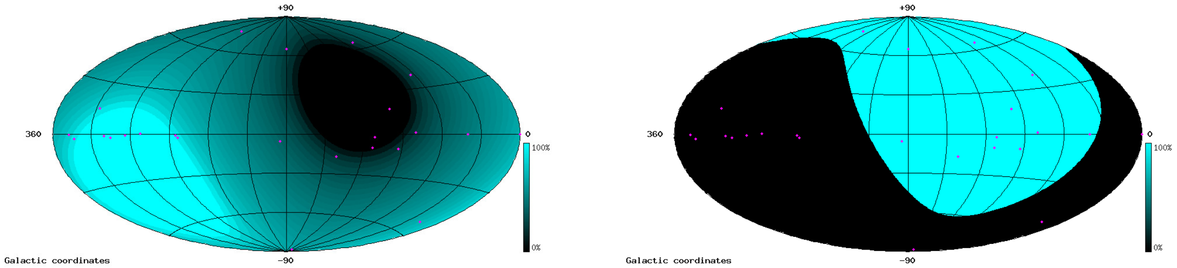

Figure 3.1: **Left:** Visibility of a neutrino telescope in the Mediterranean sea. **Right:** Visibility of a neutrino telescope in the South Pole. Both for upward-going neutrinos

Atmospheric muons are $\sim 10^6$ times more abundant at the detector level than the muons induced by atmospheric neutrinos as it is shown in figure 3.2. Nevertheless, atmospheric neutrinos constitute an irreducible source of background since they mimic perfectly the signatures produced by cosmic neutrinos, and it is impossible to distinguish between them on an event by event basis. There are three main approaches by which cosmic neutrinos can be discriminated from the atmospheric background. This discrimination can be achieved statistically, by analysing the spectral distribution of a measured sample. Since the atmospheric neutrino spectrum ($\propto E^{-3.7}$) is softer than the spectrum expected from cosmic neutrinos (typically E^{-2}), a diffuse cosmic neutrino emission is likely to produce an excess of events at high energies (see figure 1.1). Additionally, since the angular distribution of atmospheric neutrinos is uniform in space and time, another way of identifying cosmic neutrinos is by looking for space or time clustering. Finally, a third procedure to identify cosmic neutrinos is to search for coincidences in space or time with other cosmic messengers.

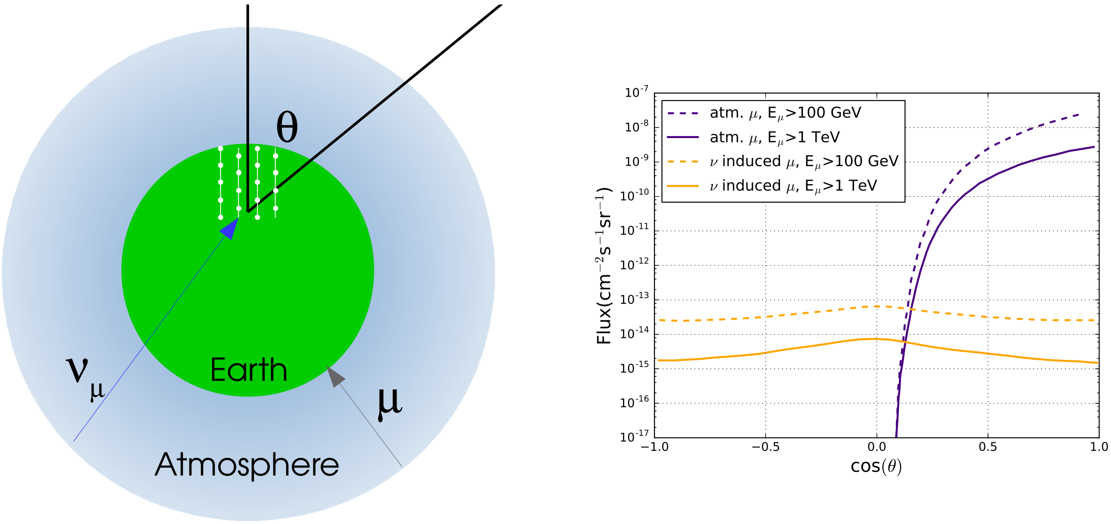

Figure 3.2: **Left:**Schematic representation of the effect of the Earth on the different components of the atmospheric background. **Right:** Atmospheric muon flux, and flux of muons induced by atmospheric neutrinos as a function of their arrival direction with respect to a neutrino telescope.

3.2 Neutrino telescopes in the world

There are currently 3 operative neutrino telescopes in the world. ANTARES in the Mediterranean sea, for which a detailed description is given in chapter 4, Baikal and IceCube.

Baikal is taking data from the bed of the lake with the same name since 1998, with around 200 optical modules distributed in 8 lines [21]. Recently, 3 prototype lines for a kilometre detector called Grand Volume Detector (GVD) have been deployed.

The largest detector is IceCube, which is constituted by 86 lines distributed over 1 Km^3 of ice in the South Pole, at a depth between 1500 and 2500 m. IceCube has as well an internal denser network of 6 lines called Deep Core, which allows to lower the energy threshold down to $\sim$10 GeV. Additionally IceCube is completed by a network of ~ 1Km^2 area called IceTop which is dedicated to the study of the cosmic ray composition. By looking for coincidences with the under-ice matrix of photomultipliers, IceTop also allows to reject downward going background events.

A complete discussion of the advantages of the different instruments is out of the scope of this work. Nevertheless, the most remarkable differences are described in the following lines.

Being in the Mediterranean sea, ANTARES is capable of achieving a very good angular resolution of $< 0.5\,\mathrm{deg}$ thanks to the optical properties of the sea water in its location (a typical absorption length of $\sim$ 50 m and an effective scattering length of $\sim$ 300 m). On the other hand, the sea water presents a drawback: it contains ^{40}K which undergoes β processes in which electrons are produced above their Cherenkov threshold, and bioluminescent organisms, which constitute a non negligible source of optical background. However, the optical background can be used for calibration purposes as it is explained in chapter 4. In addition, the sea currents produce displacements of the lines which is necessary to control continuously in order to reconstruct the events correctly. The polar ice where IceCube is embedded is characterized by a better absorption length but a worse scattering length, in the sense that its scattering length is shorter ($\sim$ 25 m), which has a negative impact on its angular resolution (which is typically of the order of some degrees). On the other hand, in the polar ice there are no sources of optical background, and the lines are always in the same positions.

3.2.1 The IceCube discovery

The first steps towards what today is considered as a breakthrough in neutrino astronomy were given by the IceCube collaboration in the year 2013 with the detection of the first very high energy (E >PeV) neutrinos. The observation of these events is reported on reference [4]. After applying a selection of events in the sample recorded between May 2010 and May 2012, which was based on applying a cut on the minimum deposited energy in the detector, two events remained in the data set, whose atmospheric origin was rejected with a 2.8 σ confidence level. Figure 3.3 shows the distribution of light produced by these events in the IceCube optical modules. The size of the spheres represents the amount of photoelectrons recorded by each OM and the colour scale indicates the photon arrival times, the red colour corresponding to the earliest times and the blue colour corresponding to the latest arrival times. The reconstructed deposited energy for these events was 1.04 and 1.14 PeV respectively.

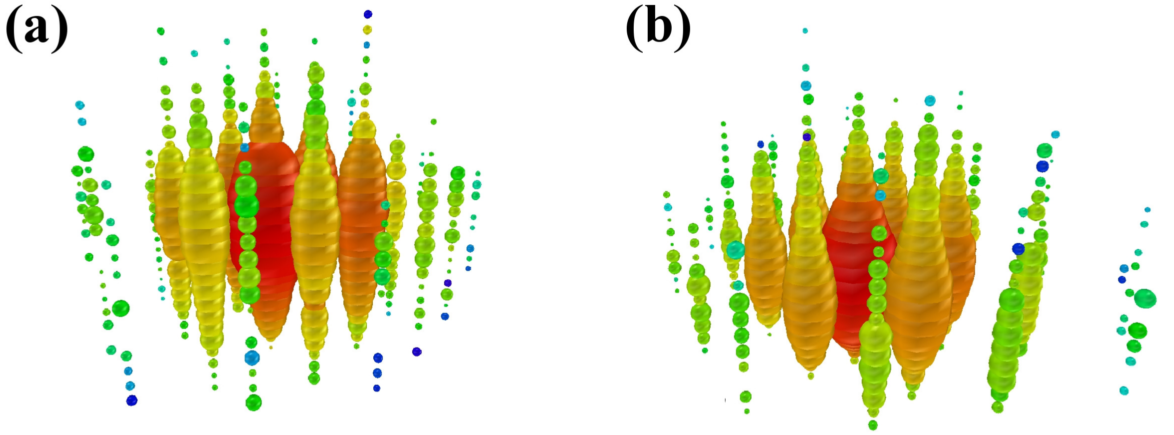

Figure 3.3: The distribution of light in the IceCube detector, produced by the first two high energy neutrinos ever detected. The size of the spheres represents the amount of photoelectrons recorded in the OMs, and the colors represent the photon arrival times. Red indicates the earliest times and blue the latest.

A follow up analysis of the same data set where different selection criteria were used, allowed to lower the energy threshold of the selected events improving the sensitivity to a cosmic neutrino flux. The general idea of this selection criteria, consists on selecting those events above a certain energy threshold (lower than the energy threshold in reference [4]), for which the neutrino interaction happens inside the instrumented volume, and which don't show a muon track coming from outside the detector. Since at high energies the directions of an atmospheric muon and an atmospheric neutrino produced in the same cosmic ray interaction are correlated as it is explained in reference [83], applying a veto to entering muon tracks helps to suppress the atmospheric background. This is achieved by using the external part of the detector to detect and veto entering muon tracks. Although this technique strongly reduces the effective detection volume, it rejects the 99.999% of downward atmospheric muons and a 70% of downward-going atmospheric neutrinos. The results after applying these selection criteria to the May 2010 - May 2012 dataset are published in reference [3], and constitute the first evidence for high energy cosmic neutrinos. A total of 28 events with energies between 30 and 1200 TeV passed the selection criteria, while around 11 background events were expected. The hypothesis that the 28 events have an atmospheric origin was excluded with a 4.1 σ confidence level.

The same selection criteria were applied to an extension of the previously mentioned dataset, which also included the data recorded by IceCube during 2012-2013. The results, which are published in reference [6] show that 37 events passed the selection while around 13 events were expected from background. The confidence level with which the atmospheric origin of these events was rejected, increased up to a 5.7σ confidence level. Figure 3.4 shows a distribution of the 37 events in equatorial coordinates together with a colour scale that indicates the result of a statistical search for clustering of events around point-like sources in different locations of the sky, which didn't produce a statistically significant result.

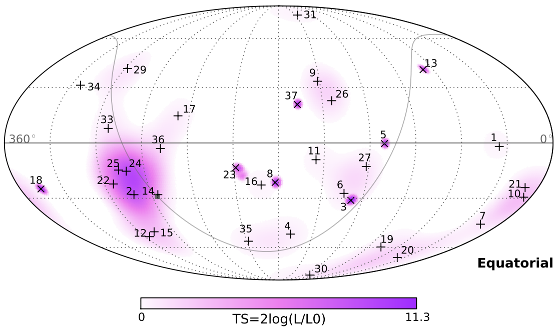

Figure 3.4: Distribution in equatorial coordinates of the 37 High Energy Starting Events detected by IceCube after three years of data taking.

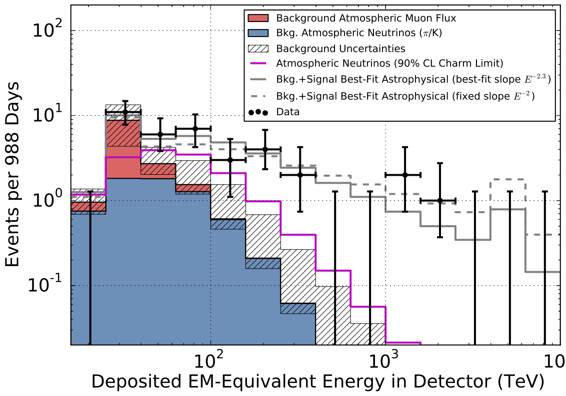

Figure 3.5: Distribution of deposited energies of the IceCube High Energy Starting Events, compared to model predictions. The gray lines correspond to two different astrophysical neutrino models where neutrinos follow a power law distribution.

The excess produced by these events is quantified in terms of a diffuse neutrino flux, which is obtained by fitting the observations at the highest energies to a combination of the neutrino flux resulting from the contribution of atmospheric neutrinos (conventional and prompt components) and a neutrino flux from astrophysical origin. The results are shown in figure 3.5. The gray dashed line corresponds to a fit where the astrophysical neutrino flux is assumed to follow an unbroken power law $\phi_\nu \propto E^{-\gamma}$ with a spectral index γ equal to 2, and the gray solid line corresponds to the best fit corresponding to an astrophysical neutrino flux which is also modelled as an unbroken power-law, but where the spectral index is allowed to vary. The best fit for the fixed index yield the result

$$E^2\phi(E) = 0.95 \pm 0.3 \times 10^{-8}\,\mathrm{GeV\,cm^{-2}\,s^{-1}\,sr^{-1}} \tag{3.3}$$

and the best fit for a variable spectral index with an cut off at 100 TeV was,

$$E^2\phi(E) = 1.5 \times 10^{-8}(E/100\,\mathrm{TeV})^{-0.3}\,\mathrm{GeV\,cm^{-2}\,s^{-1}\,sr^{-1}}. \tag{3.4}$$

These values are consistent with the diffuse flux limit derived long time ago by Waxman and Bahcall in reference [97]. In the following, the most important results achieved by ANTARES are summarised, which include some constrains to the origin of the IceCube HESE events.

3.3 ANTARES results

3.3.1 Performance

The performance of a neutrino telescope can be quantified by its angular resolution, its effective area and by its energy resolution, for track-like events (produced by ν_μ CC interactions) and for shower-like events (produced by ν_e and ν_τ CC interactions and all neutrino flavours

NC interactions). Further details about these types of events are given in chapter 5.

Performance for tracks

The median angular resolution, in other words, the median angle between the direction of a reconstructed track and the direction of the incident neutrino is presented as a function of the neutrino energy in figure 3.6 where the plots have been extracted from reference [8]. It has a value of less than 0.5° beyond 10 TeV, and its median value has been recently lowered to 0.38° by accounting for the behaviour of the optical modules in the reconstruction algorithm. The effective area, which is the ratio between the rate of detected events and the incident flux of neutrinos is shown in the same figure at the right. It is maximum in the declination range $-90^\circ < \delta < -45^\circ$. These results depend on the spectral index of the incident spectrum, which here is -2. The performances in terms of energy resolution are represented in figure 3.7, extracted from reference [40]. Median energy resolutions of $\log_{10}\Delta E \approx 0.45$ for muon energies and $\log_{10}\Delta E \approx 0.7$ for neutrino energies are obtained.

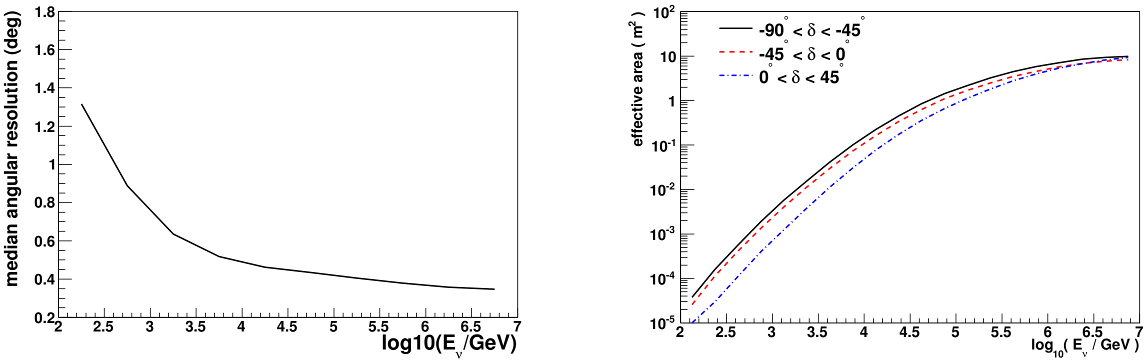

Figure 3.6: **Left:** ANTARES median angular resolution. **Right:** ANTARES effective area for an E^{-2} energy spectrum.

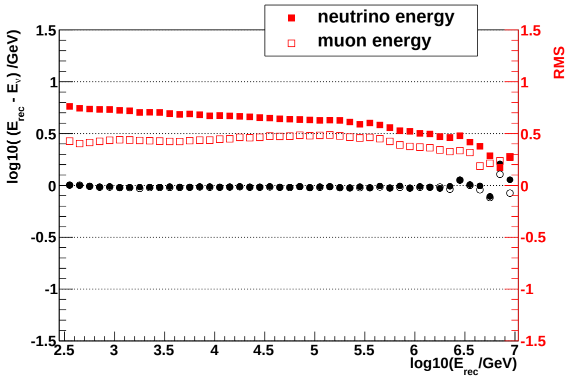

Figure 3.7: ANTARES energy resolution for muon tracks and neutrinos.

Performance for showers

ANTARES design was optimised for the reconstruction of muon tracks because the track channel provides a larger effective area and a better angular resolution. The reason relates to the longer muon path lengths compared to the distances travelled by the electrons. This provides a larger lever arm for the reconstruction and enables the reconstruction of interactions external to the detector, thus extending the effective volume, while showers are mainly contained events. Nevertheless, detecting shower like events is also very important and provides a better neutrino energy estimate since the overall energy of the interaction is deposited in the detector. These advantages allowed IceCube to observe the diffuse neutrino flux published in 2013. The search for cosmic neutrino signal from point-like sources using shower-like events in ANTARES, started recently thanks to the development of a new algorithm which allows to reconstruct the shower directions with an angular resolution of the order of $3\deg$, which was never before achieved. The energy resolution in the interval from 10 to 300 TeV is of the order of 5%. Below 10 TeV the resolution diminishes due to a decrease on the number of detected photons and for energies over 300 TeV, the emitted light saturates the detector. The angular and energy resolutions for showers are shown in figure 3.8, which has been extracted from reference [1].

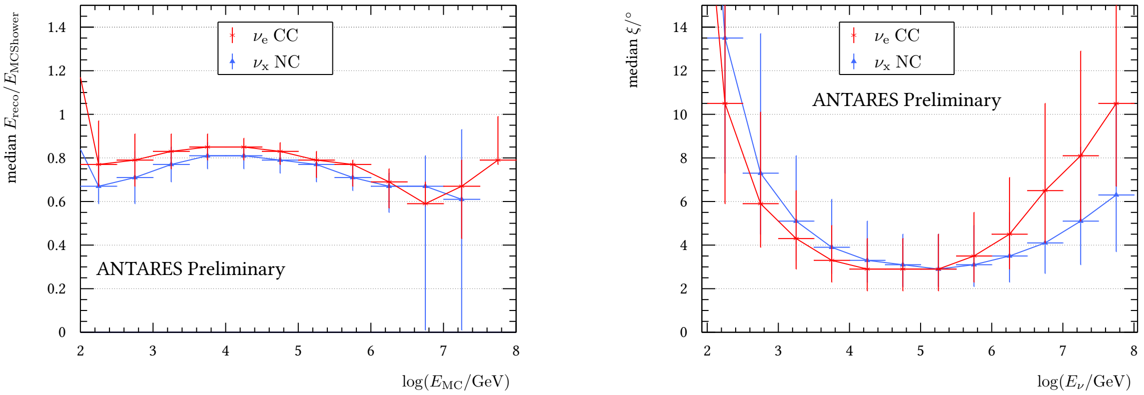

Figure 3.8: **Left:** ANTARES energy resolution for showers. **Right:** ANTARES median angular resolution for showers.

3.3.2 Search for point like and extended point sources

The main search channel for high energy neutrino astrophysical sources is the search for an excess of energetic muons produced by the ν_μ interactions near the detector. The non negligible flux of downward going atmospheric muons, constrains this search to sources located in the southern sky. The main background is the flux of atmospheric neutrinos, and some atmospheric muons mis reconstructed as upward going events. As previously mentioned, the scattering length in water allows to achieve a median angular resolution of $\sim 0.38°$ for tracks for an E^{-2} energy spectrum. The sensitivity for the sources located in the southern hemisphere is therefore excellent. A summary of the latest results can be found in references [1].

Joint search with IceCube

The track-like events reconstructed by ANTARES from January 2007 until December 2012 have been combined with the IceCube data recorded between April 2008 and May 2011 in a single analysis. Figure 3.9 shows the fraction of events of astrophysical origin potentially present in each data set for an E^{-2} spectrum. As one can see, the ANTARES contribution for directions $< 15^\circ$ is not negligible. As figure 3.9 shows, the combined analysis over all the southern sky improves the results obtained independently by each experiment, putting in evidence the complementarity of both detectors.

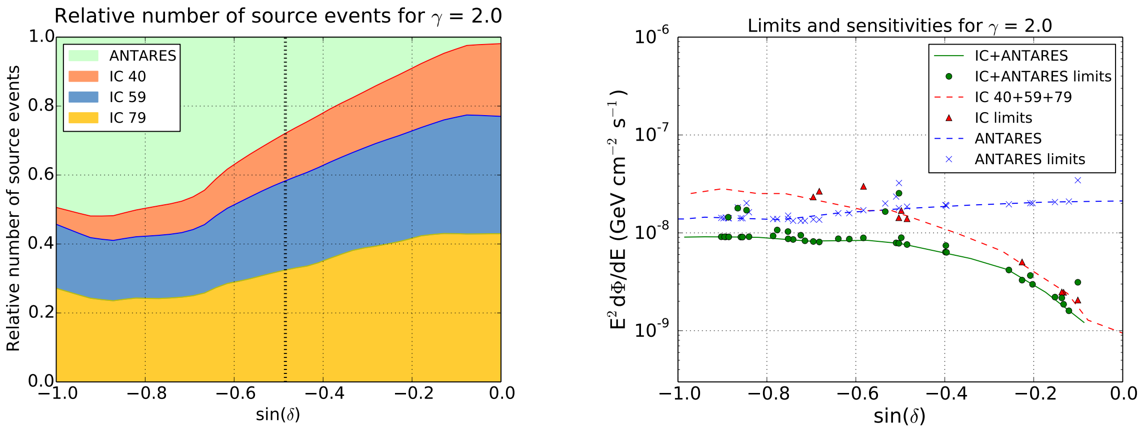

Figure 3.9: **Left:** Contribution from each data set to the ANTARES-IceCube combined analysis. **Right:** Sensitivities and limits for an E^{-2} spectrum with ANTARES, IceCube and for the combined data sets.

Constraints over the origin of the IceCube High Energy Starting Events (HESE)

After the IceCube discovery, it has been proposed that the accumulation of HESE events near δ = -29° could have been produced by a single point source. Confirming that origin is impossible by just using the IceCube data because the IceCube angular resolution is not good enough. The non detection by ANTARES of a point-like source in this region of the sky has allowed to constrain the flux of a point source as a function of its spectral index, as it is shown in figure 3.10. For the spectral index that best reproduces the IceCube data (γ =2.5), these results show that no more than 2 HESE could have been produced by the same point-like source.

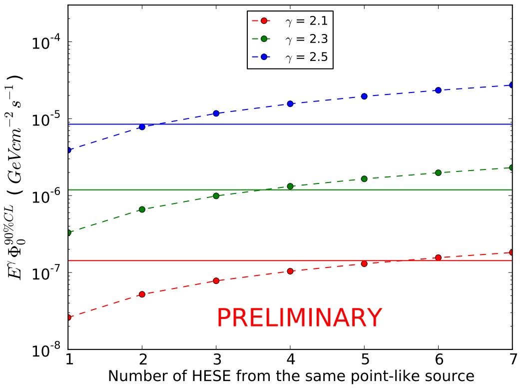

Figure 3.10: ANTARES 90% confidence level limits (flat lines) over the contribution of point sources to the IceCube HESE events, for different spectral indices and a source located at $\delta = -29^{\circ}$, corresponding to the slight excess observed by IceCube, compared to the flux needed to produce a certain number of HESE events.

Galactic plane

The interactions of the cosmic rays from the milky way with the interstellar medium produces pions, and therefore neutrinos. Evidence for these processes has been provided by the Fermi/LAT observations of the diffuse γ ray background in the galaxy. Also, the number of events of astrophysical origin observed by IceCube above 100 TeV in the direction of the galactic plane is compatible with the flux observed in the γ domain as it is shown in figure 3.11. A search for neutrinos from the galactic plane has been performed by ANTARES, without leading to a significant excess. This has allowed to exclude at a 90% confidence level, the hypothesis of a simple one-to-one relation between the gamma and neutrino fluxes coming from the galactic plane.

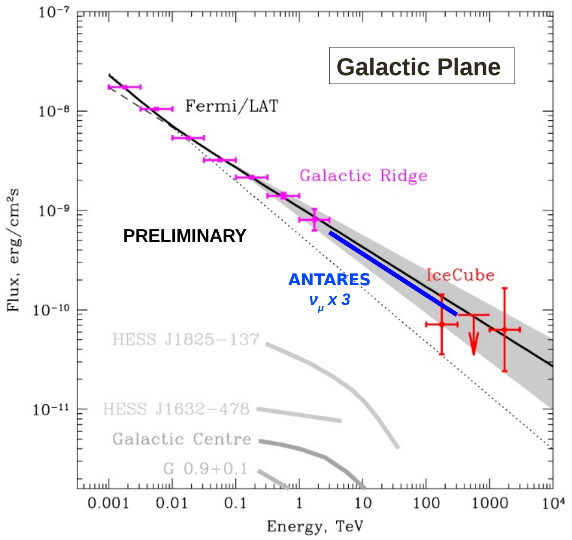

Figure 3.11: Gamma flux detected by Fermi/LAT in the direction of the galactic plane (pink), and the flux corresponding to the IceCube events in that direction, compared to the limits including all neutrino flavours be ANTARES.

The Fermi Bubbles

The so-called Fermi bubbles, which are represented in figure 3.12, are zones of gamma ray emission extending outwards the galactic plane which are thought to be a possible source of accelerated cosmic rays, and therefore, where high energy neutrinos can also be produced in nucleon-nucleon interactions. ANTARES has performed a search for neutrinos coming from this region, which relies on an ON-OFF method: an excess of events is searched for with respect to zones of equivalent coverage as the Fermi bubbles, but not coincident with the Fermi bubbles (zones "OFF"). Different spectra and energy cuts have been considered. A small excess of 1.96σ significance has been found in the Fermi bubbles zone ("ON" zone), which is still compatible with background. The results are shown in figure 3.12.

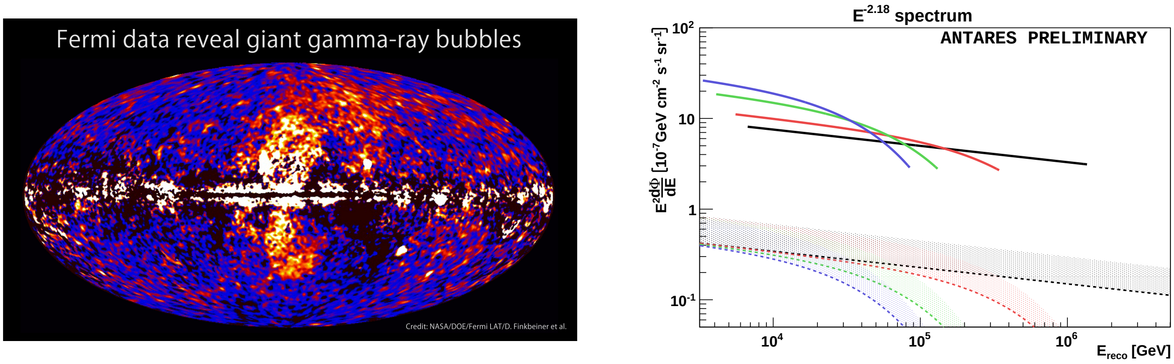

Figure 3.12: **Left:** Gamma ray bubbles as viewed by Fermi. **Right:** 90 % confidence level limitsover the neutrino flux coming from the Fermi bubbles, compared to the theoretical predictions (colored zones), for different energy cuts at 500 TeV, 100 TeV, 50 TeV, and without a cut (black).

3.3.3 Multi-messenger searches

Identifying the sources of the neutrino flux detected by Icecube is not an easy task. Besides searching for an excess at high energies (as IceCube has done) or for an accumulation, justified by astrophysical arguments, of events in a particular direction, another solution is to search for space and time correlations with transient astrophysical phenomena detected by instruments which are sensitive to different wavelengths of the electromagnetic spectrum, or to non-photonic messengers such as gravitational waves.

AGN and X-ray binaries

By using multiwavelength observations, the TANAMI collaboration has identified several bright blazars in the 50% error band of the reconstructed directions of the two PeV neutrinos detected by IceCube (IC14 and IC20) [1]. ANTARES has reported the observation of neutrino candidates in the directions corresponding to the two blazars closest to IC20, observation which is compatible with background fluctuations. But the absence of neutrino candidates in the direction of IC14, allows to exclude an E^{γ} flux with γ <2.4 as the origin of that particular event. In addition, the most energetic IceCube event (IC35), was detected during a flare from the source PKSB1424-418, which lays in the 50$\%$ error band of IC35. ANTARES observed only one event at a distance closer than $5\deg$ from this source, while 3 were expected from background.

In another analysis, ANTARES has searched for neutrinos in coincidence with 41 flares from blazars reported by Fermi/LAT and 7 flares reported by HESS, MAGIC, and VERITAS observatories, for photons beyond the TeV. The results obtained for the source 3C279 are shown in figure 3.13.

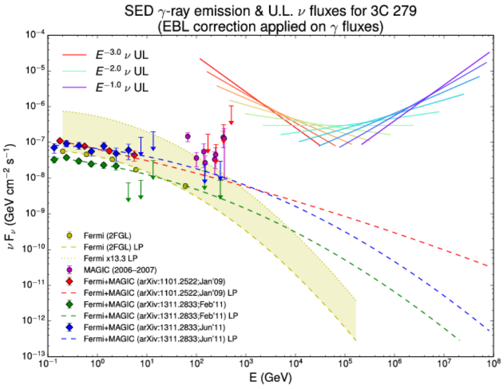

Figure 3.13: Limits over the neutrino flux coming from the blazar 3C279 for different spectral indices, compared to observations (points), and extrapolations at high energies of the spectra measured by Fermi and other ground based instruments.

X-ray binaries are a class of binary stars with a particularly high emission in the X-ray band. The emitted photons are thought to be originated in the accretion of matter from the donor star onto the dense companion, which can be a white dwarf, a neutron star or a black hole. These systems are called "high mass" or "low mass" depending on the mass of the donor star. Jets have been observed by radio surveys in certain cases, where in three particular cases Ni and Fe lines have been observed, revealing the presence of hadronic processes. A total of 34 binaries observed in the X or gamma bands, some of them microquasars, have been analysed by ANTARES during their periods of most intense activity. The results for 2 of them are shown in figure 3.14. In the case of GX339-4, the most optimistic models, in which the ration proton/electron is ≈ 100, can be excluded by the non observation by ANTARES.

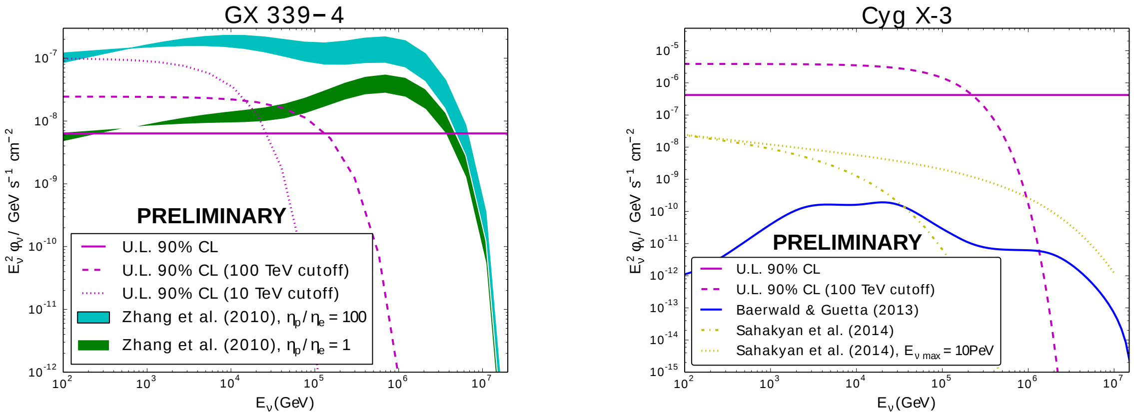

Figure 3.14: **Left:** Upper limits on the neutrino flux for the binary GX 339-4 with and without an energy cut, compared to the theoretical estimations for spectral indices between 1.8 and 2, and a proton/electron ratio of 1 or 100. **Right:** Limits for Cyg X-3 wit and without cut at 100 TeV compared to theoretical estimations.

Gamma ray bursts (GRB)

In the fireball model, the electromagnetic emission observed during these short and intense bursts of gamma photons, are produced by synchrotron radiation and posterior inverse Compton scattering by electrons accelerated in the internal shocks of a relativistic jet. The detection of neutrinos associated to these phenomena, could prove the presence of accelerated hadrons in the jets.

ANTARES has searched for high energy neutrinos from GRB based in two different models (see reference [1]): the NeuCosmA model accounts for the p-γ cross section and all the associated processes. As well, a photospheric model has been considered in which the neutrinos are emitted closer to the core, where the jets are opaque to photons. For each model, the expected signal is simulated GRB by GRB and the detector response and background are modelled by using the exact data taking conditions at the moment of each GRB.

The NeuCosmA based analysis has been applied to a total of 296 GRB observed between 2007 and 2011, without any significant correlation. In particular, for the GRB 110918A, which was particularly energetic, and for the GRB 130427A, which was particularly close, a dedicated analysis was done. No coincident neutrinos were found but this non observation has allowed to constrain certain parameters from the relativistic jet, in particular, its lorentz factor and its baryonic content. The results are represented in figure 3.15.

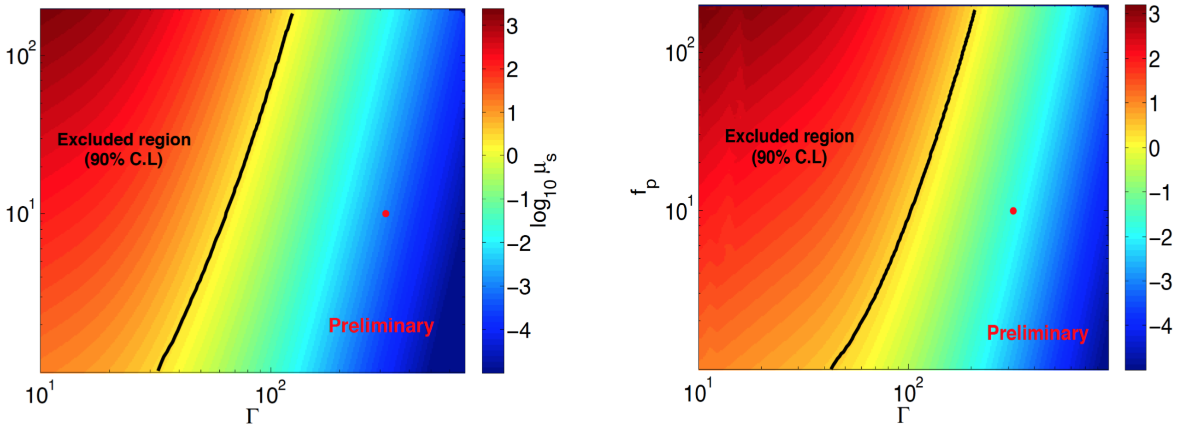

Figure 3.15: Number of expected neutrinos as a function of the Lorentz factor Γ, and of the barionic charge f_p. **Left:** GRB130427A **Right:** GRB110918A. The black line indicates the region excluded by ANTARES with a 90% confidence level, and the red point indicate the most habitual values of these parameters for long GRB.

Electromagnetic follow ups

The TAToO program (Telescopes and ANTARES Target of Opportunity), performs a real time reconstruction of muon tracks. If the event has a high estimated energy (∼100 TeV), or if several muon tracks are observed within a short time window from close-by directions, an alert is sent to telescopes operating in different wavelength bands. The goal is to find an electromagnetic counterpart to a high energy neutrino candidate.

The generation of the alert is done in a matter of seconds, and the electromagnetic follow up takes around 20 seconds in the case of the optical telescopes, and around 1 hour in the case of the rest of the telescopes. A total of 221 alerts have been set to optical telescopes since 2009, 12 to X-ray telescopes since 2013, 14 to radio telescopes, and 2 to the HESS gamma observatory since 2015. No significant counterpart was reported for any of the alerts.

Gravitational Waves

Besides sharing similar scientific goals, gravitational waves detectors and neutrino telescopes share another characteristic: both detectors suffer from an important source of background which make the detection of signal a very difficult task to achieve. Since the sources of background for neutrino telescopes and gravitational wave detectors are independent from each other, combining the data from both instruments enables to increase their individual sensitivities. The detection of a gravitational wave event by the LIGO and VIRGO detectors during September 2015 was a very important step in astroparticle physics, since it was the first statistically significant gravitational wave event ever detected. The location of the potential source is constrained with a 90% confidence level to an area subtending 590 squared degrees. Prior to the detection of that event, a memorandum of understanding existed between ANTARES, IceCube and the LIGO and VIRGO collaborations, who accordingly to such agreement informed both neutrino collaborations about their detection in order to perform a follow up. IceCube found 3 events within the source location area during a time window of $\pm$500 s centred in the detection time of the gravitational wave, while $\sim$ 2.2 background neutrinos and 2 atmospheric muons were expected. ANTARES found no candidates, while $\sim$ 0.014 atmospheric neutrinos were expected in the same time window. Therefore, both results are consistent with the background fluctuations and constraints have been set to the neutrino emission from the gravitational wave event [12].

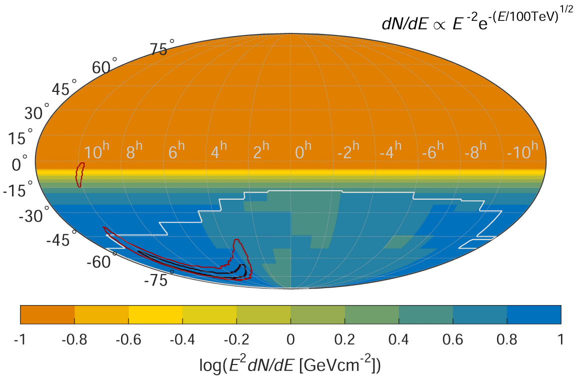

Figure 3.16: Upper limit on the high-energy $\nu_\mu + \bar{\nu}_\mu$ spectral fluence from GW150914 as a function of the source direction. The region surrounded by a white line shows the part of the sky where ANTARES is more sensitive (close to the nadir), while on the rest of the sky IceCube is more sensitive. For comparison, the 50% and 90% CL contours of the GW sky map are also shown (red and blue lines on the bottom left)

Figure 3.16 shows a sky map with the area containing the source of the gravitational wave, and the limits to the energy emitted in neutrinos for an E^{-2} spectrum with an energy cut at 100 TeV. A similar analysis with similar results has also been performed for a second gravitational wave event, the GW 151226.

Part II

The ANTARES neutrino telescope

Chapter 4

The ANTARES detector

4.1 Introduction

The ANTARES collaboration was formed in 1996, and nowadays gathers around 150 physicists, engineers, oceanographers and astronomers from about 20 institutions distributed around France, Germany, Italy, Morocco, Netherlands, Romany, Russia and Spain [14].

The detector, located 40km offshore from Toulon (42º48' N, 6º10' E) and anchored at 2475m depth, was completed on 29 May 2008 and it is the largest neutrino telescope in the northern hemisphere and the first to operate in the deep sea. Its deep underwater location ensures a partial shielding against the atmospheric muons, and its location in the northern hemisphere makes of ANTARES a privileged observer of the galactic plane. The scattering of the Cherenkov light in water is limited, which allows to reconstruct the muon trajectories (and hence the neutrino directions) with a good precision.

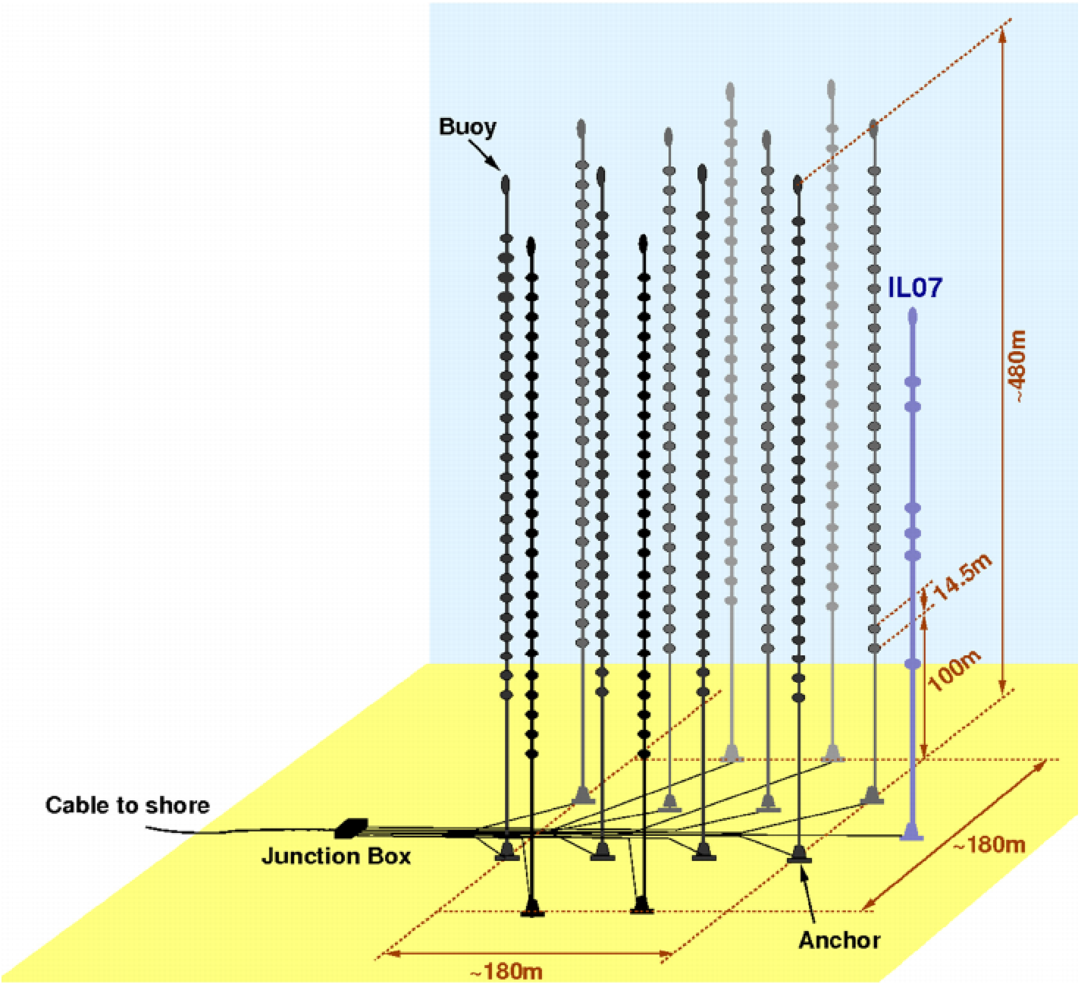

Figure 4.1: Schematic view of the ANTARES detector.

4.2 Detector description

The detection of the Cherenkov light induced by the relativistic charged particles is done with a three dimensional matrix of light detectors as shown in figure 4.2, called optical modules (OM). An OM consists of a 10" hemispherical Hamamatsu photomultiplier (PMT) which is housed in a glass sphere resistant to compressive stress. The "front" hemisphere of the OM is transparent and is coupled to the PMT with optical gel. Also fixed by the optical gel, a magnetic shield is placed in the front hemisphere surrounding the photo-cathode in order to attenuate the effect of the Earth's magnetic field on the functioning of the PMT. The "back" hemisphere is painted black and contains a drilled hole where the OM electrical connexion is housed.

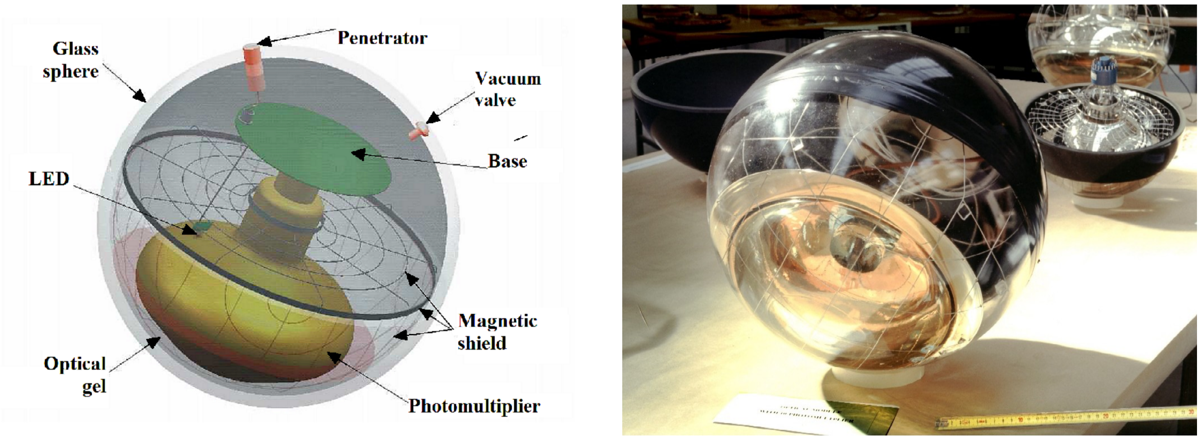

Figure 4.2: **Left:** Schematic view of the different components of an OM. **Right:** A picture of an OM

The OMs are arranged three by three into nodes called storeys as shown in figure 7.3. In a storey the OMs are held pointing downwards 45^o by a vertical titanium frame called optical module frame (OMF). The OMF also holds a local control module (LCM) which is a titanium container that hosts the electronics needed for data taking and transmission. Storeys are connected to each other with Electro-Mechanical Cables (EMC) forming lines. The EMCs contain electrical wires used for power supply, and optical fibres used for data transmission. In its nominal configuration, a line consists of 25 storeys each of them separated by a distance of 14.5 m and the lowest one separated by 100 m from the sea bed. In order to reduce the risk of failure for a full line, the lines are divided into 5 sectors of 5 successive storeys each. Concerning the data transmission and power supply, sectors are independent from each other. Each line is anchored to the sea bottom by a Bottom String Socket (BSS) and is kept tight by a top buoy and by the intrinsic buoyancy of the OMs. In its final configuration, ANTARES consists of 11 lines in their nominal configuration and a twelfth with 4 sectors, the fifth being completed by instruments dedicated to acoustic detection which are part of the AMADEUS project [14]. The distribution of the external lines in the sea bed is octagonal and each of them is separated by a distance of 60 m from its nearest neighbours. An extra instrumented line called IL07 was deployed, also equipped with acoustic detection devices as the top of the twelfth line, and devices to measure the environmental conditions. Each line's BSS is connected to a Junction Box (JB) which provides power to the detector, and which is connected to the control room by a $\sim$ 40 km long cable called the Main Electro-Optical Cable.

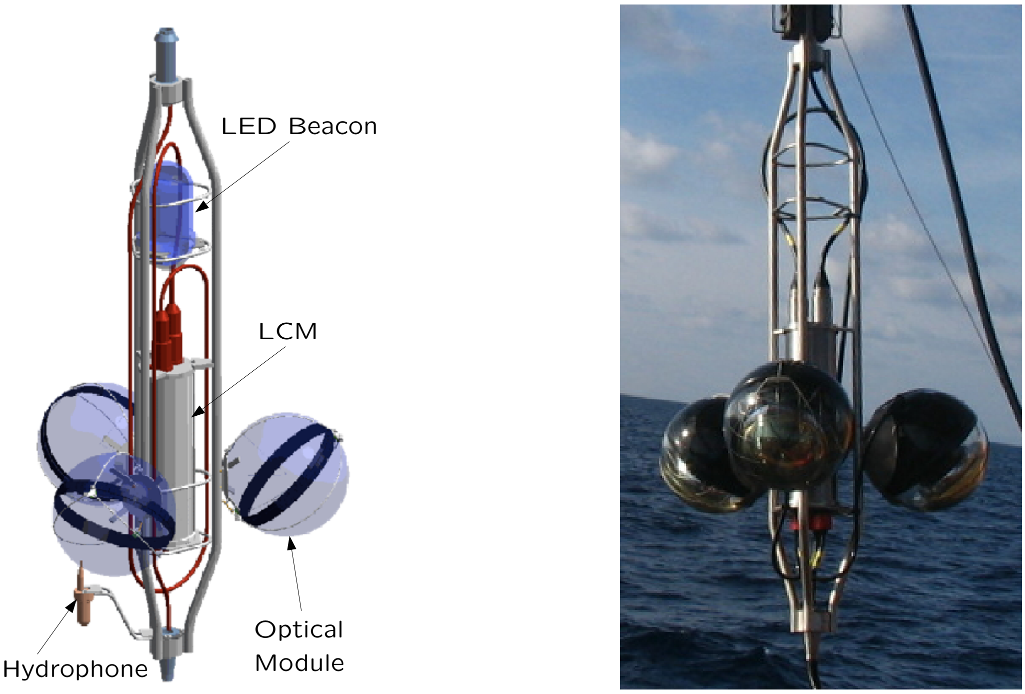

Figure 4.3: **Left:** Schematic view of a storey. **Right:** Photograph of a storey taken during the deployment stage.

4.3 Data acquisition

The ANTARES data acquisition system converts the analogue signal of the PMTs into digital data, transports the digitized data to shore, filters the relevant data from background, and stores the filtered data on disk. The data acquisition rate is typically of the order of 1 Gb.

per hour. Fluctuations occur due to variations in the optical background level, as well as to the different filtering algorithms (described in section 4.3.3) that can be applied. Data are recorded in runs of a few hours (up to 12) which are transferred and stored ar the computing center of Lyon (CCIN2P3) every night.

4.3.1 Offshore signal digitisation

The first step in the data acquisition chain is the processing of the analogue signal provided by the PMTs. This is done by a custom ASIC chip called Analogue Ring Sampler (ARS) and includes the digitisation of the timing of each PMT signal and the total charge of the pulse, which is integrated over an adjustable gate of typical width 35 ns. A voltage threshold can be set in the ARS in order to eliminate the small pulses due to the PMT dark current and to remove the electronic noise. The typical value of the voltage threshold corresponds to 0.3 photo-electrons. Provided that the PMT analogue signal is above the voltage threshold, a local clock time-stamps the threshold crossing that is further digitised by an Analogue to Digital Converter (ADC). The combined time and charge information of the PMT signal, both being digitized by two embedded Analog to Digital Converters (ADC) is referred to as a level 0 (L0) hit. Given that the digitization process by the ARS lasts around 200 ns, two ARS chips are connected to each PMT in order to reduce the dead time introduced by the signal processing.

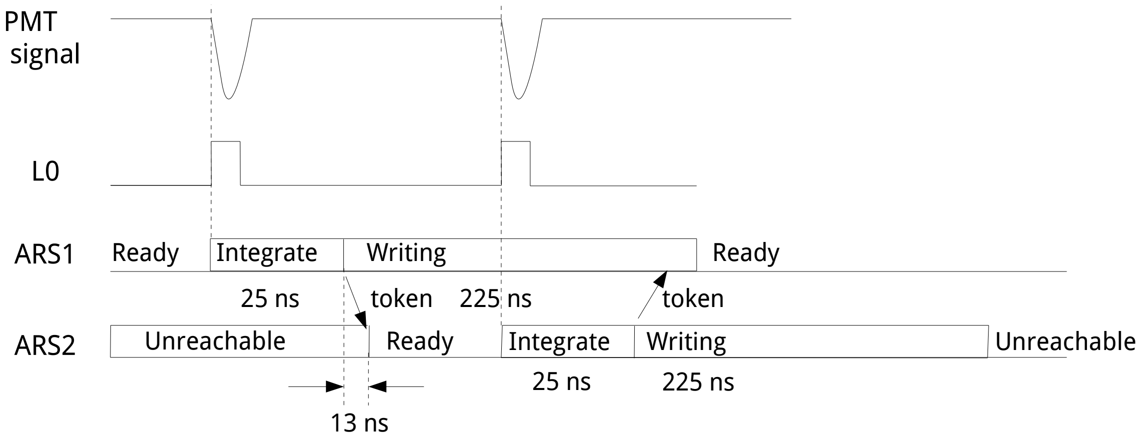

Figure 4.4: Representation of the token ring protocol, used to reduce the dead time introduced by the digitization of the signal of an OM.

The so-called token ring protocol is used to chain the two ARS chips associated to a given OM. Each ARS contains a register named "token" whose value defines its availability to integrate an incoming event. An ARS will treat an incoming event when its token is set to 1 (in which case it is said that the ARS owns the token), and ignore it otherwise. At any given time, only one of the two ARSs can own the token, and the token is passed from one ARS to the other after the integration gate with a delay time of 10-20 ns. The ARS system digitization process for a PMT is shown in Figure 4.4. The readout of the 6 ARS chips in an LCM is done by an field-programmable gate array (FPGA) board, which groups the L0 hits into time frames (TF) of 50×2^{21} ns $= 104.8576$ ms. The main components of an LCM are depicted in Fig 4.5.

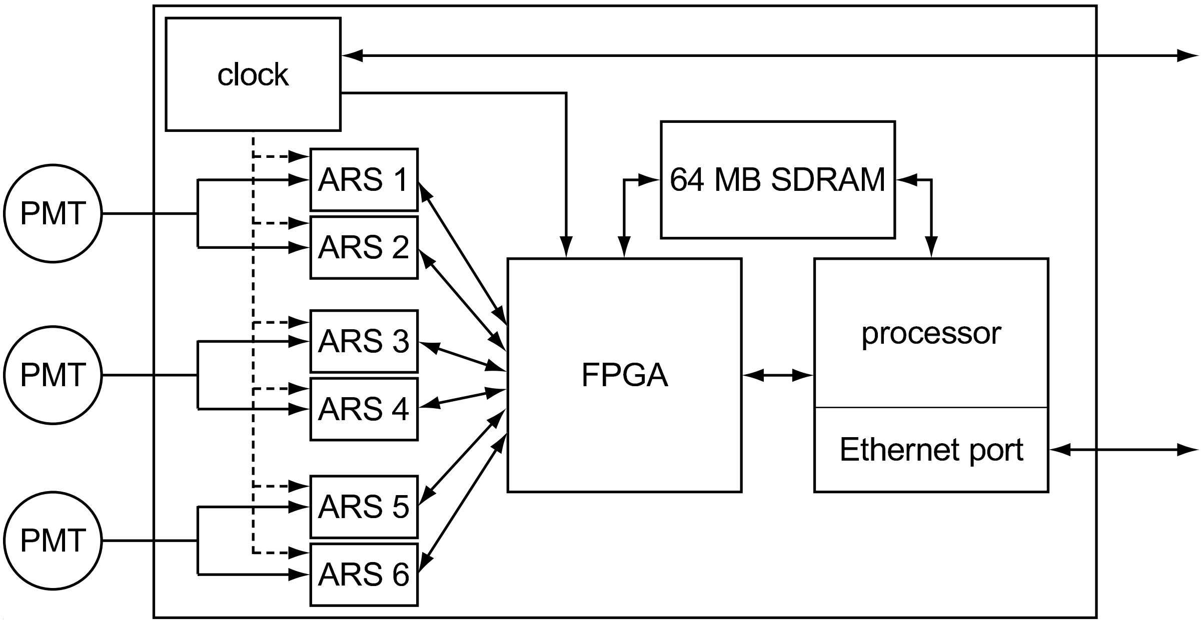

Figure 4.5: Main components of the LCM which process the signal of 3 OMs

4.3.2 Data transmission onshore

The data transmission to shore is done following the "all-data-to-shore" philosophy. This means that all the digital photo-electron hits are transferred to shore without any off-shore data selection. In this way, all the raw data are processed on shore, minimising the overall loss of physics signal and allowing for different processing methods to be applied for specific physics analyses.

This is done following the pipeline shown in Fig 4.6. In each LCM electronic module, a processor equipped with a 100 Mb/s Ethernet port acts as an interface between the ARS chips and the online data processing system. The LCM on every fifth storey in a string, called Master Local Control Module (MLCM), acts as a master for the other LCMs in the sector and contains an Ethernet switch where the Ethernet links from 5 storeys are connected by a bidirectional 100 Mb/s Ethernet link. Each MLCM is connected to an electronic container situated in the BSS, called String Control Module (SCM). These connexions are made by using the Dense Wavelength Division Multiplexing technique (DWDM) [91], which allows multiple information streams to be transmitted simultaneously through a single optic fibre by using different wavelengths for each stream. Finally, each SCM is connected to the JB via an interlink cable (IL), and the JB is connected to a PC farm in the shore station through the main electro-optical cable. These connections required the intervention of a remotely operated vehicle (ROV).

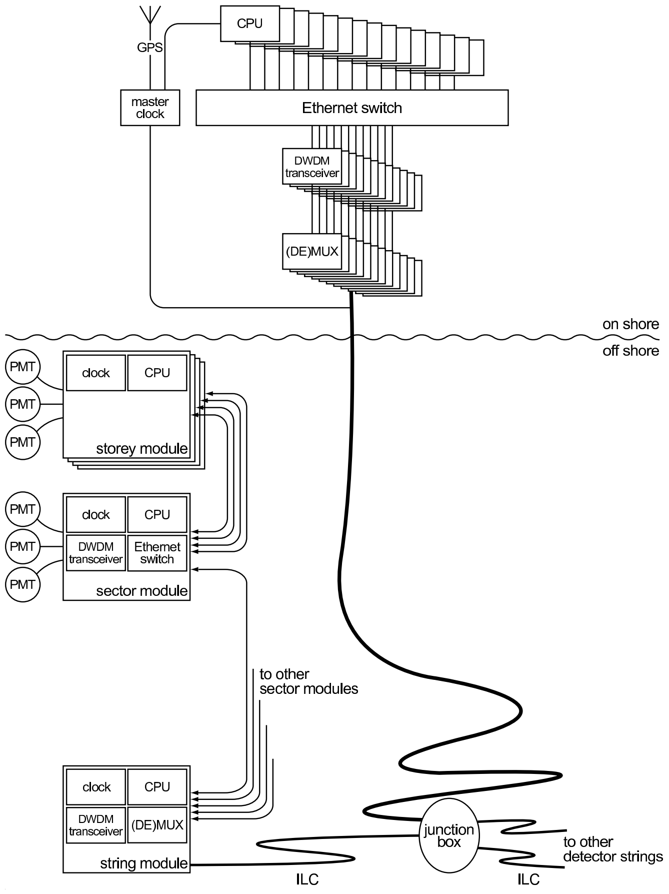

Figure 4.6: Schematic view of the ANTARES data acquisition system hardware of one detector string.

4.3.3 Data filtering

Due to the high rate of L0 hits arriving onshore, it is necessary to apply a filter in order to discard those that are likely to originate from the optical background. While those hits are produced in stochastic processes and are expected to be produced independently from each other, L0 hits produced by the passage of relativistic charged particles are expected to be correlated in space and time. The DataFilter software that runs on the PC farm onshore, is in charge of searching for groups of correlated L0 hits. The data corresponding to large enough groups of correlated L0 hits are recorded on disk for further processing, while the rest is discarded. In the following text, a description of the data filtering processes is given.

The L0 hits arriving onshore are organised in time slices. A time slice has the same duration as a frame ($\sim$ 104 ms as explained in 4.3.1), and contains the information of all the frames that correspond to the same absolute time. In other words, a time slice contains the L0 hits digitized by all the ARS chips in the detector during $\sim$ 104 ms. Each time slice is processed by a single PC where the DataFilter program selects events by applying a three level hit selection. This process is illustrated in figure 4.7.

As a first step one assumes that within a 20 ns time window, the optical background will not often produce more than a single L0 hit with a charge higher than 1 photo-electron. Therefore, single L0 hits with a high charge (typically $>$ 2.5 p.e.) and couples of L0 hits occurring within a 20 ns time window on two different OMs in the same storey are selected. The hits passing this filtering step are called level 1 (L1) hits.

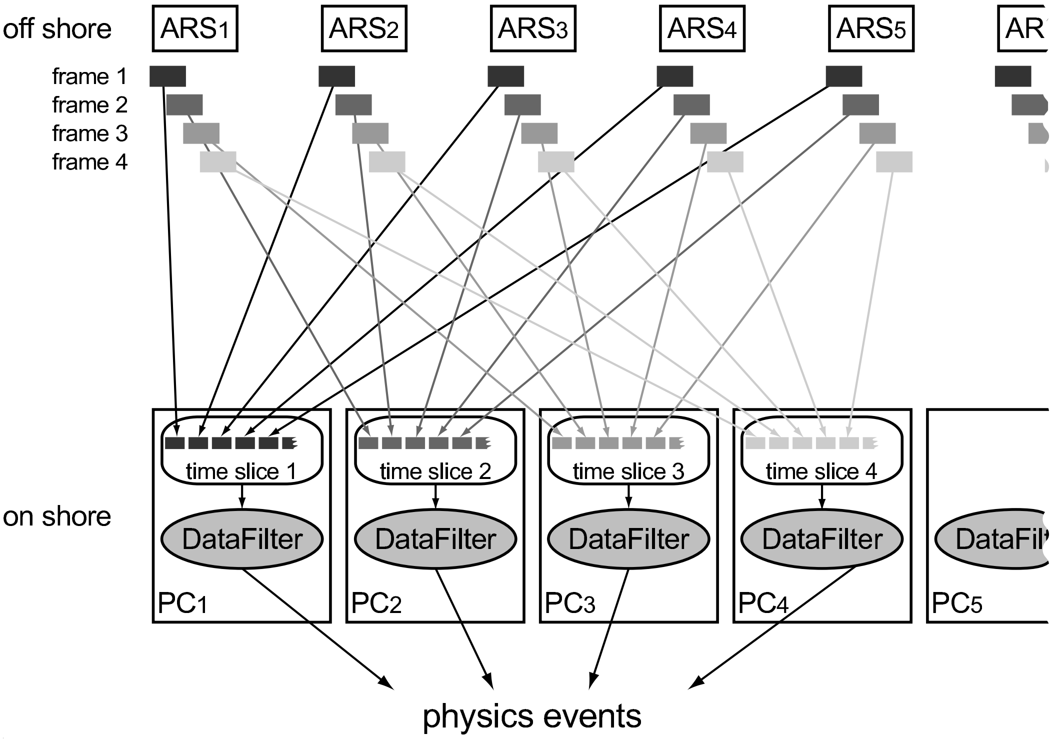

Figure 4.7: The processing of the data based on time slices. All frames belonging to the same time window are sent to a single PC and form a time slice. The DataFilter program running on each PC processes the data in the time slice. All physics events are stored on disk.

A second filtering step is carried out over the L1 hits by selecting those that are causally connected. A couple of hits $\mathrm{L1}_i$ and $\mathrm{L1}_j$, where each of them is characterized by a position and a time (r_i, t_i) and (r_j, t_j), define a space-time interval $\Delta s^2 = \Delta r^2 - c_w \cdot \Delta t^2$ (where $c_w = c/n$ is the speed of light in water, and n is the refraction index of water) and are causally connected if $\Delta s^2 \leqslant 0$. In such a case, their order in time is invariant under a change of observer. Therefore, the second step consists on selecting L1 hits that satisfy the following relation

$$|t_i - t_j| \leqslant |r_i - r_j| \cdot \frac{n}{c} + 20ns \tag{4.1}$$

where an extra time of 20 ns has been added to account for the effect of the electronics and light scattering in water. A group of hits that satisfy eq. 4.1 is called a cluster.

The final step in the data filtering is applied only to the L1 hits in a cluster. The so-called **3N trigger** consists on constraining the causal relation between L1 hits with respect to eq. 4.1 by accounting for the pattern of the Cherenkov light emission induced by a muon track. The relation between the times and positions of hits caused by a muon track can be deduced from Fig 4.8, where a muon travelling in the z direction in the detector reference frame coordinates is depicted. If the time origin is set at t_0, the time at which a Cherenkov photon arrives at an OM is given by

$$t_i = t_0 + \frac{1}{c}\left[(z_i - z_0) - \frac{r_i}{\tan\theta_c}\right] + \frac{n}{c}\frac{r_i}{\sin\theta_c} \tag{4.2}$$

where r_i is the distance from the muon's direction to the OM. Using $n \simeq (\cos\theta_c)^{-1}$, the difference in the arrival times of two photons at two OMs can be written as

$$|t_i - t_j| = \frac{|z_i - z_j|}{c} - \frac{|r_i - r_j|}{c} \cdot \tan\theta_c \tag{4.3}$$

From Fig 4.8 one can see that the time difference defined by eq. 4.3 is maximum when the muon trajectory lays in the same plane as the OMs, in which case the term $|r_i - r_j|$ reaches its maximum value. Therefore, when one accounts for the directionality the causal relation becomes

$$|t_i - t_j| \leqslant \frac{|z_i - z_j|}{c} - \frac{R_{ij}}{c} \cdot \tan\theta_c \tag{4.4}$$

where $R_{ij} \equiv |r_i - r_j|_{max}$. Using eq. 4.4, the 3N trigger searches for clusters of L1 hits in different directions. When a cluster is found with at least 5 L1 hits, a physics event is recorded including all the clustered L1 hits as well as all the L0 hits within an overall time window of the order of 2.2 μs. Note that 2.2 μs is the maximum estimated time that a relativistic muon would need to cross the detector.

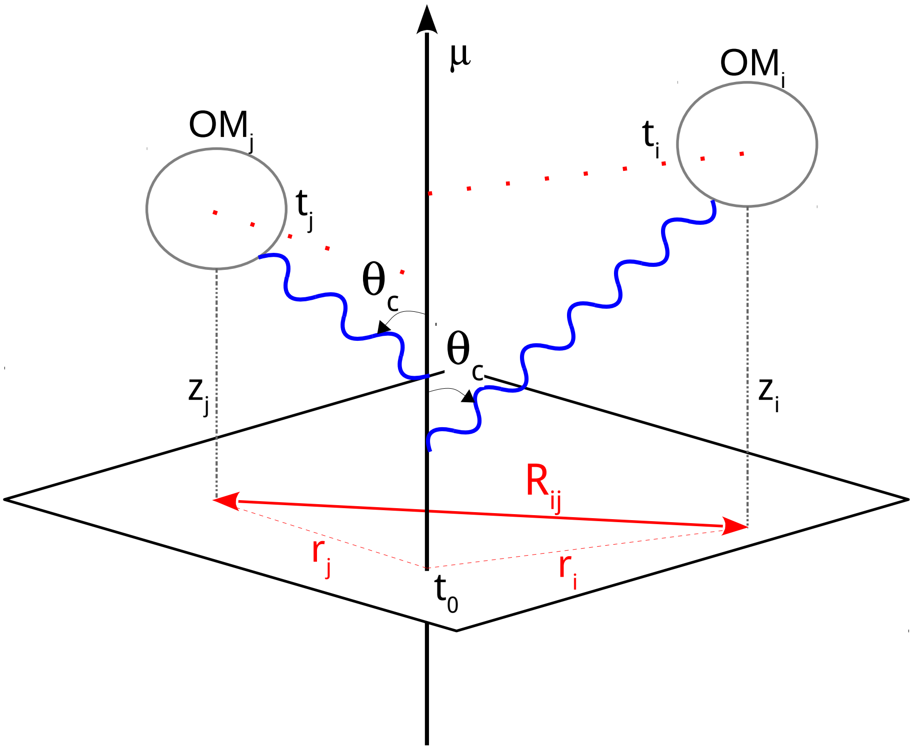

Figure 4.8: Parameters defining the causal relation between two L0 hits as given by equation 4.4 for the passage of a muon track.

The **T3 trigger** doesn't rely on the causal connexion of L1 hits. Instead, it builds on L1 hit clusters by searching for at least 2 L1 hits in adjacent storeys within a time window of 100 ns, or in next-to-adjacent storeys within a time window of 200 ns. Additionally there are other triggers adapted for particular searches. The **GC trigger** is optimized for the detection of neutrinos coming from the Galactic center, and requires one L1 and 4L0 clustered in a direction pointing to the galactic center. The **K40 trigger** demands for 2L0 in the same storey within a time window of 50 ns and it is used for searching for Cherenkov photons produced in the ^{40}K decay (see section 4.7.1). A special trigger called TST is used to search for time correlations with alerts sent by optical and gamma-ray telescopes.

4.4 Calibration

In order to correctly reconstruct the particle trajectories, a precise knowledge of the time and charge information of the L0 hits, as well as a precise knowledge of the OM positions is needed. Accurate measurements of these quantities can only be achieved by calibrating the detector. The present section is devoted to a description of how the calibration of the detector is made.

4.4.1 Time calibration

Performing a time calibration of the detector consists on finding out the time offsets and time resolution of the different OMs including the impact of the electronics on the OMs time resolution.

A master clock located onshore sends a common synchronization signal to the whole detector and can be used to measure the time delays for each LCM. The time offsets of the individual PMTs are measured by using optical beacons and LED pulsers. A LED pulser is housed by each OM (see 4.2) and is used to measure the variations on the transit time of each PMT. The transit time of a PMT is the time elapsed between the arrival of a photon to the photocatode and the signal pulse registered in the anode. Optical beacons of two classes are used to measure the relative time offsets of the different channels. Four LED beacons are installed in storeys 2, 9, 15 and 21 of each line, and two laser beacons are installed in the BSS of two central lines [1]. During special runs, the LED beacons are flashed to illuminate the nearby OMs and the time offset of the OMs is found by comparing the measured and the expected times of the hits. In addition, the two laser beacons are used to cross check the

---

[1] Since the distance from the BSS to the first storey is much larger than the distance between two storeys, a more powerful light source than an LED is required to be located at the sea bed.

time calibration of OMs in different lines.

The time resolution of an OM is given by the dispersion of the time distribution of the PMT signal, which can be written as

$$\sigma^2_{\mathsf{OM}} = \frac{\sigma^2_{\mathsf{TTS}}}{N_{\mathsf{pe}}} + \frac{\sigma^2_{\mathsf{water}}}{N_\gamma} + \sigma^2_{\mathsf{OB}} + \sigma^2_{\mathsf{elec}} \tag{4.5}$$

where σ_{TTS} is the dispersion of the transit time of the electrons from different points in the photocatode to the anode which has been measured in the laboratory and has a value ~ 1.3 ns. σ_{water} represents the chromatic dispersion of the photons in water (which is $\sim$ 1.5 ns for a light path of 40m), σ_{elec} indicates the intrinsic effect of the electronics, and σ_{calib} represents the imprecisions introduced by the calibration system. The measurement of the electronics contribution to the time resolution can be addressed by using light sources that provide high values of N_γ and N_{pe} so that the first two terms of equation 4.5 can be neglected, and whose timing can be controlled at the nanosecond precision so that the third term can also be neglected. In the practice this is done by using the optical beacons situated close to the OMs, and the electronics contribution is measured to be ~ 0.5ns [16], which is well below the uncertainties intrinsic to the PMT.

4.4.2 Position calibration

The relative positions of the OMs will change with the orientation and displacement of the lines, which are not rigid and are affected by the sea currents. The measurements of the positions of the storeys are based on the travel time of acoustic signals. The instrumental setup used to perform such measurements consists on an acoustic emitter located at the BSS of each line and five acoustic receivers which are called hydrophones, situated in storeys 1, 8, 14, 19 and 25 of each line. Since these measurements require a precise knowledge of the sound speed in water, sound velocimeters are also distributed in some lines on the detector. In addition to these acoustic devices, a tilt-meter and a compass housed by every

LCM provide measurements of the pitch, roll and heading of every storey. The data obtained from the acoustic system the compass and the tilt-meter are used to infer the shape of each line, which allows to know the relative positions of the OMs with an accuracy of $\sim$ 10 cm. The absolute geographical position of the detector was determined by the GPS position of the ship used during the deployment of the lines. Its orientation with respect to the sky was measured with an accuracy better than 0.13º in the horizontal direction and better than 0.06º in the vertical direction [9]. This measurement was done with four acoustic beacons located around the detector, which location was measured with respect to the detector and with respect to the GPS position of the ship at the surface.

4.4.3 Charge calibration

As it is explained in section 4.3.1, the ARS integrates the PMT signal, provided that it passes a predefined threshold. As a result of this process, a quantity called AVC is obtained that is related to the number of photo-electrons Q_{pe} recorded by the PMT. The charge calibration is done to find out the correspondence between these two quantities. Laboratory measurements [15] have verified that the relation between these 2 quantities is linear (that means that both the response of the integrator and the ADC are linear). Assuming that this linearity is preserved in the detector site, the charge calibration consists on measuring two points corresponding to zero p.e. (i.e. no signal, which corresponds to the pedestal of the integrator response) and one single p.e., noted respectively $AVC(0pe)$ and $AVC(1pe)$. Since the optical background produces mainly 1 photon, $AVC(1pe)$ is extracted from background hits. Special runs reading the PMT output at random times (so without detected light) allow the measurement of the corresponding $AVC(0pe)$ value. The number of photo-electrons corresponding to a given AVC recorded value naturally follows as:

$$Q_{pe} = \frac{AVC - AVC(0pe)}{AVC(1pe) - AVC(0pe)} \tag{4.6}$$

4.5 Track reconstruction

The analysis presented in the last chapters of this work is based on the reconstruction method described in reference [54], which is optimized for muon tracks. A muon track is characterized by its direction, which can be parametrized as a function of its zenith ϕ and azimuth θ angles $\vec{d} = (\sin\theta\cos\phi, \sin\theta\sin\phi, \cos\theta)$ and the position of the muon $\vec{p} = (p_x, p_y, p_z)$ at a given time t_0. This is, a total of five free parameters. In order to determine these parameters, the mentioned reconstruction method performs different consecutive fitting processes, each of them making use of the results obtained in the previous one in order to improve the accuracy of the results. Basically, it consists on finding the track parameters that maximize the probability (or likelihood) of observing a set of selected hits, $P(\text{hits}|\vec{d}, \vec{p})$. The latest steps of the reconstruction algorithm account for the hit amplitudes, optical background hits and hit time residuals. The performance of the method and the quality with which tracks are reconstructed are given by two variables. The estimated error on the direction of the muon track, is represented by β and measured in degrees. The quality of the reconstruction is related to the value of the likelihood obtained in the maximization process, which is done numerically, and to the number of hits in the event. It is represented by the dimensionless variable Λ. Figure 4.9 illustrates the discriminating power of these variables. The left plot, shows the cumulative distribution of Λ for upward-going events. The three data sets correspond to data corresponding to events reconstructed by ANTARES, and Monte Carlo simulations. One can see that for low values of Λ the sample is dominated by atmospheric muons whose directions have been miss-reconstructed, and mimic upward-going events. An adequate cut on Λ therefore allows to reduce the atmospheric muon contamination. The right plot shows how a cut on the estimated angular error β, has a similar effect.

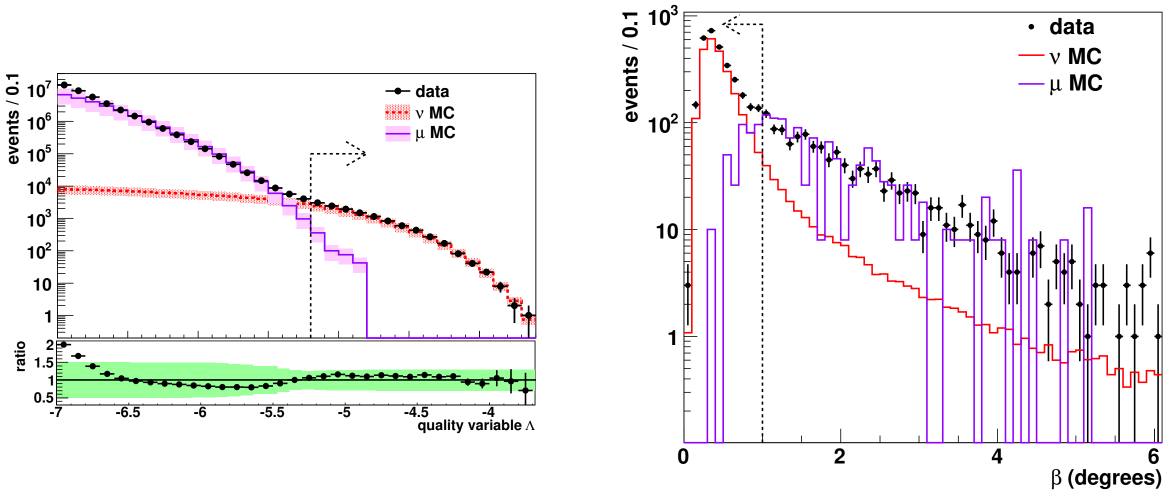

Figure 4.9: **Left:** Cumulative distribution of Λ for upward-going tracks with $\beta < 1^\circ$. **Right:**Estimated angular error for upward-going tracks with $\Lambda > -5.2$. An adequate cut on the variables Λ and β allows to remove downward-going atmospheric muons that are missreconstructed as upward-going particles.

4.6 Energy reconstruction

The energy of the muon tracks can estimated by considering the muon energy losses via pair production or bremmstrahlung processes, which according to figure 5.3 increases with the muon's energy. As it is explained in chapter 5 these losses generate electromagnetic cascades which emit light that can be used to estimate the muon energy loss after propagating a certain distance dE/dX. This is done by adding the amplitudes of those hits with an amplitude larger than 2.5 photo electrons (since they are mainly produced by electromagnetic cascades). The energy of the muons is then estimated from an empirical function which is based on the dependency between E_μ and dE/dX shown in figure 5.3. Since nevertheless, this dependency becomes weak for energies below 1000 GeV, this estimator fails to give an accurate prediction of the track energy in this energy range.

In the last chapters of this thesis, another energy proxy is used, called N_{hit}. This is the number of hits used in the reconstruction of a track. Even if it doesn't provide an accurate value of the energy, a large enough event statistics shows that this estimator allows to discriminate between atmospheric neutrinos and neutrinos whose energy distribution follows a harder spectrum. This is illustrated in figure 7.7 which obtained from Monte Carlo simulations, shows the distribution of hits for neutrinos following an atmospheric spectrum and an E^{-2} spectrum.

4.7 Measuring the PMT efficiency variation using background L0 hits

4.7.1 Optical Background

Every process in which light is produced is a potential source of background for the ANTARES OMs. The detector is located deep enough that the OMs never receive Sun light because it gets completely absorbed by the seawater after several hundreds of meters. Nevertheless, there exist environmental processes in which light is produced, that constitute the so-called optical background. The sources of optical background consist essentially of bioluminescence and natural radioactive decays.

Bioluminescence, is the emission of light by living organisms. This emission happens when an organic molecule, generally called luciferin, is transformed into an excited molecule called oxiluciferin, in an oxidation reaction catalysed by an enzime called luciferase. The photons emitted by the excited oxiluciferin molecules from marine organisms lay in the wavelength range of 450-590 nm, and can therefore mimic Cherenkov photons.

On the other hand, the main source of radioactive decays is the ^{40}K radio isotope. Its lifetime is $\sim 10^9$ years and its main decay channels are two: the 10.72% of the times it decays to stable ^{40}Ar via electron capture and the 89.5% of the times it decays to stable ^{40}Ca through β^- processes. The electrons emitted in the latter processes are energetic enough to create subsequent Cherenkov radiation before getting absorbed. These processes produce L0 hits in the different OMs that can be used to measure the evolution of the counting rates of the different PMTs. The counting rates vary in time due to changes in the environmental conditions such as temperature, biofouling, sea currents... and due to variations in the OM settings (gain or HV variations, thresholds, ageing effects... etc).

After various years of data taking, a decrease in the trigger rate and in the reconstruction rate has been observed, which suggest a potential OM efficiency loss. This loss can be estimated in several ways. In this section, a first study based on the decrease of the counting rates of the PMTs is carried out. First, the necessary ingredients to perform this study are defined. Then, a description of how the counting rate evolution of an OM is estimated, and finally the results for the whole detector are presented.

4.7.2 Baseline and burst fraction

As explained in 4.3.1, L0 hits are arranged into frames of $\sim 104ms$. Therefore, a rate can be computed for each frame by dividing the number of L0 hits recorded by the frame duration. Onshore, these rate values are histogramed every 15 minutes, and the peak of the histogram is fitted to a gauss distribution which mean is stored and called **baseline rate**. The fraction of time during which the rate exceeds the baseline value by at least a 20% is also stored and referred to as **burst fraction**. These data can be found in a data base for every OM in the detector. Figure 4.10 shows the evolution of the baseline and burst fraction with time for an OM during a period of 5 years between 2009 and 2014. One can see the baseline remains stable around 50-60 kHz, except for time periods spanning from the end of April until June, when the rates increase up to several hundreds of kHz. This periodical increase of the baseline rate could be related to an increase of the bioluminescent activity caused by marine organisms that are drifted towards the detector by water currents during seasonal changes [45].

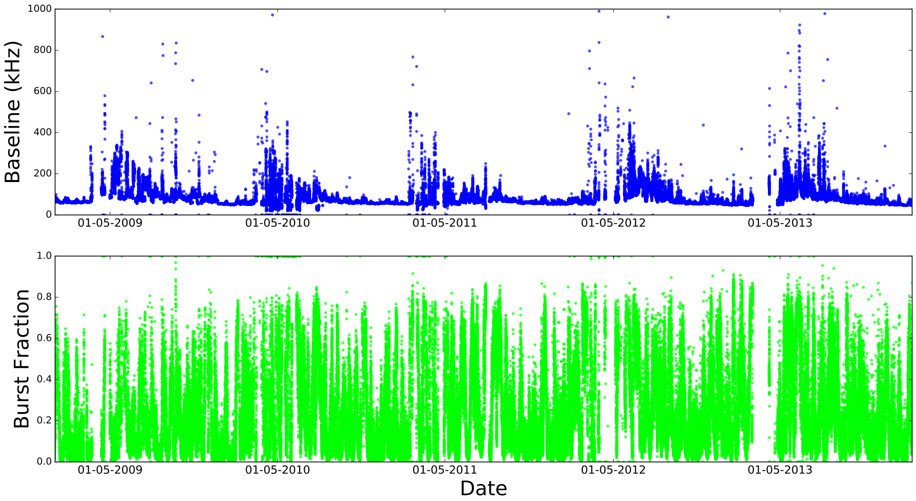

Figure 4.10: Baseline and burst fraction for an OM during the period between 2009 and 2014. Every year during the spring period, the baseline experiences an increase which is believed to be related with an increase of the bioluminescence activity

4.7.3 Using the baseline to estimate the OM efficiency loss

For the same OM presented on Fig 4.10, a cut on the burst fraction was applied and the median baseline rate was computed for every run. Fig 4.11 shows the temporal evolution of this quantity together with a fit to the function

$$f = \alpha \cdot t + \beta + N_1 \cdot e^{\frac{t-t_{01}}{\tau_1}} + \sum_{i=2}^{n} H(t_{0i}) \cdot \left[N_i \cdot e^{\frac{t-t_{0i}}{\tau_i}} - N_{i-1} \cdot e^{\frac{t-t_{0i-1}}{\tau_{i-1}}} \right] \tag{4.7}$$

where the linear term represent the time evolution of the median baseline, and the exponential terms represent the increase of the baseline due to the increase on the high bioluminescence periods. $H(t)$ is the Hevyside step function and each t_{0i} represents the starting time of these periods, at which the baseline reaches values of $\sim N_i$ kHz higher than its value during stable periods. τ_i is the characteristic time constant of this process. β is related to the value of the baseline rate at a reference time, and α represents the linear evolution of the

t_0 (10^6 s)	t_1 (10^6 s)	t_2 (10^6 s)	t_3 (10^6 s)	t_4 (10^6 s)	α (kHz/s)	β (kHz)	N (kHz)	τ (10^6 s)
1240	1272	1304	1339	1370	-0.115 $\cdot 10^{-6}$	205.85	110.01	-5.03

Table 4.1: Result of the best fit for the median baseline rate of the OM shown in figure 4.11.

stable value of the baseline rate with time. For the OM in figure 4.11, equation 4.7 has 17 free parameters. In order to simplify the fitting process, it was assumed that the conditions under which bioluminescence activity increases during spring don't vary from one year to the next one, and the parameters τ_i and N_i were therefore assumed to be constant in time (i.e. $\tau_i = \tau$, and $N_i = N$ for all i). This reduces the number of free parameters in eq 4.7 to 7. The results for the fit shown in Fig 4.11 are shown in table 4.1. The OM efficiency loss can be computed from the parameter α, which in this particular case indicates that the counting rate of the shown OM decreases at a rate of ~ 3.5 kHz/year.

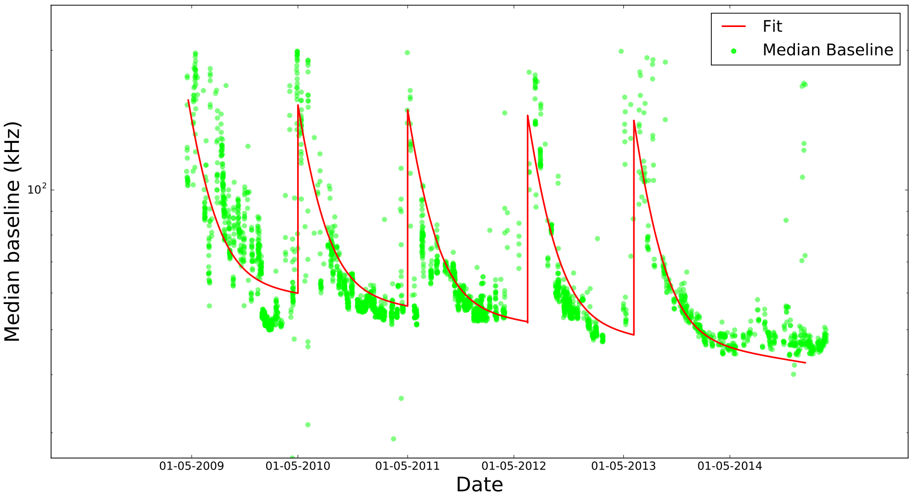

Figure 4.11: Evolution of the median baseline per run for an OM during a 5 year period fitted to equation 4.7. The results of the fit are shown in table 4.1. The value of the paremeter α indicates an overall decrease in the baseline of this OM.

The baseline rate of an OM at a given time $\mathcal{B}(t)$, can be written as a sum of a linear component and a burst component,

$$\mathcal{B}(t) = \mathcal{B}^l(t) + \mathcal{B}^b(t) \tag{4.8}$$

and its efficiency at time t $\varepsilon(t)$, is defined as the ratio of its linear component of the baseline rate at a time t to a reference value $\mathcal{B}_0^l = \mathcal{B}^l(t_0)$ at a time t_0 when the efficiency was assumed to be 1.

$$\varepsilon(t) = \frac{\mathcal{B}^l(t)}{\mathcal{B}_0^l} \tag{4.9}$$

and its variation with time can be written as a function of the fit parameter α as

$$\dot{\varepsilon}\frac{d\varepsilon(t)}{dt} = \frac{1}{\mathcal{B}_0^l} \cdot \frac{d\mathcal{B}^l(t)}{dt} = \frac{\alpha}{\mathcal{B}_0^l} \tag{4.10}$$

Hence, the efficiency of an OM at time t can be written as

$$\varepsilon(t) = \varepsilon(t_0) + \frac{\alpha}{\mathcal{B}_0^l} \cdot dt \tag{4.11}$$

where $\varepsilon(t_0) = 1$.

4.7.4 OM efficiency statistics

A correct simulation of the response of the detector to the passage of particles and to the presence of optical background must include the deterioration of the PMTs with time. A study like the one presented in 4.7.3 has been carried out for all the OMs in the detector. Due to the sensitivity of the fitting tool to a small variation on the parameters of eq 4.7, and due to the large number of OMs in the detector, the parameters τ, N and t_{0i} were fixed in each case to the values obtained in table 4.1. This is a good approximation, since these parameters represent the effect of environmental conditions which are independent of the OMs. For all the OMs the reference time t_0 was arbitrarily chosen to January 2008, corresponding to the early data taking phase of the detector, when no ageing effect should be sizeable visible.

Figure 4.12 shows in units of months^{-1} the distribution of the OMs efficiency variation, and the distribution of the average efficiency variation per LCM. The quantity on the x axis is $-\dot{\varepsilon}$, and is called efficiency loss. These distributions show that the mean OM efficiency variation is negative and around a 0.2% per month. Among all the OMs in the detector, 124 of them are not included in this test, either because they are not functioning, or because their counting rate is so low that not enough data were available to perform the fit described in 4.7.3. One can observe as well that for some OMs the counting rate increases. Such a behaviour was also observed in the laboratory for 1 over 3 OMs tested over ageing stress, although the origin of this effect is not clearly understood.

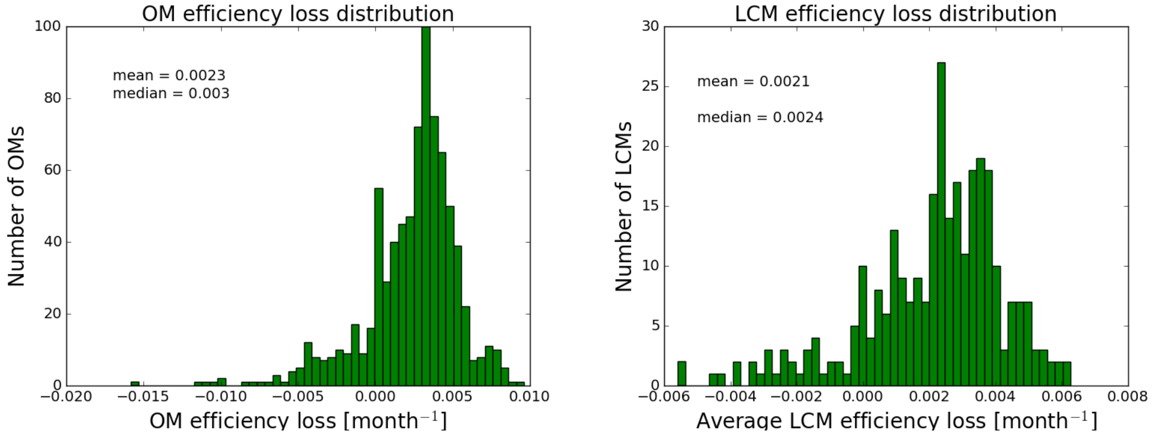

Figure 4.12: Efficiency evolution. The quantity represented in the x axis is efficiency loss, defined as $-\dot{\varepsilon}$. In the left, the OM efficiency loss distribution is shown and in the right the average loss per LCM. In both cases the mean and median values are positive, which implies an overall efficiency loss in the detector.

Figure 4.13 shows the evolution of $-\dot{\varepsilon}$ with the depth in the water, by plotting its average value for storeys and for sectors at the same height. One can see that the deeper the OMs are, less is the variation in their baseline. Nevertheless, alternative efficiency studies based on the hits induced by the ^{40}K decay (described in section 4.7.5) have not confirmed this behaviour.

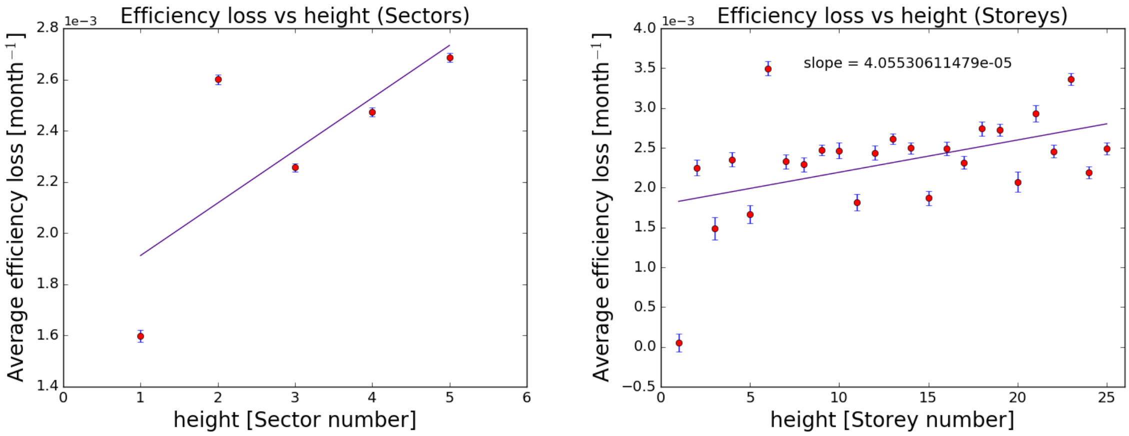

Figure 4.13: Evolution of the efficiency loss with the depth: The average value per sector (left) and the average value per storey (right). 0 is the deepest position. From this figures one concludes that the deeper the OMs are, the less is their efficiency loss.

4.7.5 An alternative study based in the ^{40}K

An alternative calculation of the OMs efficiency loss has been carried out by using the hits produced by the β decay of the ^{40}K into ^{40}Ca. When this process takes place nearby a storey, the Cherenkov light emitted by the out-coming electron can reach two different OMs i and j of the storey within a characteristic window of $\sim$ 50 ns. As mentioned in section 4.3.3, the K40 trigger selects couples of L0 hits within the same storey during this time window and they are stored as K40 hits in the data base. Each K40 hit consists therefore of 2 L0 hits with a time difference of less than 50 ns, in two different OMs i and j from the same storey. During special runs in which the K40 trigger is activated, the rates of coincidences between each pair of OMs is measured and stored in the data base. For each storey three rates are therefore calculated, corresponding to the observed coincident hits between the OMs 1-2, 1-3 and 2-3, and represented by R_{12}, R_{13} and R_{23} respectively. These rate R_{ij} is expected to be related to the efficiencies ε_i and ε_j of the OMs i and j by

$$R_{ij} = R_0 \varepsilon_i \varepsilon_j, \tag{4.12}$$

where R_0 is a normalization rate which value of $R_0 = 15$Hz, was chosen as the mean of the rate of K40 hits recorded by the detector during the period from 2008 to 2014. From this expression, the efficiency of the OMs can be computed as

$$\varepsilon_1 = \sqrt{\frac{1}{R_0}\frac{R_{12}R_{13}}{R_{23}}}, \qquad \varepsilon_2 = \sqrt{\frac{1}{R_0}\frac{R_{12}R_{23}}{R_{21}}}, \qquad \varepsilon_3 = \sqrt{\frac{1}{R_0}\frac{R_{13}R_{23}}{R_{12}}} \tag{4.13}$$

For each OM in the detector, ε was computed on a monthly basis by using the data from the K40 dedicated runs. Figure 4.14 shows how the efficiencies obtained with the baseline rates and with the ^{40}K compare for different OMs in the detector. The results obtained by fitting the baseline rates produce a harder evolution in the OM efficiencies. The impact of both methods in the Data-Monte Carlo comparison is currently under study.

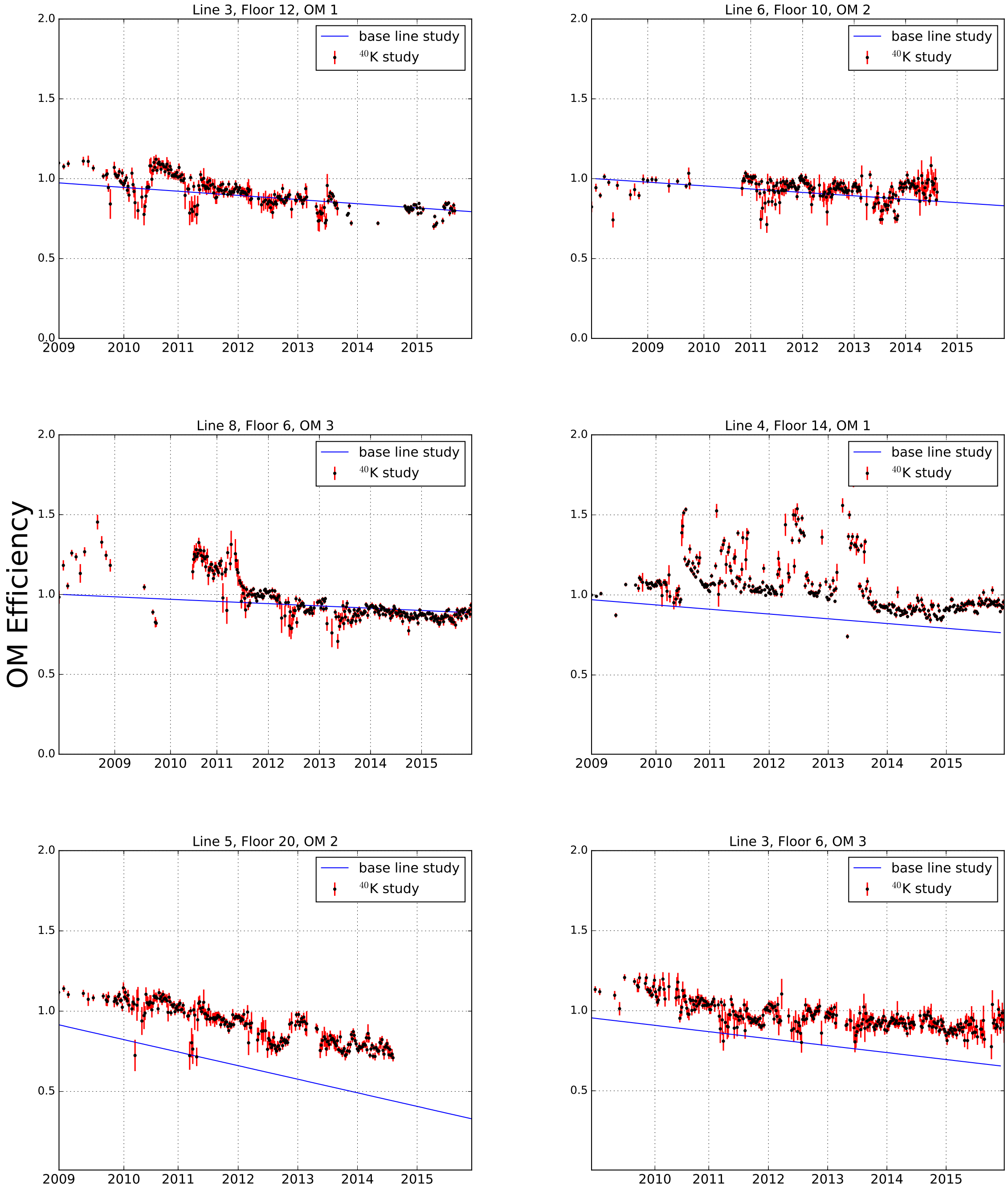

Figure 4.14: Comparison of the results of the efficiency evolution stuties carried out by fitting the baseline rates, and by using the ^{40}K decays.

Chapter 5

Monte Carlo simulations

5.1 Introduction

Science relies on observations that allow testing the predictions about the natural world made by theoretical models. Every experiment is committed to determine whether its observations are in agreement or in conflict with the predictions derived from those models, and therefore, every experiment needs a theoretical reference that predicts, according to the hypotheses to be tested, the imprints that the system under study will leave in the given experimental set up. Comparisons of the observations with these predictions will allow modifying, expanding or rejecting the original hypotheses and develop new theories.

When an experiment deals with the observation of a deterministic system, the theoretical predictions for its outcome can be rather easily obtained from analytical calculations based on a phenomenological model. Particle physics experiments, however, deal with systems of stochastic nature where the amount of particles involved, together with the instrumental uncertainties, make it difficult to predict their outcomes by just using analytical tools. Random number generators allow to account for the stochastic nature of such systems through the Monte Carlo techniques, which constitute a realistic approach for predicting the possible outcomes of experiments.

The signal detected by ANTARES is produced in the last stage of a chain of stochastic physical processes that starts with the production of atmospheric muons and atmospheric neutrinos in the cosmic ray interactions with the atmosphere (as discussed in chapter 3), or with the arrival of cosmic neutrinos to the Earth. Atmospheric muons at the sea level may propagate down through water reaching the detector, and neutrinos may interact with matter in a point sufficiently close to the instrumented volume to produce particles that will induce Cherenkov radiation likely to be detected by the OMs. A completely accurate model for the response of ANTARES to the atmospheric background would require simulating the interactions of the cosmic ray flux in the atmosphere and the tracking of the neutrinos and muons from their production point to the neighbourhood of the detector. Each of the Cherenkov photons induced by the passage of atmospheric muons through the instrumented volume would have to be tracked by simulating its interactions with matter, and the interactions of each of the neutrinos with the matter near the detector would also have to be simulated. Finally, it would be necessary to simulate the full response of the OMs to the arrival of each of the Cherenkov photons. A full Monte Carlo simulation tracking all of these particles would be prohibitive in terms of computing resources: for instance, a rough estimate obtained by integrating equation 3.2, shows that a high energy particle ($\beta = 1$) with $Q = 1$ would produce about 345 photons/cm with λ between 300 and 600 nm. Since muons with energies about ~ 10 GeV can propagate through water distances around ~ 100 m (see for instance, figure 5.2), the simulation and tracking of $\sim 10^6$ photons would be necessary in order to simulate the propagation of a single muon.

The response of ANTARES to the previous processes can be reproduced by making some approximations that reduce the degree of complexity of the simulation chain, without having a relevant impact on the final result with respect to the one that would be obtained by performing a full simulation. These approximations include the use of parametrizations, breaking down the simulation chain into different independent steps, or the grouping of particles into different categories according to the morphology and distribution of the signal that they may produce in the detector.

5.1.1 Physical processes in ANTARES

The simulation chain is divided in different steps accordingly to the physical processes involved in ANTARES, which can be classified into the following categories:

1. Production of physics signal and atmospheric background:
    - Production of cosmic neutrinos
    - Cosmic ray interactions in the atmosphere, where atmospheric neutrinos and atmospheric muons are produced
    - Neutrino interactions near the detector
2. Production of optical signal in the detector
    - Propagation of atmospheric muons and of the neutrino interactions products through the detector
    - Emission, propagation and detection of Cherenkov light
3. Production of optical background
    - ^{40}K decays
    - Bioluminescence

Among the processes in the first category, the production of a cosmic neutrino flux depends on the theoretical models that describe the neutrino emission from different kinds of sources, and can be treated independently of the detector simulation. In chapter 8 a neutrino flux produced by populations of AGN is inferred from observations in the electromagnetic spectrum, and assuming a neutrino emission model based on the Fermi acceleration mechanism.

As it is mentioned in chapter 1, kaons and pions are present in the air showers induced by the interactions of cosmic rays in the atmosphere. These mesons are unstable and decay producing muons and neutrinos. In particular, charged pions decay through the process $\pi^{\pm} \rightarrow \mu^{\pm} + \nu/\bar{\nu}$ in the 99.99% of the cases, and the charged kaons decay through $K^{\pm} \rightarrow \mu^{\pm} + \nu/\bar{\nu}$

in a 63.4% of the cases. In reference [83] it is shown that for high enough meson energies ($E \sim TeV$), the opening angle between the ν and the μ produced in the decay of a meson can be very small. This makes it probable that both the ν and the μ arrive at the detector at the same time, and opens the possibility of vetoing the downward-going atmospheric neutrino background by discarding those events containing muon tracks originated outside the instrumented volume. This correlation between the arrival times of atmospheric neutrinos and atmospheric muons has been exploited by the IceCube collaboration, who uses the external part of the detector as a veto for atmospheric muons. Nevertheless, the ANTARES limited size does not allow to apply such a veto technique and the simulation of the arrival of atmospheric muons is done independently from the simulation of neutrino interactions.

Atmospheric muons from air showers arrive at the Earth in groups of different multiplicities where the muons tracks are almost parallel and very close to each other. The simulation of the arrival of atmospheric muons is done with the `MUPAGE` code, which generates bundles of atmospheric muons at the detector level. This is done by using parametrizations of the flux, lateral distribution with respect to the bundle axis, and energy spectrum of the muon bundles. These parametrizations, and the `MUPAGE` code are described in section 5.2.1.

The interactions of neutrinos with matter at energies higher than $\sim 10^{-1}$ GeV are dominated by three kinds of processes as it is shown in figure 5.1. For energies lower than ~ 1 GeV, the main contribution to the neutrino cross section comes from processes where neutrinos scatter off an entire nucleon. This can happen via the neutral currents ($\nu + N \rightarrow \nu + N$) in which case the process is called neutral current elastic scattering (NCE), or via charged currents ($\nu_l + n \rightarrow p + l^-$), in which case the process is called charged current quasi elastic scattering (CCQE). When the neutrino energies are high enough, they can excite a nucleon to a resonant state that can decay through different channels producing final states that present different combinations of nucleons and mesons. An example of such resonant processes (RES) is the production of pions from the decay of a Δ resonance, $\nu_\mu + n \rightarrow \Delta^+ + \mu^- \rightarrow n + \pi^+ + \mu^-$. Finally, provided that the neutrino energy is high enough to resolve the internal structure of the nucleons, it can scatter off its individual partons in a process called deep inelastic scattering (DIS). As a consequence of the recoil of the scattered parton, the nucleon is fragmented and a jet of hadrons (or hadronic shower) is produced in the so-called hadronization process. Deep inelastic scattering is the main contribution to the neutrino cross section in the relevant energy range for ANTARES. The simulation of these processes is done by the `GENHEN` code, which is described in section 5.2.2.

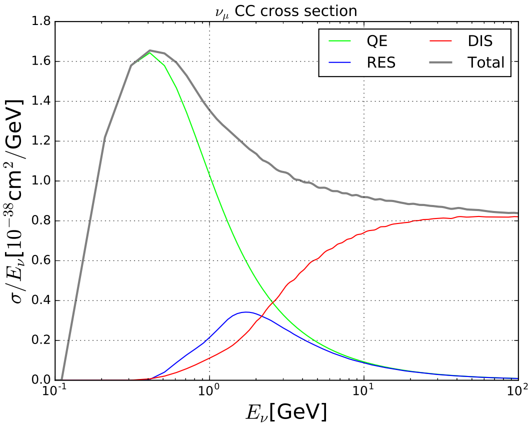

Figure 5.1: Contributions to the neutrino interactions cross section. This figure shows as an example, the contributions to the ν_μ CC cross section at energies higher than the GeV. The main contributions are quasi elastic scattering, resonance production and deep inelastic scattering.

The processes in the second category are addressed by the `KM3` code, which simulates the propagation of the particles produced by `GENHEN` and `MUPAGE`, and simulates the Cherenkov light induced by them. As described in section 5.2.3, `KM3` produces a distribution of Cherenkov photons in the different OMs of the detector by making use of the ANTARES geometry. Finally, the simulation of the optical background is done by the `Trigger Efficiency` code which adds background photons to the output of `KM3`. In addition, `Trigger Efficiency` simulates the detector response to the generated light and produces events that look like the observed ones by simulating the effects of the electronics and applying the different triggers described in the previous chapter.

5.1.2 Event types in ANTARES

To better understand the functioning of the different simulation tools mentioned above, it is necessary to give a description of the different kinds of events that could potentially be reconstructed by a neutrino telescope. Each event is characterised by a different geometrical distribution of the hits produced in the OMs, which depends on how the different particles propagate through the detector.

Concerning the geometry of the ANTARES detector, the products of the neutrino interactions can be classified into charged leptons and hadrons. As mentioned in the previous section, hadrons propagate collectively as a so-called hadronic shower, which is induced by the fragmentation of the nucleons in DIS neutrino interactions. The propagation of the charged leptons through water can be described by straight trajectories until they interact with the medium changing their direction. In this context, the **range** is defined as the average distance travelled by a particle before having either interacted or decayed. Figure 5.2 shows the range as a function of the energy for the propagation of the three charged leptons in rock and in water. These results are obtained from a simulation done with the `Muon Monte Carlo` package described in reference [38], in which each of the particles are propagated through rock and water. The simulation accounts for both radiative and ionization energy losses, as well as for the decay probability of each particle.

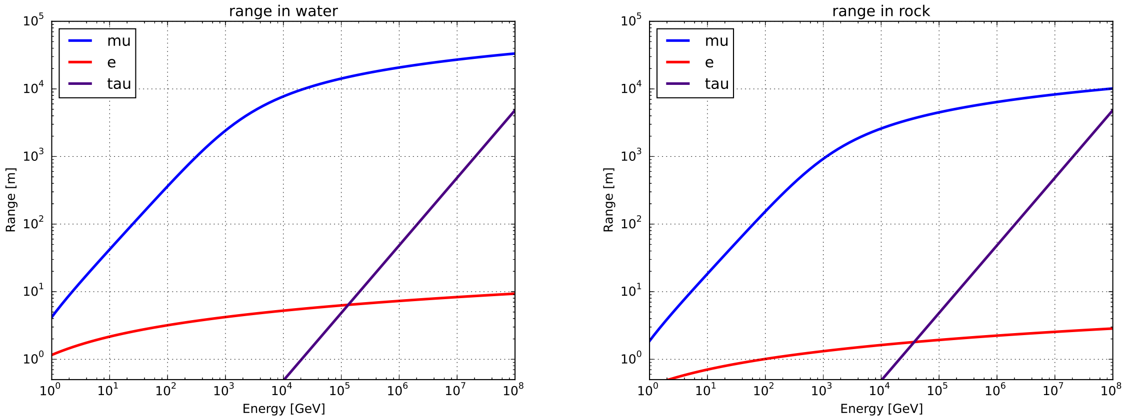

Figure 5.2: Ranges in rock and in water for the three charged leptons.

The comparison between both media shows that electrons and muons have shorter ranges in rock than in water, whereas the range for tau leptons doesn't change from rock to water. This suggests that in this energy range, the propagation of muons and electrons is dominated by their interactions with matter while the propagation of tau leptons, which is independent of the medium, must be mostly influenced by their decay probability. While muons can propagate long enough distances to traverse the detector even if they are produced in the rock under the instrument, the range of electrons is very short compared to the typical distances between the ANTARES OMs and their trajectories cannot be resolved. On the other hand, the trajectories of the tau leptons can be resolved only at energies higher than $\sim 10^5$GeV.

Another quantity that is useful to look at in order to have a better understanding of figure 5.2, is the mean energy loss per unit propagated distance. This quantity is called the **stopping power** of the material, and depends both on the properties of the material and on the energy of the particles. Figure 5.3 shows the stopping power of rock and water for the three charged leptons as obtained from the `Muon Monte Carlo` code mentioned above. An additional line is plotted for the decay processes, which shows the ratio of the particle's energy to the propagated distance in decay processes. This quantity is equal to $m{\cdot}\tau/c$, where m is the lepton's mass, τ its mean lifetime and c, the speed of light in vacuum.

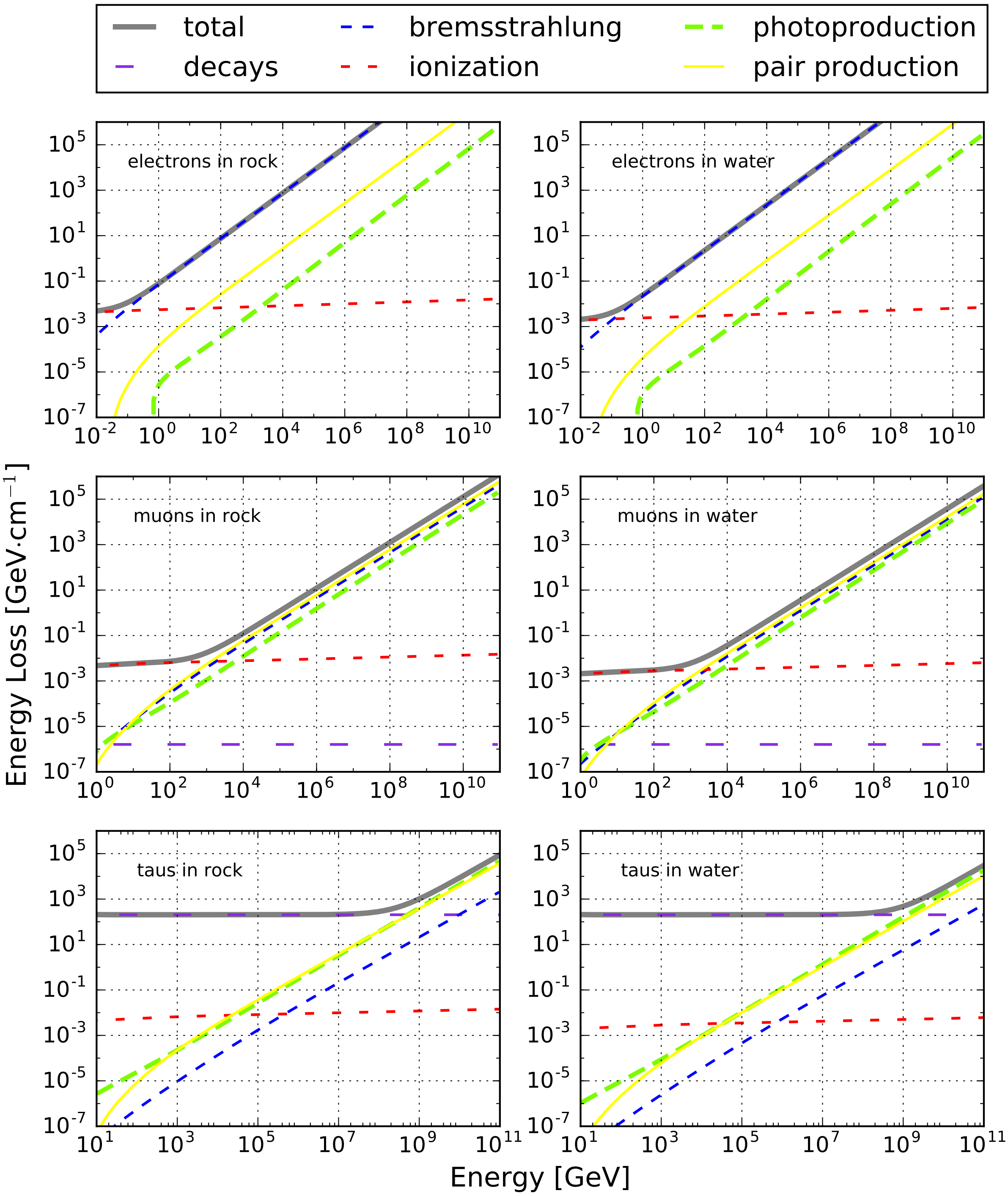

Figure 5.3: Energy loss per distance for the propagation of the charged leptons in rock and in water. These results were obtained with the `Muon Monte Carlo` code, which is described in reference [38].

For electrons, the energy losses in both media and in this energy range are dominated by bremsstrahlung processes, in which electrons are decelerated by the electromagnetic fields of the nuclei. In these processes the energy is conserved through the emission of photons of energies equal to the energies lost by the decelerated electrons. If the energy of an emitted photon is high enough ($> 2m_e$), it will be able to produce e^-e^+ pairs (while inducing a nuclear recoil), that will in turn propagate and undergo subsequent bremsstrahlung processes, leading to a chain of bremsstrahlung-pair production processes that continues until the emitted photon energies are under the pair production threshold. This phenomenon is known as an electromagnetic shower.

For muons, the result of the simulation in rock and water matches with equation 5.3, where α represents the energy losses due to ionization processes, and β represents the energy losses due to radiative processes. At these energies both α and β can be considered approximately constant and independent of the muon's energy. The critical energy $\varepsilon = \alpha/\beta$ at which radiative processes become as relevant as ionization processes, is around ~ 5 TeV in water, and a bit less in rock. The critical energy is also visible in figure 5.2 as a change in the slope of the muon range. For energies higher than ε, the muon range increases at a lower rate because the stopping power of the media increases at a higher rate, and the energy loss per unit distance is higher. In these processes, muons do not get significantly deviated from their trajectories, and therefore leave a track-like signal in the detector.

For **tau leptons**, the situation is quite different: due to their short mean lifetime ($\sim 10^{-13}s$) they decay before undergoing any interaction for energies lower than $\sim 10^9$ GeV. The $\sim 18\%$ of the times tau leptons decay into a muon and two neutrinos, another $\sim 18\%$ of the times they decay into an electron and two neutrinos. The electrons and muons produced in these decays propagate as described in the previous paragraphs. The other $\sim 64\%$ of the times, tau leptons decay into hadronic final states and a tau neutrino.

Summary: signal events in ANTARES

As a consequence of the differences in the propagation of the particles described here above through the detector, the geometrical distribution of the hits produced in the OMs changes depending on the particle that produces them. According to the geometrical distribution of hits, the different particles can be classified into different kinds of events which are summarised in figure 5.4. The most remarkable characteristic of an event is whether it presents a track or not, since the angular error made by the reconstruction algorithms varies significantly from tracks to showers. The events that present tracks are produced by muons and tau leptons. Muons propagate in nearly straight trajectories through the instrumented volume losing energy and producing electromagnetic showers due to bremsstrahlung processes, and tau leptons propagate in straight trajectories (provided that their energy is high enough) until they decay producing either muons or hadronic showers. Events that don't contain a track are those produced by neutral current neutrino interactions, by ν_e charged current interactions, or those ν_τ charged current interactions where a tau lepton is produced with low energy, that will decay into hadrons.

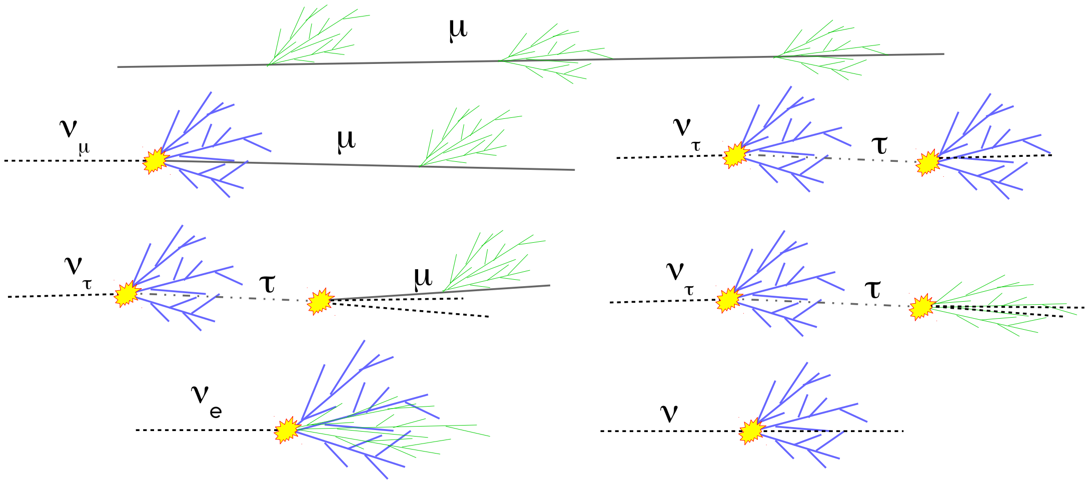

Figure 5.4: Potential event signatures that can be reconstructed with neutrino telescopes. Green lines represent electromagnetic showers, and blue lines represent hadronic showers.

5.2 Simulation tools

The simulation tools in ANTARES comprehend the generation of the processes that produce a detectable signal in the instrument, such as the neutrino interactions, the propagation of particles and the simulation of the optical background. The light detected by ANTARES may be induced by particles having originated far away from the instrument, as is the case for atmospheric muons. From figure 5.2, one can see that the high energy muons produced in the neutrino interactions with rock or water can propagate very long distances before reaching the detector and inducing Cherenkov light likely to be detected by the OMs. In order to correctly characterize the response of the instrument to a neutrino flux arriving at the surface of the Earth, it is necessary to simulate the neutrino interactions in a volume that is large enough to account for the signal produced by long range particles. On the other hand, this volume should be small enough that only those neutrino interactions likely to produce detectable signal are simulated. This problem is addressed by the definition of different regions around the detector which are depicted in figure 5.5. The **instrumented volume** is a cylindrical volume around the optical modules whose dimensions are limited by the height of the lines and by the perimeter defined by the external lines. **The can** is a cylindrical volume that encompasses the instrumented volume and whose dimensions are a few times larger than the water absorption length l_{abs} in the ANTARES site. This volume is defined in order to restrict the simulation of the Cherenkov light which is extremely demanding in computational resources. Cherenkov light is only simulated for those particles that propagate inside the can. Similarly, the **generation volume** is defined as a cylinder inside which the neutrino interactions are simulated. Its dimensions are generally larger than those of the can, and depend on the energy range considered in each particular simulation.

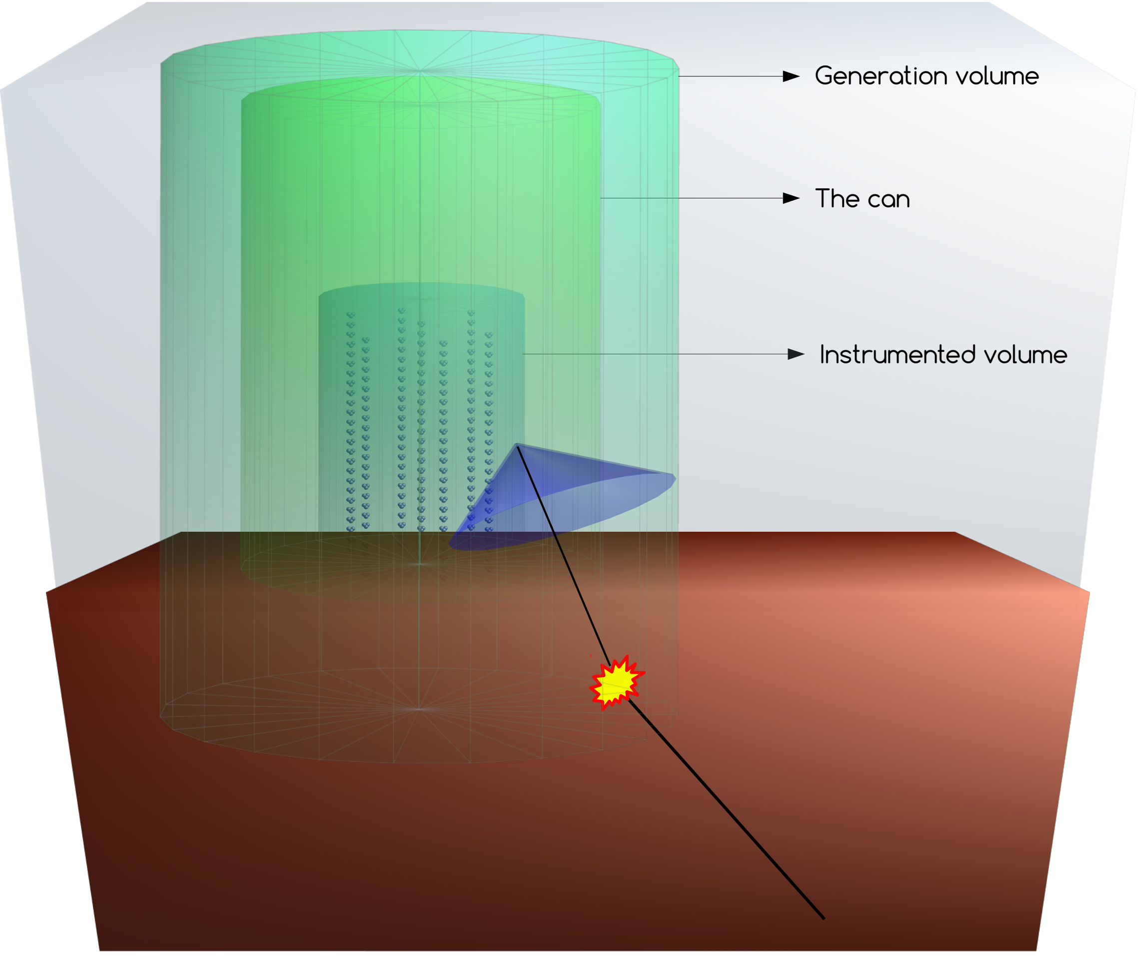

Figure 5.5: Scheme of the volumes defined in the simulation tools. The generation volume is the volume where neutrino interactions are simulated. Since muons produced in neutrino interactions can propagate long distances, the generation volume is larger than the instrumented volume. The can is the volume where the Cherenkov light is simulated. Its dimensions are a few times larger than the absorption length of light in water. the instrumented volume, is the a cylindrical volume containing the OMs.

In the rest of the present section, the different simulation tools used in ANTARES are described which are summarised in the scheme shown in figure 5.6. In first place, the `GENHEN` and `MUPAGE` tools simulate the particles produced in neutrino interactions and the arrival of atmospheric muons to the can respectively. The particles produced by these programs are used by the `KM3` code, which generates the light emitted by each of them during their propagation through the can, and build photon distributions in the OMs. Finally, the `Trigger Efficiency` program simulates optical background hits and environmental conditions, and accounts for the detector response in order to produce a simulated set of events equivalent to the data recorded by the detector in a given period.

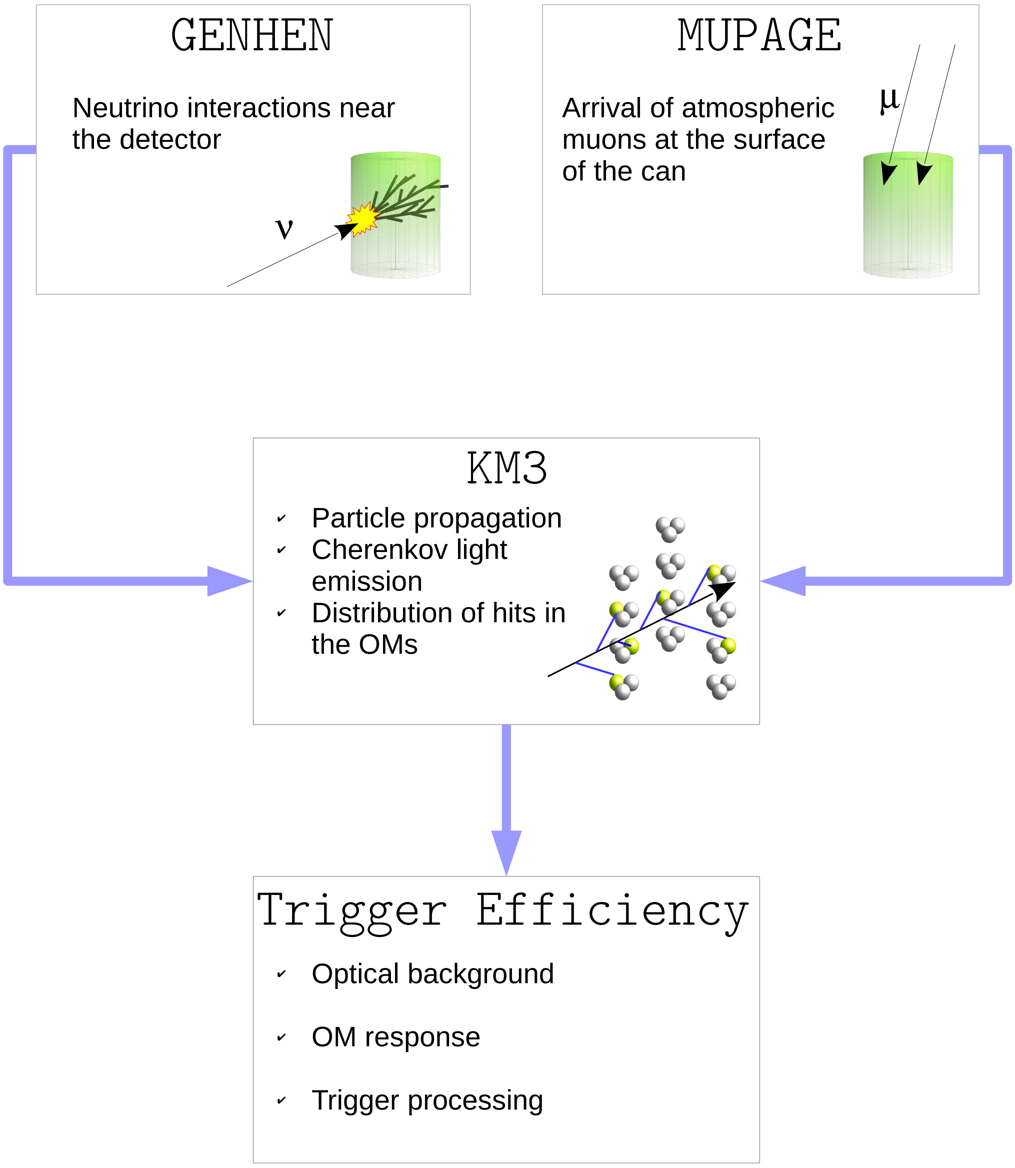

Figure 5.6: Scheme of the different simulation tools in the Monte Carlo chain for ANTARES.

5.2.1 Atmospheric muons: `MUPAGE`

Atmospheric muons are produced at about 15 km above the sea level when cosmic ray interact with the matter in the atmosphere. They are the most abundant charged particles at the sea level, where their average measured energy is $\sim$ 4 GeV [72]. They reach the Earth's surface as single events or in bundles of different multiplicities, and together with neutrinos they are the only remains of atmospheric showers capable of penetrating the Earth deep underground. Their energy spectrum and angular and lateral distributions are the convolution of the production spectrum, the energy loss due to their propagation through the different media and their decays.

The ANTARES collaboration has developed a package with the aim of simulating the arrival of atmospheric muons to the detector. This software is called `MUPAGE` (MUon GEnerator from PArametric formulas), and generates bundles of atmospheric muons at the level of the detector by using a set of parametrizations for their flux, their lateral distribution, and their energy spectrum. These parametrizations were obtained from a complete Monte Carlo simulation of air showers induced by cosmic rays interactions that consisted in 3 steps. First, the `HEMAS` code [81] was used to generate cosmic ray interactions and the subsequent propagation of air showers in the atmosphere down to the sea level. In the second step, the propagation of those muons that had reached the sea level, down to 5 km underwater was simulated using the `MUSIC` code (MUon SImulation Code) [20]. Finally, parametrizations for their flux, lateral distribution and energy spectrum were obtained as functions of the vertical depth h, the zenith angle θ, and the bundle multiplicity m. These parametrizations were obtained by fitting the results of the simulations to formulas that were inspired by the results provided by underground experiments. A detailed description of how these parametrizations were obtained can be found in reference [28]. The next lines provide a summary of these results.

Muon bundles flux The functional form that describes the flux of muon bundles as a function of their multiplicity was obtained from reference [32], where the measurements of underground muons performed by the Fréjus detector at a depth of ~ 1780 m, are shown to be well fitted by the empirical formula,

$$\Phi(m) = \frac{K}{m^{\nu}} \quad \text{with} \quad \nu = \frac{\nu_1}{(1 + \Lambda \cdot m)} \tag{5.1}$$

where K, ν_1 and Λ are free parameters and m the bundle multiplicity. As it is described in [28] the fits of the results obtained with the full Monte Carlo simulation to equation 5.1 show that the parameters K, ν_1 and Λ depend on h and θ. This dependence is shown in figure 5.7 where the flux of muon bundles is plotted as a function of the multiplicity for different depths and zenith angles.

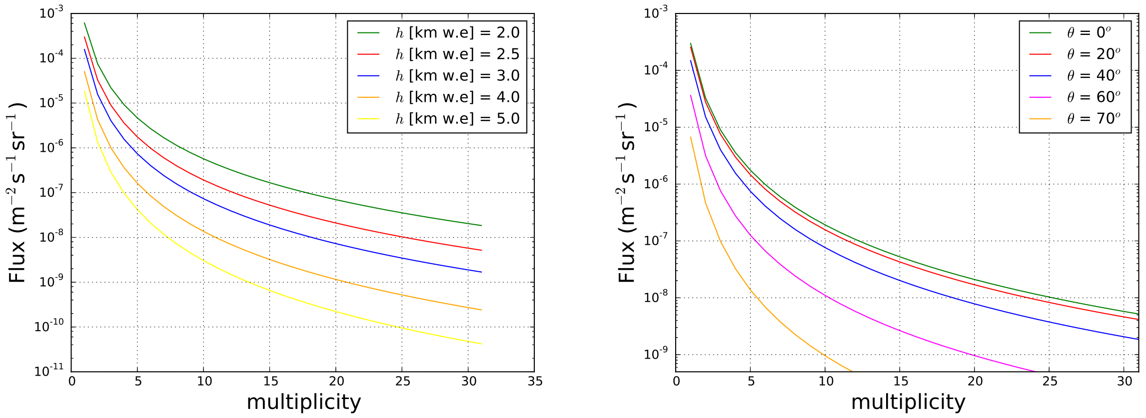

(a) (b)

Figure 5.7: Parametrization of the flux of muon bundles described by equation 5.1. **Left:** Flux of muon bundles with different multiplicities at $\theta = 0^o$ and for five different vertical depths h. **Right:** Flux of muon bundles with different multiplicities m at a vertical depth of $h = 2.5$ w.e. for different zenith angles θ. Muons get absorbed during their propagation through matter, and their flux is therefore reduced with the depth and the zenith angle.

Muon lateral spread In reference [48], a simulation of cosmic ray showers coupled to a subsequent simulation of the propagation of muons through rock shows that the radial distances R from the muons to the shower axis deep underground is well described by an inverse power law. As it is described in [28], the dependence of R with the muon energy makes it necessary to characterize the lateral spread distribution of muons in bundles in order to build a correct parametrization of their energies. Following reference [48], the results of the full Monte Carlo simulation were fitted to the formula

$$\frac{dN}{dR} = C\frac{R}{(R+R_0)^{\alpha}} \tag{5.2}$$

where the factors C ,α and R_0 depend on θ, m and h. Figure 5.8a shows the normalized lateral distribution of muons in doublets ($m = 2$) for the vertical direction ($\theta = 0$) and several values of vertical depth. Figure 5.8b, shows the normalized lateral spread for muons in bundles of $m > 2$ at a vertical depth of $h = 3.5$km.w.e. The average distance R of the muons to the shower axis decreases with the vertical depth and with the bundle multiplicity. The reason for this is that the muons which are closest to the shower axis are the most energetic ones, which in turn can propagate longer distances through matter without getting absorbed. On the other hand, the multiplicity of the bundles increase with the energy of the primary cosmic rays, and therefore the muons in bundles of higher multiplicities are expected to be more energetic.

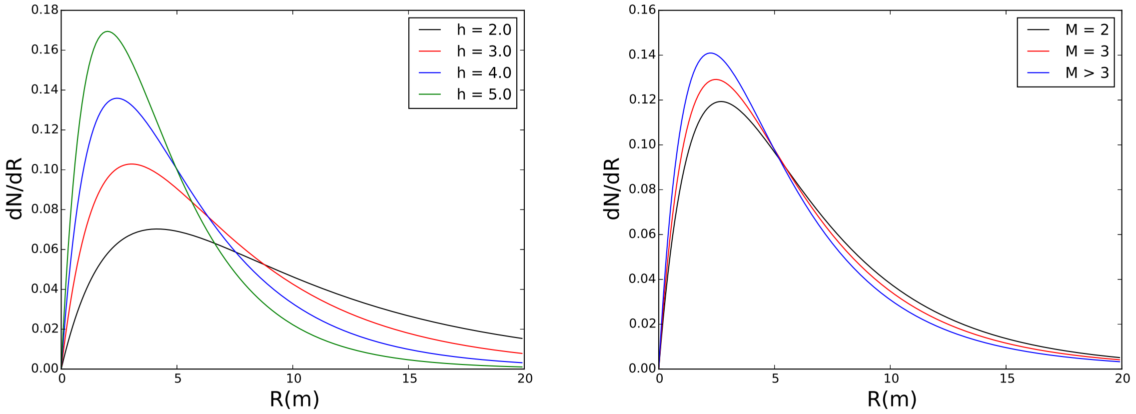

(a) (b)

Figure 5.8: Lateral spread of muons in bundles as a function of the depth and bundle multiplicity

Energy spectrum of muons in bundles The energy spectrum of muons in bundles at a given depth is related to their energy loss during their propagation through matter. At high energies, their average energy loss is described by the equation

$$-\left\langle \frac{dE(E_\mu)}{dX} \right\rangle = \alpha + \beta E_\mu \tag{5.3}$$

where X represents the travelled distance, and α and β represent the muon energy loss due to ionizing and radiative processes respectively. The average distance travelled by muons with initial energy E_0 and final energy E can be computed as

$$X = \int_E^{E_0} \frac{dE_\mu}{\langle dE(E_\mu)/dX \rangle} \tag{5.4}$$

Solving this integral one can find an expression that relates the muon's final energy E to its initial energy E_0 and the average travelled distance X,

$$E = (E_0 + \epsilon) \cdot e^{-\beta X} - \epsilon \tag{5.5}$$

where $\epsilon = \alpha/\beta$. If instead of considering single muons with initial energies E_0, one considers a muon flux following a power-law energy spectrum, $dN/dE_0 = \phi_0 \cdot E_0^{-\gamma}$, equation 5.5 can be used to compute the energy spectrum of the muons after the propagation of a distance X through matter, as follows

$$\frac{dN}{dE} = \frac{dN}{dE_0} \times \frac{dE_0}{dE} = \phi_0 \cdot e^{\beta X(1-\gamma)} \left[E + \epsilon(1 - e^{-\beta X})\right]^{-\gamma} \tag{5.6}$$

This simple way of relating the spectrum of the flux after propagating a certain distance doesn't account for statistical fluctuations in the energy loss processes. Fluctuations become important when the energy loss starts to be dominated by radiative processes, to which statistical fluctuations are inherent since they are highly stochastic. The energy spectrum of muon bundles was parametrized by fitting the results of the full Monte Carlo simulation to equation 5.6, where ϵ, β and γ are considered as simple parameters with no physical meaning, and that depend on the variables h, m, R and θ.

Figure 5.9 shows the differential energy spectrum of single muons as a function of θ and h. The maximum of the distributions E_μ^{max}, shifts towards higher values when h and θ increase, because muons with lower energies are more easily absorbed while propagating through matter. This effect is also seen in figure 5.10 where the differential energy spectrum of muon pairs is shown for different radial distances R to the shower axis.

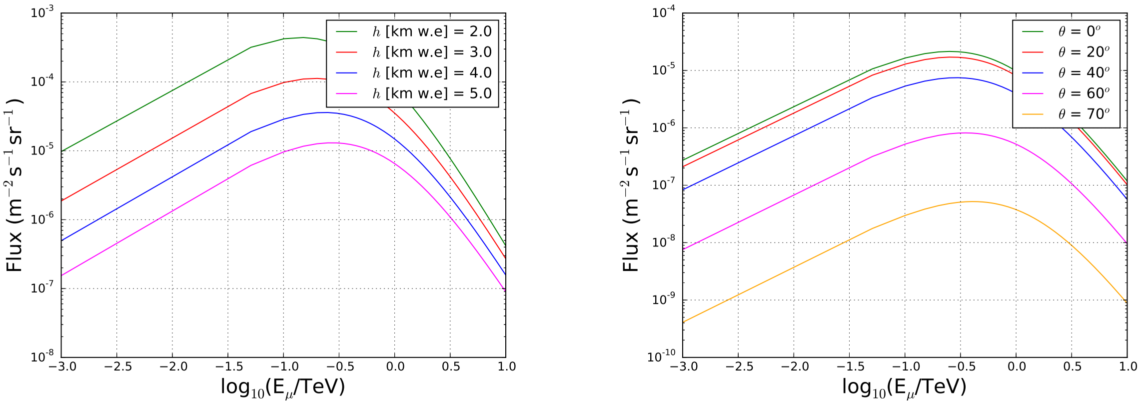

Figure 5.9: Differential energy spectra for single muons. **Left:** at various vertical depths and for the vertical direction. **Right:** at a vertical depth of 4.5 km.w.e and for various zenith angles. The lines have been computed following Eq. 5.6, using 5.1 to obtain a flux. The values of the parameters are the ones corresponding to the fits of the Monte Carlo simulation [28].

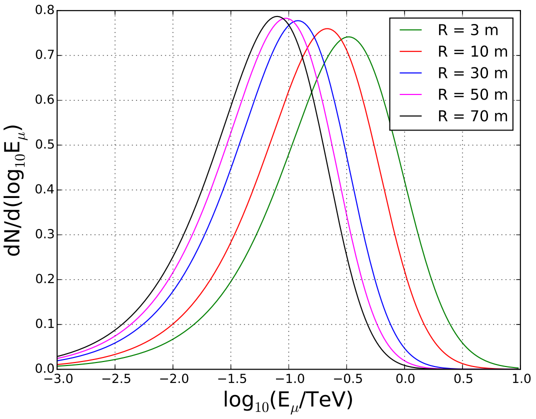

Figure 5.10: Differential energy spectra of muons in bundles with multiplicity $M = 2$, at five radial distances R from the shower axis. The lines were computed with Eq. 5.6 and using the parameters used to fit the full Monte Carlo simulation as given in [28]

The `MUPAGE` code

`MUPAGE` is a Monte Carlo generator of atmospheric muon bundles that uses the parametrizations described above. It simulates the arrival of atmospheric muons at the surface of a generic can which dimensions can be chosen. In what follows, a brief description of the steps followed by the code is given. A fully detailed description of the code is given in [35]. The simulation of a muon bundle consists on the following steps:

1. **Bundle multiplicity and direction** The bundle multiplicity m is sampled from a uniform distribution between some user defined limits $[m_{\text{min}}, m_{\text{max}}]$. Its direction on the detector's local coordinates is defined by the zenith θ, and azimuth ϕ angles. A value of θ is sampled from a uniform distribution in the user defined range $[\theta_{\text{min}}, \theta_{\text{max}}]$, and a value of ϕ is sampled from a uniform distribution in the range $[0, 2\pi]$.

2. **Depth of the bundle intersection with the can** The can is projected onto a plane Π perpendicular to the sampled bundle's direction, as it is shown in figure 5.11. A point $P_{\text{a}} = (X, Y)_{\Pi}$ of coordinates (X, Y) in the plane Π is sampled uniformly from this projection. Using this point, the intersection coordinates $(x, y, z)_{\text{det}}$ of the bundle's axis with the can in the detector's frame, are computed and the intersection depth h is inferred.

3. **Evaluating the bundle probability** As a result of the previous steps, a muon bundle is generated with a multiplicity m, a zenith direction θ and at a depth h. The probability that such a bundle is produced is evaluated from equation 5.1, and the event is consequently accepted or rejected.

4. **Muons impact points** For single muon events (i.e. bundles with $m = 1$), the muon's direction coincides with the bundle axis and its impact point with the can coincides with the point previously sampled. For bundles with $m > 1$, the positions $P_i = (X_i, Y_i)_{\Pi}$ of the muons in the plane Π are sampled so that their radial distances R to the point

P_a are distributed according to equation 5.2. Using these points, the corresponding impact points with the can in the detector's reference frame, $P_i = (x_i, y_i, z_i)_\mathsf{det}$ are computed.

5. **Muons arrival times** The arrival time of each muon is computed relative to the first muon in the bundle, which is assumed to arrive at the can's surface at $t = 0$. If $m > 1$, the distance of each muon to the axis $d_i = P_i - P_a$ is computed and the arrival time of the i^{th} muon is computed relative to the arrival time of the first muon, as

$$t_i = \frac{d_i - d_1}{c} \tag{5.7}$$

6. The energies of the muons are generated following a distribution given by equation 5.6.

Finally, the simulation's livetime is computed. To do so the solid angle is divided in intervals, the j^{th} interval given by $\Delta\Omega_j = 2\pi(\cos\theta_{1j} - \cos\theta_{2j})$ and for each of them, the number of simulated events $N(\Delta\Omega_j)$ with multiplicity $m = m_\mathsf{min}$ and with the bundle axis intercepting the can's upper disk is evaluated. The number of expected events per unit time in the can's upper surface ($h = H_\mathsf{min}$) in the solid angle $\Delta\Omega_j$, with multiplicity m_min is

$$\dot{N}_\mathsf{expected}(\Delta\Omega_j) = \Phi(H_\mathsf{min}, \theta_j, m_\mathsf{min}) \cdot S \cdot \Delta\Omega_j \tag{5.8}$$

where $\theta_j = (\theta_{1j} - \theta_{2j})/2$ and $S = \pi R^2_\mathsf{can} \cdot \cos\theta_j$ is the projected area of the upper disk. The livetime for each bin can be computed as

$$T(\Delta\Omega_j) = N(\Delta\Omega_j)/\dot{N}_\mathsf{expected}(\Delta\Omega_j) \tag{5.9}$$

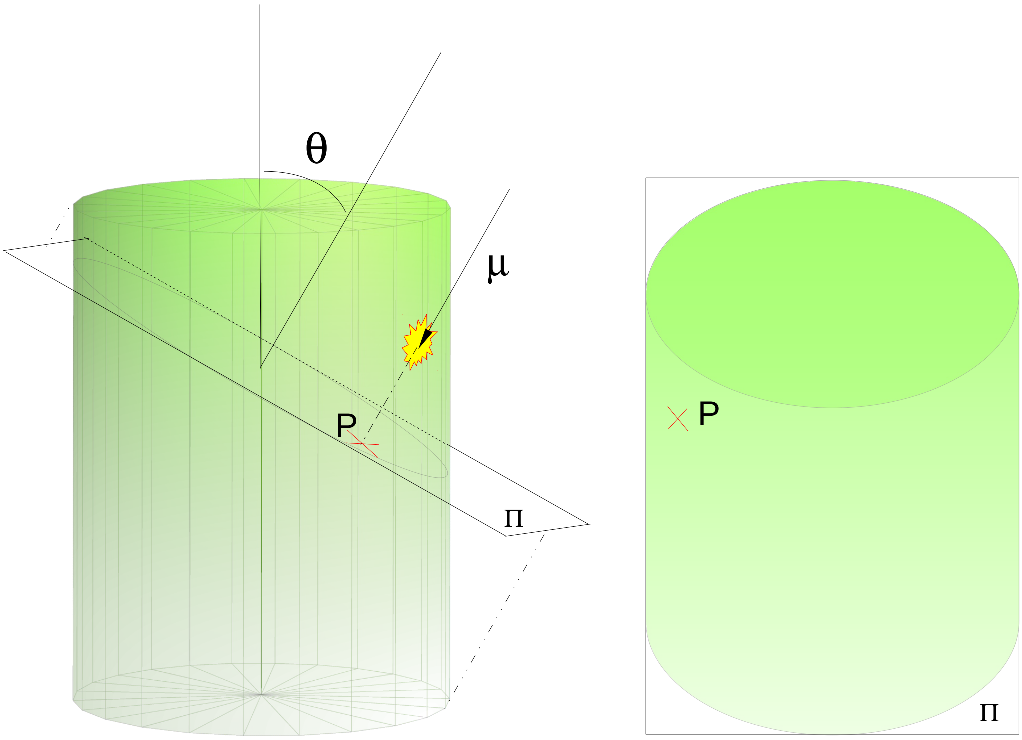

Figure 5.11: Scheme showing the main features of the generation of a muon bundle in `MUPAGE`. A direction θ is sampled, and the impact point of the bundle is sampled from the plane perpendicular to θ.

5.2.2 Neutrinos `GENHEN`

`GENHEN` stands for (`GEN`erator of `High Energy Neutrinos`), and it is the name of the tool used to simulate the interactions of neutrinos likely to produce signal in ANTARES. Since its first versions in which only ν_μ interactions were simulated, `GENHEN` has undergone continuous modifications in order to include the simulation of all flavour neutrino interactions. The modifications in the latest versions of the code have been particularly focused on simulating a ν_τ flux.

`GENHEN` generates distributions of particles inside and on the surface of the can, that are produced in processes derived from neutrino interactions with the matter in the generation volume. The generation is done according to some user specified inputs, the most relevant ones being

- The number of interactions to be simulated, N.
- The energy range of the interacting neutrinos $[E_{\text{min}}, E_{\text{max}}]$.
- The spectral index of the neutrino energy distribution X.
- The range of the neutrino directions in the zenith angle $(\theta_{\text{min}}, \theta_{\text{max}})$.
- The type of event to be simulated. Four possible different events can be simulated
    1. ν_μ CC or NC interactions.
    2. ν_e CC or NC interactions.
    3. ν_τ CC interactions where the produced tau lepton decays to a muon.
    4. ν_τ CC interactions where the produced tau lepton decays to a shower.
    5. ν_τ NC interactions.

The description of the algorithm can be divided into three main stages. In a first step, the generation volume and the number of interactions to simulate per energy interval in the chosen energy range are computed. In second place the interactions are simulated one by one, and finally weights are generated for each each neutrino interaction, that allow to transform the generated sample to a sample corresponding to a cosmic neutrino flux (with chosen spectral index), or to an atmospheric neutrino flux.

Stage 1: Computing the generation volumes and energy range

Charged leptons produced in neutrino interactions outside the can, may under certain circumstances propagate and reach it producing light that is detectable by the OMs. As one can deduce from figure 5.2, whether a charged lepton that is produced at a given distance from the can will reach it or not, depends on its flavour and on its energy. Neutrino interactions are simulated within the generation volume V_{g}, whose characteristic dimension R_{g} is bigger than the radius of the can and depends on the type of event that is simulated. In the energy range $[E_{\mathsf{min}}, E_{\mathsf{max}}]$, R_{g} is chosen to be equal to the maximum distance that a charged lepton produced in a CC interaction of a neutrino of energy E_{max}, would travel in the case in which its energy was the maximum allowed by the kinematics of the interaction. This distance is denoted by $R_{\mathsf{max}}(E_{\mathsf{max}})$. More details about the calculation of $R_{\mathsf{max}}(E_{\mathsf{max}})$ for the different leptons can be found in [63], [24] and [23]. The generation volume for a given energy range, is a cylinder of radius $R_{\mathsf{max}}(E_{\mathsf{max}})$ which extends vertically downwards by $R_{\mathsf{max}}(E_{\mathsf{max}})$, and vertically upwards up to $R_{\mathsf{max}}(E_{\mathsf{max}})$ or up to the sea surface.

Since the range $[E_{\mathsf{min}}, E_{\mathsf{max}}]$ may span several orders of magnitude, a way of saving computing resources is to divide it into intervals of equal length in $\log_{10}(E)$ and to compute a corresponding scaled generation volume V^i_{scaled} for each interval by following the same criterion as for computing V_{g}. The corresponding scaled number of interactions in the i^{th} interval N^i_{scaled}, is sampled from a Poisson distribution,

$$N^i_{\mathsf{scaled}} = P\left(N^i \times \frac{V^i_{\mathsf{scaled}}}{V_{\mathsf{g}}}\right), \tag{5.10}$$

where

$$N^i = N_{\mathsf{total}} \times \frac{\int_{E^i_{\mathsf{min}}}^{E^i_{\mathsf{max}}} E^{-X} dE}{\int_{E_{\mathsf{min}}}^{E_{\mathsf{max}}} E^{-X} dE} \tag{5.11}$$

At the end of this stage, the energy range is divided into intervals, and for each interval a corresponding number of interactions and a scaled generation volume is computed. In the next stage, the interactions are simulated for each energy interval and those particles that can produce detectable light in the can are selected and recorded.

Stage 2: Simulation of the neutrino interactions

Each of the neutrino interactions in each energy interval are simulated in two main steps. First the particles produced in the interaction are generated, and second, a selection of those particles that are likely to produce signal in the detector is done.

The generation of the particles produced in a neutrino interaction in the i^{th} energy interval is done as follows:

1. The energy of the interacting neutrino is sampled from a power law distribution E^{-X}, in the range $[E^i_{\mathsf{min}}, E^i_{\mathsf{max}}]$.
2. The interaction vertex is generated: a point within the scaled volume is randomly chosen and if this point is outside the can, the shortest distance from it to the surface of the can is computed. If this distance is longer than the maximum range (of the corresponding charged lepton) corresponding to the energy of the interacting neutrino sampled in (1), the event is rejected.
3. The neutrino's direction is generated uniformly within the user specified zenith angle range $(\theta_{\mathsf{min}}, \theta_{\mathsf{max}})$. If the interaction vertex is outside the can, the minimum distance between the can and the neutrino direction is computed. If this distance is larger than a user specified distance, the event is rejected.
4. The type of neutrino interaction process is selected after a comparison of the cross sections, and the interaction is simulated by calling the appropriate code. `LEPTO` [58] simulates the DIS processes, and `RSQ` simulates QE and resonant processes.

At this point, the final state of all the particles produced in the interaction process has been computed, and a selection of those particles that can produce light detectable in the can is made according to the following criteria:

1. If the interaction vertex is inside the can, all the particles are recorded.

2. If the neutrino interaction vertex is outside the can only muons and τ leptons are selected. Muons whose directions intersect the can are propagated towards its surface with an appropriate routine that accounts for the energy loss processes. If the muon reaches the can, it is recorded.

For τ leptons, the treatment of the propagation and decay was not correctly implemented and required modifications that are described below in this section.

Stage 3: Weights generation

The particles produced in the previous stages correspond to neutrino interactions which energy spectrum follows a user specified power law, given by the spectral index X. Besides, the user's choice of the input parameters determines the number of simulated interactions in a given solid angle Ω, and in a given volume V. This means that the generated sample doesn't necessarily represent a realistic neutrino flux. If one wants to obtain a sample of particles that represents the arrival to the Earth of a certain neutrino flux, it is necessary to assign weights to each of the events, in order to obtain the correct distribution in energy, time, volume and solid angle.

The neutrino interactions are generated according to a joint probability density function that is defined by the values of the input parameters,

$$f_{E,\Omega,V,t} = \frac{E^{-X}}{I_E} \times \frac{1}{I_\Omega} \times \frac{1}{t_{gen}} \times \frac{1}{V_{gen}} \tag{5.12}$$

where t_{gen} is the (arbitrary) time represented by the simulation, $I_E = \int_{E_{\text{min}}}^{E_{\text{max}}} E^{-X} dE$, and $I_\Omega = \int_{\theta_{\text{min}}}^{\theta_{\text{max}}} d\Omega$. $f_{E,\Omega,V,t}$ is the product of the marginal pdfs obtained by normalizing to 1 the functional forms of the interactions distribution in each dimension of the phase space, and has units of $[GeV^{-1} \cdot s^{-1} \cdot m^{-3} \cdot sr^{-1}]$. Multiplying $f_{E,\Omega,V,t}$ by the number of interactions generated, one obtains the differential rate of interacting neutrinos per unit volume in the phase space,

$$\frac{d\Gamma_\nu}{dEd\Omega dtdV} = N \times \frac{E^{-X}}{I_E} \times \frac{1}{I_\Omega} \times \frac{1}{t_{gen}} \times \frac{1}{V_{gen}} \tag{5.13}$$

The number of neutrino interactions Γ_ν is related to the number of neutrinos arriving near the detector by their probability to interact with the medium, which depends on the differential cross section of the neutrino-nucleon interactions $\sigma(E_\nu)$, and on the number of target nucleons per unit volume $N_A \cdot \rho$, where N_A is the Avogadro number and ρ is the mass density per unit volume[1]. Therefore, the simulated sample corresponds to a differential neutrino flux at the detector $d\phi_\nu^{\text{det}}$ given by,

$$\frac{d\phi_\nu^{\text{det}}}{dEd\Omega dtdS} = \frac{d\Gamma_\nu}{dEd\Omega dtdV} \times \frac{1}{\sigma(E_\nu) \cdot \rho \cdot N_A} \tag{5.14}$$

Since the interaction probability has units of $[m^{-1}]$, equation 5.14 has units of $[GeV^{-1} \cdot s^{-1} \cdot m^{-2} \cdot sr^{-1}]$. This flux is in turn related to the neutrino flux arriving at the Earth $d\phi_\nu^\oplus$ by the probability that neutrinos propagate through the Earth, $P_\oplus(E_\nu, \theta)$. The generated sample corresponds to a neutrino flux at the Earth's surface given by

$$\frac{d\phi_\nu^\oplus}{dEd\Omega dtdS} = \frac{1}{P_\oplus(E_\nu, \theta)} \times \frac{1}{\sigma(E_\nu) \cdot \rho \cdot N_A} \times \frac{N}{E^X I_E I_\Omega V_{\text{gen}} t_{\text{gen}}} \tag{5.15}$$

If one wants to make the sample to correspond to a neutrino flux $d\phi_\nu'^\oplus$ different from the generated one, the events have to be weighted according to the relation between $d\phi_\nu'^\oplus$ and $d\phi_\nu^\oplus$,

$$\omega = \frac{d\phi_\nu'^\oplus}{d\phi_\nu^\oplus} = d\phi_\nu'^\oplus \times \frac{E^X I_E I_\Omega V_{\text{gen}} t_{\text{gen}} \sigma(E_\nu) \cdot \rho \cdot N_A \cdot P_\oplus(E_\nu, \theta)}{N} \tag{5.16}$$

Tau lepton propagation and decay

As mentioned above, the propagation and decay of the tau leptons produced in the ν_τ CC interactions was not correctly implemented in `GENHEN` and modifications have been done in

---

[1] Note that the molar mass is assumed to be equal to 1.

order to properly simulate these processes. The τ lepton is the heaviest of the three charged leptons with a mass of $m_\tau \approx 1.7$ GeV, and the one with the shortest mean live time of $\tau_\tau \approx 2.13 \times 10^{-13}$ s. As a consequence of its short live time, the distance travelled by the tau lepton is negligible for energies below $\sim 10^5$ GeV as it is shown in figure 5.3. On the other hand one can see from figure 5.2 that its propagation both through rock and through water is exempt of energy losses.

In the GENHEN version previous to the modifications here presented, the tau lepton decays were produced in the neutrino interaction point without simulating their propagation, and the decays were simulated by a custom routine which included some of the most relevant decay channels. The main modifications made to the code are two: in first place the taus are propagated, and in second place more decay channels are included.

The propagation of the tau leptons is simulated in the second stage of the simulation, at the time of selecting which of the neutrino interaction products are stored and which are discarded. If a tau lepton is found among the produced particles, its propagation distance is computed according to the formula

$$d_\tau = c \cdot t_\tau \cdot \frac{E_\tau}{m_\tau}, \tag{5.17}$$

where c is the speed of light in vacuum, t_τ is the tau's lifetime in its rest frame, E_τ is its energy and m_τ its mass. The quantities t_τ and E_τ are provided by the LEPTO and RSQ packages that simulate the interactions of neutrinos with matter. Figure 5.12a shows a cross check done to verify that the propagation of the tau leptons is well simulated. The red line in this plot shows the theoretical p.d.f. of the tau lepton life time, and the blue histogram shows the distribution of lifetime values computed from the calculated propagation distance d_τ, E_τ and m_τ. In addition, figure 5.12b shows the $E_\tau - d_\tau$ distribution obtained from GENHEN, compared to the $E_\tau - d_\tau$ dependence obtained by using the tau lepton mean lifetime τ_τ.

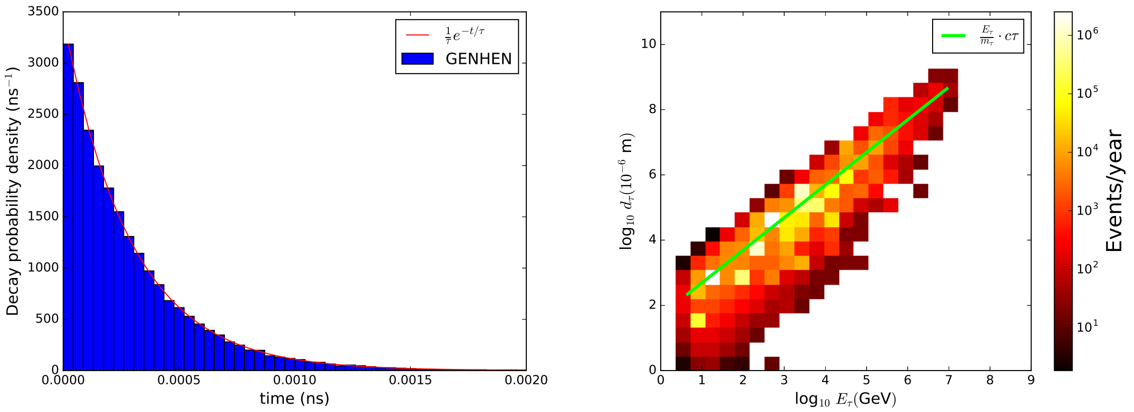

(a) (b)

Figure 5.12: Propagation of the tau lepton. Figure 5.12a shows the theoretical p.d.f of the tau decay time compared to the distribution of decay times obtained from a simulation, by using the tau propagated distance, its mass and its energy. Figure 5.12b shows the distribution of taus in energy and propagated distances obtained from a simulation, compared to the $E_\tau - d_\tau$ relation computed by using the tau lepton mean life time.

Knowing the neutrino interaction vertex and the distance propagated by the tau leptons, their decay vertices can be easily found. Whether their decays are simulated or not, is decided according to the following criteria which are summarised in figure 5.13:

1. If the neutrino interaction vertex is inside the can, the tau decay vertex is computed:
   - If the decay vertex is inside the can 5.13b, then the tau decay is simulated and all the produced particles are recorded.
   - If the decay vertex is outside the can (figure 5.13d), the tau decay is not simulated.
2. If the neutrino interaction vertex is outside the can, the decay vertex is computed:
   - If it is inside the can (figure 5.13f) the τ decay is simulated and all the products are recorded.
   - If the τ decays outside the can into a muon (fig 5.13e), the decay is simulated, and the muon is propagated to the can.

- If the tau decays outside the can through a different channel (fig 5.13c), the decay is not simulated.

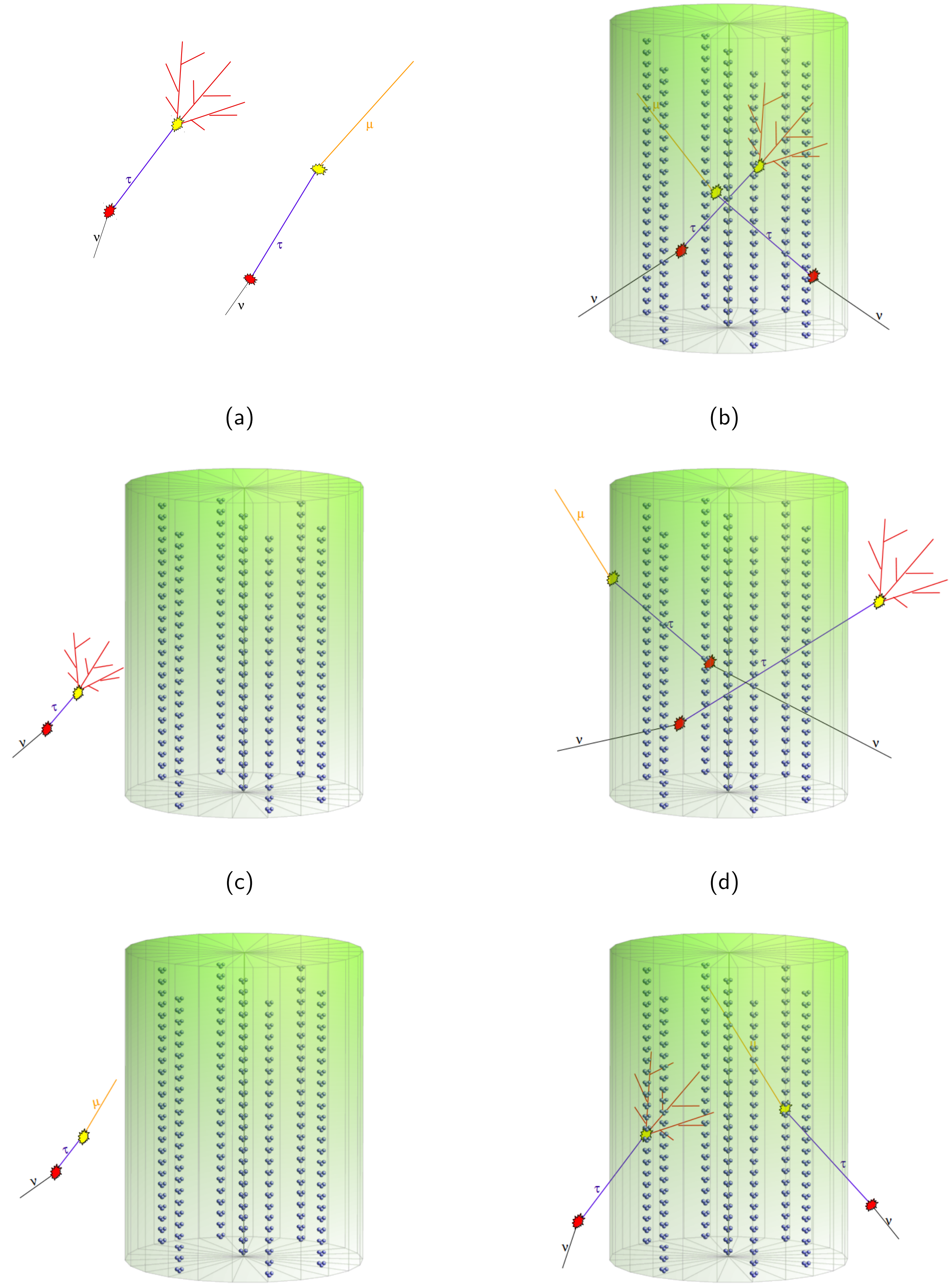

(a) (b)

(c) (d)

(e) (f)

Figure 5.13: The different situations where the tau decays take place with respect to the can.

The tau decays are simulated with the `TAUOLA` package [95], which includes the decay modes listed in table 5.1. Only the first seven channels were included in the `GENHEN` version previous to the modifications here presented, namely `GENHEN` v7r3. The rest of the channels were not treated due to technical problems in their processing. Note that among the channels that were not included there is channel number 8 which has a non negligible branching ratio with respect to the most probable channels. The rest of the channels that were not included have a low probability compared to the first seven. The problems related to the processing of these channels have been solved, and they are included in `GENHEN` v7r4 and posterior versions.

`TAUOLA` id	Channel	Branching ratio respect to 1
1	$\tau \to e\nu_e\nu_\tau$	1.0000
2	$\tau \to \mu\nu_\mu\nu_\tau$	0.9732
3	$\tau \to \pi\nu_\tau$	0.6217
4	$\tau \to \pi\pi\nu_\tau$	1.4221
5	$\tau \to 3\pi\nu_\tau$	1.0180
6	$\tau \to K\nu_\tau$	0.0405
7	$\tau \to K\pi\nu_\tau$	0.0781
8	$\tau \to 3\pi^\pm\pi^0\nu_\tau$	0.2414
9	$\tau \to \pi^\pm 3\pi^0\nu_\tau$	0.0601
10	$\tau \to 3\pi^\pm 2\pi^0\nu_\tau$	0.0281
11	$\tau \to 5\pi^\pm\nu_\tau$	0.0450
12	$\tau \to 5\pi^\pm\pi^0\nu_\tau$	0.0010
13	$\tau \to 3\pi^\pm 3\pi^0\nu_\tau$	0.0062
14	$\tau \to K^+K^-\pi^\pm\nu_\tau$	0.0096
15	$\tau \to K^0\bar{K}^0\pi^\pm\nu_\tau$	0.0169
16	$\tau \to K^\pm K^0\pi^\pm\nu_\tau$	0.0056
17	$\tau \to K^\pm 2\pi^0\nu_\tau$	0.0045
18	$\tau \to K^\pm\pi^+\pi^-\nu_\tau$	0.0219
19	$\tau \to K^0\pi^\pm\pi^0\nu_\tau$	0.0188
20	$\tau \to \eta\pi^\pm\pi^0\nu_\tau$	0.0096
21	$\tau \to \pi^\pm\pi^0\gamma\nu_\tau$	0.0088
22	$\tau \to K^\pm K^0\nu_\tau$	0.0146

Table 5.1: Decay modes included in `TAUOLA`

5.2.3 Tracking of particles and Cherenkov light emission `kM3`

The propagation of photons through the detector depends on the optical properties of the sea water in the ANTARES location. Building a water model that accounts for the interactions of photons with the water molecules and the different kinds of impurities, is important to correctly simulate the arrival of Cherenkov photons to the different OMs in the detector. Figure 5.14, provides a general picture of the interaction processes between photons and water. In this scheme, a monochromatic photon beam $\Phi_i(\lambda)$ illuminates a small volume ΔV of water, of thickness Δr. As a result of the interactions of photons with water, $\Phi_i(\lambda)$ is decomposed into three components. A component $\Phi_a(\lambda)$ of the incident flux gets absorbed within the water volume, and a component $\Phi_s(\lambda, \theta)$ gets scattered into different angles θ with respect to the direction of $\Phi_i(\lambda)$. As a result of these processes, $\Phi_i(\lambda)$ gets attenuated and only a part $\Phi_t(\lambda)$ of it is transmitted through ΔV.

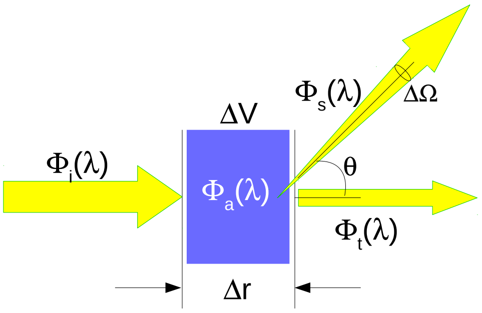

Figure 5.14: Scheme of the processes that describe the attenuation of light in water. A monochromatic beam of light incides over a water volume. Part of it is absorbed, part of it is transmitted, and part of it is scattered into different directions. The optical properties of water define the fraction of the incident flux that is absorbed and scattered.

Since these processes are highly stochastic, the description of the optical properties of water is given by the definition of several physical parameters that are related to the probability that photons are either scattered or absorbed. These parameters are basically three: the scattering and absorption length, defined as the average distance that photons propagate through water before being respectively scattered an absorbed, and the so-called **spectral volume scattering function** $\beta(\theta, \lambda)$, which represents the distribution of the scattering directions. It has units of m^{-1} sr^{-1} and is defined as

$$\tilde{\beta}(\theta, \lambda) \equiv \frac{\beta(\theta, \lambda)}{b(\lambda)} \tag{5.18}$$

The ANTARES water model contains the dependence of both the absorption length and the scattering length with the photon's wavelength in the ANTARES site. These parameters have been estimated by using empirical models for light absorption and scattering in sea water (see reference [75]), to fit experimental measurements performed at the ANTARES site (see [62]). The value of $\tilde{\beta}(\theta, \lambda)$ used in the ANTARES water model relies on measurements presented in references [39], [19], and [61], and can be found in reference [62]. Figures 5.15a and 5.15b summarise the ANTARES water model. Respectively, they show the wavelength dependence of the absorption and scattering lengths as used in the simulations and an example of the distribution of scattering directions for a wavelength of 550 nm.

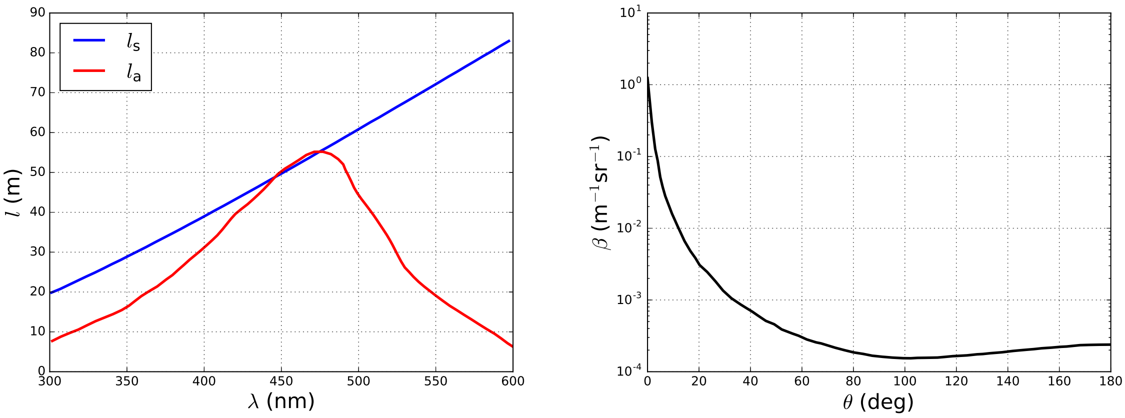

(a) (b)

Figure 5.15: Physical parameters defining the ANTARES water model. Figure 5.15a shows the absorption and scattering lengths, and figure 5.15b shows the distribution of scattering directions.

The `KM3` package simulates the Cherenkov light emission induced by the relativistic particles generated by `GENHEN` and `MUPAGE`. A full simulation of these processes would require to track every particle down to its Cherenkov threshold accounting for its energy losses, and to propagate through the water each of the emitted Cherenkov photons. Unfortunately, due to the large number of particles, the long distances and the wide energy ranges involved in these processes it is not possible to perform simulations with such a level of accuracy. The `KM3` software is a computationally efficient tool designed to simulate the detection of the Cherenkov photons emitted during the propagation of relativistic particles through the detector. The simulation is done in three steps, each of them achieved by a dedicated module.

1. `GEN`: Generates and tracks Cherenkov photons
2. `HIT`: Builds the distribution of hits in the OMs
3. `KM3MC`: Simulates the detector response by using the results from the previous stages.

Generation and tracking of Cherenkov photons `GEN`

The `Gen` code generates photon fields at various radii from a track or a shower. It produces large tables that parametrise the amount of photons arriving to each OM as well as their arrival times, for different OM positions and orientations with respect to the propagating particle's axis. These tables are produced on the basis of detailed simulations where `GEANT` is used to track the individual particles and to develop showers. The generated tables correspond to the following classes of simulation:

- **Muon tracks:** One metre muon tracks are simulated with energy losses below 0.3 GeV, by tracking them in steps of 1 cm. Muon scattering is included.
- **Tau tracks:** One metre tau tracks are simulated without energy loss.
- **Electromagnetic showers:** Electromagnetic showers initiated by electrons at energies of 100 MeV, 1 GeV, 10 GeV and 100 GeV. The shower length l varies with the electron's

momentum p and the medium density ρ as

$$l = \frac{1.8 \cdot (1 + \log_{10} p)}{\rho} \tag{5.19}$$

In order to produce the tables, the volume around the track/shower axis is divided into concentric spherical shells with radii between 2 and 200 m, and the information of about 10000 of the photons crossing each shell is recorded. This information comprises the arrival time, the photon's direction and the interactions suffered, and is obtained by tracking the photon through water as follows:

1. A wavelength λ between 300 and 600 nm is sampled from the Cherenkov spectrum (λ^{-2}).
2. The absorption length l_{a} corresponding to the sampled wavelength is found from figure 5.15a, and an absorption distance d_{a} is sampled from an $e^{-d_{\mathrm{a}}/l_{\mathrm{a}}}$ distribution.
3. The scattering length l_{s} corresponding to the sampled wavelength is computed from 5.15b, and a scattering distance d_{s} is sampled from an $e^{-d_{\mathrm{a}}/l_{\mathrm{a}}}$ distribution.
4. The scattering and absorption distances are compared:
   - If $d_{\mathrm{s}} > d_{\mathrm{a}}$, the photon is propagated a distance d_{a}, and stopped. For each shell crossed by the photon until its absorption, its position, direction, time and wavelength are recorded and labelled as "direct" photon.
   - If $d_{\mathrm{s}} < d_{\mathrm{a}}$ the photon is propagated a distance d_{s}. At each shell its position, direction time and wavelength are recorded and labelled as "direct photon". When the scattering point is reached, a scattering angle θ_{s} is drawn from the distribution shown in 5.15b. The photon's direction is changed by an angle θ_{s}, and a new scattering distance is sampled.

5. For scattered photons, the previous comparison is repeated until the total path length is longer than the absorption distance and the photon information at each shell is labelled as "scattered" photon.

The output of the `GEN` program consists of a list of all the photons recorded in each spherical shell as well as all the relevant information about the simulation, such as the particle type, its energy, the track length medium type, etc.

Building hit probability distributions in the OMs `HIT`

The `HIT` program uses the output from `GEN` to produce distributions of hits and times in the OMs, both for direct and scattered photons. Since the probability that a hit is produced in an OM depends both on its distance and on its relative orientation to the track/shower axis, the hits distribution is computed for each of the spherical shells defined in `GEN`, and for different relative orientations of the optical modules with respect to the direction normal to the shells, defined by the angles (θ_{OM}, ϕ_{OM}) (see figure 5.16). More specifically, the chosen OM orientations are:

- **Direct photons:** 1 bin in ϕ_{OM} and 10 bins of equal size in $\cos(\theta_{OM})$, in the range $-1 < \cos(\theta_{OM}) < 1$
- **Scattered photons:** 3 ϕ_{OM} bins in the range $0 < \phi_{OM} < \pi$ and 5 bins of equal size in θ_{OM} in the range $0 < \theta_{OM} < \pi$

For each OM orientation and distance to the track/shower axis, the hit probabilities are computed as follows:

1. The data in the photon tables are binned in the zenith angle θ_{bin} with respect to the track/shower axis. For the data corresponding to direct photons induced by muon tracks, a single bin is used for all the zenith range. For the rest of the cases, the zenith angle range is binned into 20 bins of equal size in $\cos\theta$.

2. By using the number of entries in each bin, a photon flux is computed and weighted by the OM effective area $A_{\text{eff}}^{\text{OM}}(\lambda, \alpha_i)$, which is a function of the photon's wavelength λ and the incident angle of the photon with respect to the PMT axis, α_i. The OM effective area is the product of the geometric area of the of the photocatode projected in the incident direction $A_{\text{PMT}}(\alpha_i)$, the probabilities that a photon is transmitted both through the OM glass sphere t_{glass} and through the optical gel t_{gel}, and the PMT's quantum efficiency q and collection efficiency c

$$A_{\text{eff}}^{\text{OM}}(\lambda, \alpha_i) = A_{\text{PMT}}(\alpha_i) \cdot q(\lambda) \cdot c \cdot t_{\text{glass}}(\lambda, \alpha_i) \cdot t_{\text{gel}}(\lambda, \alpha_i) \tag{5.20}$$

By repeating this process for the different spherical shells around the track/shower axis, a distribution of detected photons and arrival times for each shell and different OM orientations (θ_{OM}, ϕ_{OM}) is obtained.

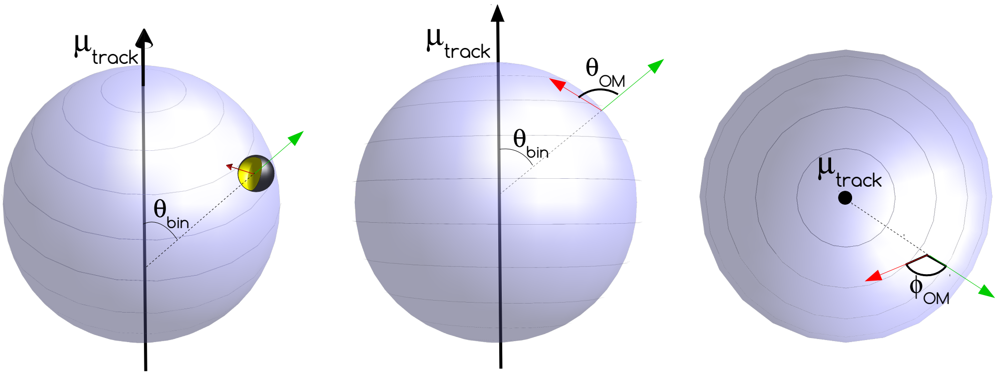

Figure 5.16: Different OM orientations with respect to the spherical shells used in `KM3` to build the photon tables.

Detector response to the passage of relativistic particles `KM3MC`

Finally, the `KM3MC` program reads the lists of particles produced by `GENHEN` or `MUPAGE` and uses the hit distribution probabilities produced by `HIT` together with the information of the detector geometry to simulate the hits produced in the ANTARES OMs, by the particles that propagate through the detector. `KM3MC` simulates the ANTARES response to muon and tau tracks, electromagnetic showers and hadronic showers. Muons are propagated through the medium by iterations through track segments of 1 m long until the muon is stopped or until it leaves the detector. For each segment, the muon energy loss, its initial and final positions, and its direction and time information are computed. The direct and scattered photons detected by each OM are found, and if the energy loss is higher than the average energy loss by ionization (~ 0.3 GeV/m as shown in figure 5.3) an electromagnetic shower is generated in a random position along the 1m segment. To simulate it, a new electron is added to the particle list. For electromagnetic showers, the number of detected photons and their detection times in each OM are sampled from the tables corresponding to the electromagnetic showers, and hadroinc showers are simulated as electromagnetic showers where the energy of the initial electron E_e is a fraction of the energy of the particle initiating the hadroinc shower $E_e = \omega E$. This is known as the one particle approximation.

5.2.4 Optical background, electronics and triggers `Trigger Efficiency`

The output provided by `KM3` does not provide with a realistic description of the data observed by ANTARES, since it doesn't contain information about the hits produced by the optical background. Additionally, `KM3` neither accounts for the effects of the electronics on the hit times. In order to transform the sample produced by `KM3` into a sample of hits that looks like data, the `Trigger Efficiency` program adds background hits to the sample, and applies a correction in order to reproduce the effects of the electronics on the hit recording times. This software applies the logic algorithm that selects the hits that will be used to reconstruct the physics events, according to the triggers explained in section 4.3.

In order to generate the background hits for a given run, the program uses the information about the rate of single hits recorded by the instrument during the run period, and produces background hits with times and amplitudes that follow the observations.

Part III

Search for inhomogeneities in the atmospheric background produced by cosmic neutrinos

Introduction

A common characteristic to almost every particle physics experiment is the recording of a high amount of events, some of which contain relevant information and some of which do not. In accelerator experiments for instance, the events may be proton collisions in which new particles are produced, and where imprints of a particular physical phenomenon under study may be present. Collisions showing these imprints are classified as signal events, and collisions not showing them are classified as background events. In neutrino telescopes, different types of events are produced by the passage of charged particles through the instrumented volume. As it has already been explained, the main event types are produced by the passage of atmospheric muons, the interactions of atmospheric neutrinos, and the interactions of cosmic neutrinos. Events of each of the previous classes can be used to explore different physical phenomena. For instance, atmospheric neutrinos can be used to study neutrino oscillations, atmospheric muons may bring useful information about the cosmic ray interactions in the Earth's atmosphere and cosmic neutrinos are unique astrophysical messengers. In order to study any of the previous phenomena, one would have to interpret the information provided by the events of a certain type. For instance, the study of astrophysical sources with a neutrino telescope requires to analyse and interpret the information contained in the interactions of cosmic neutrinos near the detector. The interactions of atmospheric neutrinos and the propagation of atmospheric muons would constitute in this case background events, while the interactions of cosmic neutrinos would constitute the signal events. In order to obtain accurate results, a correct discrimination between signal and background events is a fundamental issue to deal with. The goal of this part is to present a method to discriminate cosmic neutrino signal in ANTARES from the atmospheric background.

Removing background events is in some cases an easy task that can be achieved by applying cuts in the data. For instance, a significantly large fraction of the atmospheric muon background in ANTARES is removed by applying a directional cut on the directions of the events to select only the upward going ones. The discrimination between atmospheric and cosmic neutrinos becomes nevertheless more difficult, and requires of more sophisticated techniques that usually involve the statistical analysis of simulated event samples containing both, signal and background events. These techniques require in turn to make assumptions about the physical origin of the signal events, and about one or more physical parameters (such as the energy, arrival times, arrival directions...etc) that make them distinguishable from the background events.

Several types of statistical analyses can be applied to an event sample, each of them being sensitive to differences between signal and background in a particular physical parameter. For instance, one could assume that a hypothetical neutrino source was active during a certain period of time in a particular location in the sky, and emitting a neutrino flux with some particular characteristics related to the physics of the source. In order to search for signal events coming from this source, one would first need to simulate event samples containing background events, and different amounts of events located near the position of the source, during the time period in which the source was active, and with energies consistent with the source physical model. Then, one would have to design a statistical analysis able to discriminate between signal and background events, and test its sensitivity to simulated samples containing different amounts of signal events. Finally, once the analysis would have proven to be sensitive to the presence of signal, one would have to apply it to the recorded data. In the unfortunate situation that an analysis of the data does not produce a statistically significant result, rather than saying that no signal was found, one can use the sensitivity of the analysis to set upper limits to the physical parameters used to simulate the signal in the samples.

The following chapters are dedicated to the search of cosmic neutrino signal emitted by populations of Active Galactic Nuclei (AGN). AGN are promising candidates for Ultra High Cosmic Ray (UHECR) sources, where neutrinos may also be produced. They are steady sources, and in this work they will be assumed to be distributed homogeneously in the sky [2]

---

[2] This is an approximation, since the cosmological principle states that the Universe is homogeneous only at large scales and AGN in the local Universe are not supposed to follow an homogeneous distribution.

and emitting neutrinos continuously. Unlike the atmospheric neutrinos whose directions are distributed isotropically, AGN neutrinos are expected to be clustered in space.

This last part is divided into 4 chapters. In chapter 6, the basic concepts related to the statistical methods used to search for signal are described. This is done by using the set of events reconstructed by ANTARES during the period from 2007 to 2012 as a practical example. In particular, two different statistical approaches are described. On the one hand, an approach based on the theory of hypothesis testing, and on the other hand an approach based on the goodness of fit tests. A statistical analysis method developed in the latter framework is described in chapter 7, and its sensitivity to different kinds of sources is tested. Chapters 8 and 9 are dedicated to the search of neutrinos from AGN populations by applying the 2 point correlation method. Chapter 8 describes the simulation of signal events produced in ANTARES by populations of AGN based on two parameters. One related to the number of AGN in the population, and another one related to the power of the AGN in terms of neutrino emission. In chapter 9, the 2 point correlation method is applied to study the sensitivity of ANTARES to such populations.

Chapter 6

Signal search method

6.1 Introduction

As it was explained in the introduction to this final part, the discrimination of signal from background is a matter of primordial importance if one wants to obtain a correct physical interpretation of the experimental data. Normally, each experiment needs its own tools to separate the detected background from the signal corresponding to the physical phenomenon under study. Neutrino telescopes aim for the detection of cosmic neutrinos produced in different astrophysical scenarios, each of which having a particular emission mechanism. The signal produced by cosmic neutrinos in the detector is therefore expected to have different characteristics depending on the type of source from which they are emitted. For instance, neutrinos emitted from GRB are expected to be clustered in space and time, whereas neutrinos from extended potential sources such as the Fermi Bubbles are expected to be detected with a particular spatial and energy distribution. It is therefore necessary to develop tools that allow to discriminate signal from background events, that are adapted to the different astrophysical scenarios in which neutrinos are produced.

The ANTARES collaboration has carried out dedicated searches for transient sources such as GRB, steady point sources, extended sources such as the Fermi Bubbles or the galactic ridge, as well as search for signal neutrinos in coincidence with other cosmic messengers such as gravitational waves or cosmic rays. In this chapter, the basics of the main approaches used in the statistical analyses carried with the ANTARES data are presented. These approaches are basically two, and the use of one or another depends on the kind of signal that one is searching for. When a model for the source of signal is available, an approach based on the theory of hypothesis testing is used. If on the contrary the statistical analysis is designed to perform a model independent search of signal, an approach based on the goodness of fit tests is used. Both approaches are described by using the set of events reconstructed by ANTARES during the period from 2007 to 2012, which is presented in section 6.2, and which is posteriorly analysed in chapter 9.

6.2 The ANTARES data set

The discrimination of signal from background is a complex subject that in some cases can only be achieved by using dedicated techniques which rely on the statistical treatment of data. The search for cosmic signal in the data recorded by neutrino telescopes is one of such cases. To illustrate this, lets consider the set of track-like events reconstructed by ANTARES during the period of time between 2007 and 2012. As it was explained in the introduction to this final part, these events may correspond to atmospheric muons, muons produced by the interactions of atmospheric neutrinos, or muons produced by cosmic neutrinos. Removing the atmospheric muons is relatively easy, since they get absorbed in the Earth. By applying a directional cut on the sample of reconstructed events such that only upward-going events (in the detector's frame) are selected, the atmospheric muon background is reduced significantly but not completely. It is not completely reduced, because some downward-going events can be miss-reconstructed as upward-going and therefore contaminate the selected sample after the directional cut. In order to reduce this contamination, additional cuts must be applied in the parameters that define the quality of the reconstruction, Λ and β. It has been shown in ref. [11] that after the cuts $\Lambda > -5.2$ and $\beta < 1.0$, the estimated atmospheric muon contamination is around 10%. After applying these three cuts on the 2007-2012 sample, a total of 5243 events remain, whose reconstructed directions in the equatorial coordinates right ascension α and declination δ, are shown in figure 6.1. From now on, this data set will be referred to as the **observed sky map**, and denoted by $\mathcal{S}_{\text{obs}}$. From this figure one can see that even if the atmospheric muon contamination had been completely reduced to zero after the cuts, it is impossible to say by naked eye if some of the remaining events correspond to cosmic neutrino signal. Having reached this point, it is necessary to address the problem by using statistical resources.

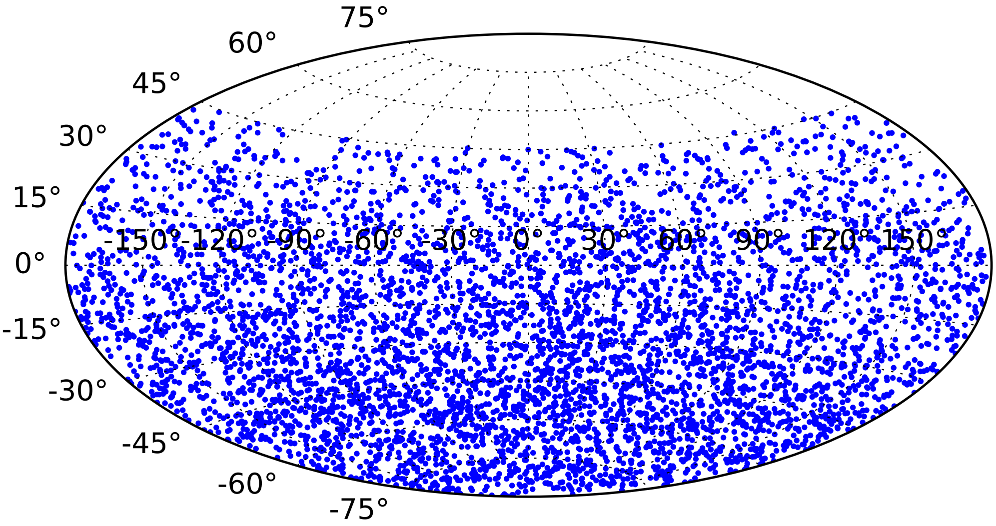

Figure 6.1: Sky map showing the directions of the track-like events reconstructed by ANTARES dugint the period from 2007 to 2012. The plot shows 5243 upward-going events that passed the cuts $\Lambda > -5.2, \beta > 1.0$. In the text, this set of events is referred to as the ANTARES observed sky map, and represented by $\mathcal{S}_{\text{obs}}$
.

The methods used in experimental particle physics to discriminate signal from background are mainly based on two statistical frameworks that were developed during the first decades of the XX$^{\text{th}}$ century. On the one hand, the **goodness of fit test** formalism was developed by R. Fischer [47], and on the other hand Neyman and Pearsons [71], developed the theory of **hypothesis testing**. Both theories deal from a probabilistic perspective, with the problem of determining whether some given experimental observations are compatible with a certain hypothesis. These formalisms are not only used in particle physics, but also in many other fields of research such as economy, medicine or biology. Since nevertheless we are interested in their application to the search of cosmic neutrinos in the ANTARES sky map $\mathcal{S}_{\text{obs}}$, the following sections describe the basic concepts of both theories which are introduced by using this data set as a practical example.

As mentioned in the previous paragraph, both theories study the compatibility of some observations with a given hypothesis called the **null hypothesis**, which hereafter is denoted as H_0. The null hypothesis is usually formulated in such a way that if the data show a certain degree of incompatibility with it, a discovery is claimed. In the case of a search for cosmic neutrinos with ANTARES, these observations are the events in the sky map $\mathcal{S}_{\text{obs}}$, and the null hypothesis can be formulated as

H_0: *"All the events in $\mathcal{S}_{obs}$ are produced by atmospheric background"*.

If any information contained in $\mathcal{S}_{\text{obs}}$ suggests that these observations are incompatible with H_0 and the degree of incompatibility is high, then a discovery of cosmic neutrinos will be claimed. If the degree of incompatibility is not strong enough to claim a discovery, then a level of incompatibility of the data with H_0 will be quoted. The question that arises at this point is: assuming that H_0 is indeed rejected by the observations and that therefore a discovery of cosmic neutrinos is claimed, what is the origin of these neutrinos? This question is addressed by the Neyman and Pearsons theory of hypothesis testing.

6.3 Hypothesis testing

In the theory of hypothesis testing, rather than testing the compatibility of some observations with the null hypothesis, the observations are used to test the null hypothesis against another hypothesis H_1 called the alternative hypothesis. This hypothesis contains information about the discovery which is claimed in the case that the null hypothesis is rejected. In the context of the ANTARES sky map $\mathcal{S}_{\text{obs}}$, three possible examples of alternative hypotheses which are contrary to the null hypothesis H_0 previously formulated, could be

1. H_1: *$\mathcal{S}_{obs}$ contains atmospheric background events, and some events produced by a source located in the coordinates (α, δ) that emits a known neutrino flux.*

2. H_1: *$\mathcal{S}_{obs}$ contains atmospheric background events, and some events produced by a source located in the coordinates (α, δ) that emits a neutrino flux characterized by a power-law of unknown spectral index γ.*

3. H_1: *$\mathcal{S}_{obs}$ doesn't contain just background events.*

In the first example the alternative hypothesis is completely specified, in the sense that there are no free parameters. In such a situation, H_1 is said to be a simple hypothesis. In the second case, the alternative hypothesis involves the spectral index of the source as a free parameter, and it can be regarded as a collection of simple hypotheses where each of them is specified by a different value of γ. In this case, H_1 is called a composite hypothesis. Finally, in the third example H_1 corresponds to a particular case of the second one where the alternative hypothesis is the collection of all the possible hypotheses that are contrary to H_0.

Since no cosmic neutrino sources have been identified yet, formulating a simple alternative hypothesis in which the neutrino flux from a particular source is known is not usually done. The common practice when the alternative hypothesis is linked to a particular neutrino source candidate, is to formulate a composite hypothesis where a parameter such as the neutrino spectral index is let to vary. Two examples of this can be found in the constrains that ANTARES has set to the neutrino emission from a known population of blazars [13], or to the neutrino emission from single point-like sources [11]. In contrast to the cosmic neutrino signal, the atmospheric background is assumed to be well known and H_0 is usually formulated as a simple hypothesis. The third case can be considered as a generalization of the second one, and is the case that is treated later in this work, for which an approach based on the Fischer's theory is better suited.

Since a composite hypothesis is a collection of simple hypotheses, the basic concepts involved in the procedure of testing H_0 against H_1 can be introduced from the simplest case in which both H_0 and H_1 are simple hypotheses. The test of the null hypothesis against the alternative hypothesis is done by following 3 steps:

1. In first place, the so-called **test statistic** λ should be chosen. This is a random variable whose value is given by a chosen function of observable quantities, and whose probability density function (p.d.f.) under the null and the alternative hypotheses $f(\lambda|H)$ can be computed. In the case of the ANTARES sky map $\mathcal{S}_{\text{obs}}$, λ can be any function of any parameter that is measured by the instrument. It could be for instance, a function of the times of the events, of their directions, of their energies...etc. The set of all the possible values of λ is called the sample space, and is represented by Ω.

2. In second place, one should divide Ω into two regions. The acceptance region $\omega*$ is a subset of the sample space containing those values of λ that are likely to be observed when H_0 is true, and the critical region $\omega = \Omega - \omega*$ is the subset of the sample space complementary to the acceptance region.

3. Finally one should compute the experimental value of the test λ_{obs}, and obtain a conclusion about the data. If λ_{obs} is contained in $\omega*$ H_0 is accepted, and if it is contained in ω, H_0 is rejected in favour of H_1.

It is important to note that the result of this procedure depends on the choice of λ and ω, and therefore one risks of making a wrong interpretation of the data. This idea can be better understood by looking at figure 6.2, where the typical concepts involved in hypothesis testing are depicted. It shows an example in which λ follows a normal distribution under two simple hypotheses H_0 and H_1, where the only difference between both distributions is the mean.

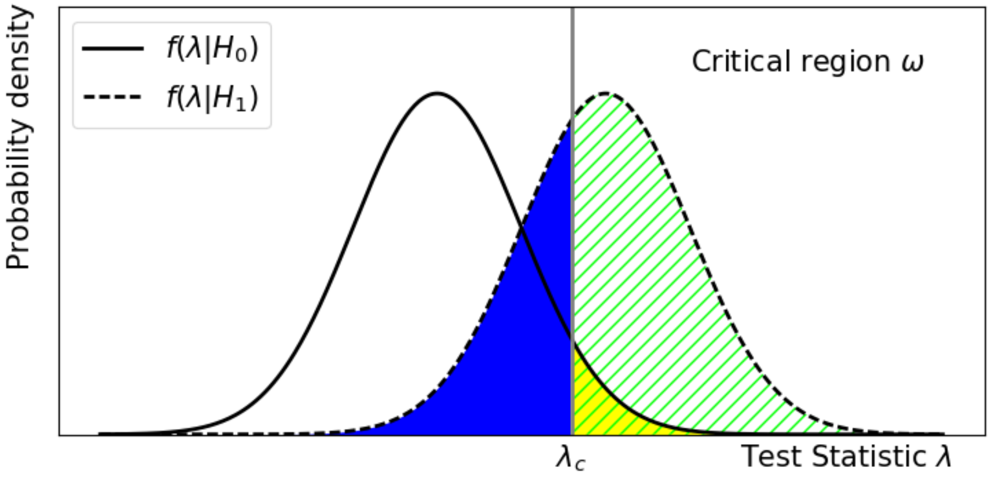

Figure 6.2: Representation of the basic picture in hypothesis testing: the continuous line represents the probability density function of the test λ provided that the null hypothesis is true, and the dashed line represents the probability density function of λ when the alternative hypoithesis is true. The green filled area represents the power of λ to reject H_0 in favour of H_1, and the yellow area represents the size of λ, which represents the probability of rejecting H_0 when it is true.

The sample space Ω is represented by the x-axis, and it is divided into the acceptance and the critical regions by a chosen critical value of the test statistics λ_{c}. Looking at the p.d.f. of λ under the null hypothesis $f(\lambda|H_0)$, one can see that there are some λ values in the critical region with a non negligible probability of being observed when H_0 is true. In the hypothetical case that H_0 were true and λ_{obs} were any of these values, H_0 would be wrongly rejected in favour of H_1 and a false discovery would be claimed. The probability α of making such an error is called the **size** or the **significance** of the test, and is represented by the yellow area under $f(\lambda|H_0)$ in the critical region,

$$\alpha = P(\lambda \in \omega|H_0) \tag{6.1}$$

Alternatively, one can also make the error of accepting H_0 when H_1 is true with a probability β represented by the blue area below the p.d.f. of λ under the alternative hypothesis, $f(\lambda|H_1)$.

An important quantity to bear in mind when two hypotheses are being tested is the probability of accepting H_1 when it is true. This probability is given by $1 - \beta$, and it is called the **power** of the test λ for correctly rejecting H_0 in favour of H_1 or **discovery potential** of the test λ.

$$\text{power} = 1 - \beta = P(\lambda \in \omega | H_1) \tag{6.2}$$

In fig 6.2, the power is represented by the green dashed area under $f(\lambda|H_1)$.

The values of the size and the power depend on the choice of the test statistic and of the critical region. Ideally one would like to choose λ and ω such that the probability of making any of the two mentioned errors would be as minimum as possible (or said with other words, that minimise the size of the test, and that maximise its power). But this is not such a straightforward question since it usually happens that β increases when α decreases, and vice versa. Figure 6.2 is a clear example, where decreasing the size of the test α also decreases its power. Reducing the size and increasing the power can be therefore regarded as two conflicting objectives that make it (almost) impossible to accept or reject the null hypothesis with absolute certainty, since there will (almost) always exist a probability of miss-interpreting the observations. In particle physics it is common to fix the significance at a certain value, and then look for the test that has the maximum power to correctly claim a discovery of H_1. The values at which the significance is usually fixed are $\alpha_{3\sigma} = 1{-}2.7{\cdot}10^{-3}$ and $\alpha_{5\sigma} = 1{-}5.7{\cdot}10^{-7}$, which are also called 3σ and 5σ levels of significance[1]. The corresponding critical values of the test, to these levels of significance are respectively denoted by $\lambda_{3\sigma}$ and $\lambda_{5\sigma}$.

At a given level of significance, the most powerful test for rejecting H_0 in favour of H_1 when both of them are simple hypotheses is given by the likelihood ratio test. For the

---

[1] These values correspond to the result of integrating a normal distribution from three and five standard deviations respectively towards its most extreme values and are commonly used as a reference, even if the test statistic pdf is not a normal distribution.

ANTARES observed sky map, this test is given by,

$$\lambda = \frac{\mathcal{L}(\mathcal{S}_{\text{obs}}|H_1)}{\mathcal{L}(\mathcal{S}_{\text{obs}}|H_0)} \tag{6.3}$$

which is the ratio between the likelihood (or probability) that the set $\mathcal{S}_{\text{obs}}$ would be observed when H_0 is true, and the likelihood observing the same set when H_1 is true. If the hypotheses H_0 and H_1 depended on some parameters p and q respectively, they could be written as collection of simple hypotheses, each of them characterized by a possible value of p and q, $H_0(p) = \{H_0(p_i)\}$ and $H_1(q) = \{H_1(q_j)\}$. In that case, the most powerful test would be given by the maximum likelihood ratio,

$$\lambda = \frac{\text{max}_j(\mathcal{L}(\mathcal{S}_{\text{obs}}|H_1(q_j)))}{\text{max}_i(\mathcal{L}(\mathcal{S}_{\text{obs}}|H_0(p_i)))} \tag{6.4}$$

in other words, it is the likelihood ratio computed by choosing the values of the parameters p and q that maximise the likelihood of the observations under H_0 and H_1 respectively. This test statistic is suitable for an alternative hypothesis like the one in the second of the previous examples, in which part of the events in $\mathcal{S}_{\text{obs}}$ are assumed to be produced by cosmic neutrinos emitted from a point source with an unknown spectral index γ. If the null hypothesis is simple (i.e. the atmospheric background is known), then the test statistic that would optimise the discovery potential for this kind of source, would be given by finding the value of γ that maximizes $\mathcal{L}(\mathcal{S}_{\text{obs}}|H_1(\gamma))$.

Applying equation 6.4 is reasonable when the number of parameters in either hypotheses is small. The alternative hypothesis in the third of the previous examples (i.e. "there is something else than just background") is so general that in may involve an arbitrarily high number of parameters. Indeed, from the point of view of the hypothesis tests, formulating such a general alternative hypothesis is like not making an alternative hypothesis at all. In such a case, $\mathcal{L}(\mathcal{S}_{\text{obs}}$ is an undefined quantity and applying equations 6.3 or 6.4 is no longer possible. When an alternative hypothesis is not defined, the compatibility of the data with

H_0 is done in the framework of goodness of fit tests.

6.4 Goodness of fit tests

The approach for testing the compatibility of observations with a null hypothesis when an alternative hypothesis is not formulated, is done in a similar way as in the theory of hypothesis testing. Still, a test statistic λ should be chosen, and still H_0 is rejected if λ_{obs} falls in a critical region defined by a significance level α. The main difference with respect to the hypothesis test is that since in this case an alternative hypothesis H_1 is not formulated, it is not possible to optimise the test for the discovery of a particular signal.

In this framework, the experimental value of the test λ_{obs} is compared with its p.d.f. under H_0, and the consistency of the observations with H_0 is inferred with a certain confidence level (CL). The confidence level which is also called p-value, is a quantity that represents how well do the observations fit the null hypothesis and is computed as the probability, assuming that H_0 is true, of observing a value of λ as extreme as the experimental one. The meaning of "extreme" in this situation means to be "as far away from the mean value of $f(\lambda|H_0)$ as the observations are". This concept is represented in figure 6.3, where $f(\lambda|H_0)$ is shown together with the significance α, which is represented as the blue area under $f(\lambda|H_0)$.

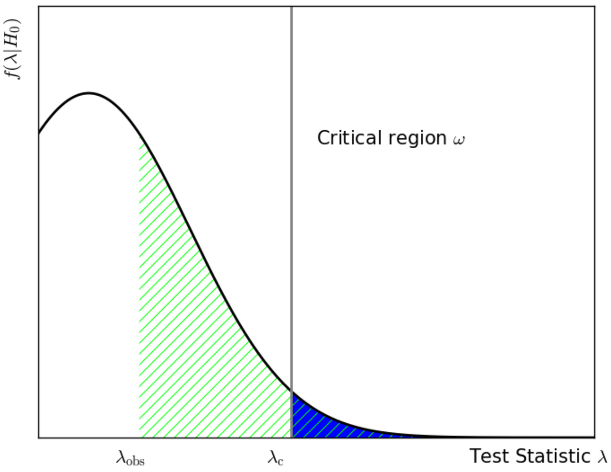

Figure 6.3: Schematic representation of the basic concepts appearing in the goodness of fit tests. The black curve represents the pdf of the test statistics λ under the null hypothesis, the blue area represents the chosen level of significance α, and the green area represents the p-value, which is obtained from the observations. If the p-value is smaller than the significance, then an incompatibility of the observations with H_0 at an α level of significance is claimed.

In this example it is assumed that a departure from the null hypothesis would yield higher values of λ than the ones that are likely to be observed under H_0 (i.e. the left tail of the distribution is not considered). Therefore, the values of λ considered to be more extreme than the observed one in this example, are those values of λ higher than λ_{obs}, and the p-value is represented as the area dashed in green under $f(\lambda|H_0)$. As in the case of hypothesis testing, the significance values that are typically used in particle physics are 3σ and 5σ. If the p-value is larger than the 3σ significance, then the observations are believed to be consistent with the null hypothesis. In the case that it is smaller than the 3σ significance, it is believed that the data are somehow incompatible with the null hypothesis, but not enough to claim a discovery. If the p-value is smaller than the 5σ, the data are believed to be incompatible with the null hypothesis.

6.4.1 Discovery power and goodness of fit tests

Even though the spirit of the goodness of fit tests is not to reject H_0 in favour of a particular alternative hypothesis, one can still compute the discovery power of the chosen test statistic for any alternative hypothesis H_1 as it is described in 6.4. This is what it is done in the following chapters.

The next chapter presents a method based on the goodness of fit test to search for an excess of anisotropies with respect to the background only hypothesis, in the directions of the events in sky maps like $\mathcal{S}_{\text{obs}}$.

Chapter 7

The 2 point correlation analysis

In this chapter, the 2 point correlation method is presented as a particular case of the goodness of fit tests. This method is used to search for an excess of anisotropies on the arrival directions of the events at different angular scales. This approach is complementary to the point-source search based on the maximum likelihood method mentioned in section 6.3, which is mainly sensitive to one bright point-like source and not to collective effects.

This chapter is divided into three sections. The motivation to use this analysis with the ANTARES data set is given in section 7.1 and the general steps to follow and its main ingredients are presented in 7.2. In section 7.4, a deeper analysis of the 2 point correlation method is done, and several configurations under which it can be performed are described. Each of these configurations is defined by the choice of some of the parameters that define the analysis, and which can have an impact on its result. Finally, one of these configurations is chosen to apply this method to the search of cosmic neutrinos in the ANTARES observed sky map $\mathcal{S}_{\text{obs}}$. The choice is made by comparing the discovery power of the method under its different configurations, for several kinds of sources.

7.1 Motivation: The spatial distribution of atmospheric and cosmic events in ANTARES

In section 6.2, $\mathcal{S}_{\text{obs}}$ has been defined as the set of the 5243 upward-going track-like events reconstructed by ANTARES in the time period from 2007 to 2012, which pass some cuts related to the quality of the track reconstruction (namely $\Lambda > -5.2$ and $\beta < 1.0$). This set is mainly composed by events produced in the interactions of atmospheric neutrinos close to the detector and a small fraction (estimated to be less than the 10% from Monte Carlo simulations) of downward-going atmospheric muons whose tracks have been wrongly miss-reconstructed as upward-going. This set may contain as well some events produced by cosmic neutrinos. If they are present, their spatial distribution is expected to be different from that of atmospheric neutrinos. The motivation for applying the 2 point correlation analysis to $\mathcal{S}_{\text{obs}}$, is to detect an excess of anisotropies in $\mathcal{S}_{\text{obs}}$ with respect to the atmospheric background, that could be potentially produced by cosmic neutrinos at different scales.

Even though the arrival directions of cosmic-rays to the Earth follow an isotropic distribution, the spatial distribution of the events in $\mathcal{S}_{\text{obs}}$ (shown in figure 6.1) doesn't appear to be isotropic for two reasons. First, because the data set contains just events with upward-going directions in the detector's local coordinates. This directional selection affects the effective visibility of the instrument, which is related to the fraction of the sky from which events are selected. At any given time, this fraction of the sky is obviously 2π sr if only upward-going events are selected, and it corresponds to a certain region of the Universe. But due to the rotation of the Earth, different regions of the Universe become visible from the ANTARES location along one day. Some of them are be visible during a larger amount of time than others, and some regions are not visible at all. Note that if ANTARES was located at one of the Earth's poles (which are crossed by the Earth's rotation axis), only half of the Universe would be visible with upward-going events. In second place, the data taking conditions also affect the spatial distribution of the reconstructed events. The environmental conditions could produce an asymmetry on the times of the day at which the events are reconstructed with a given quality, and the malfunctioning of some OMs due to their ageing also introduces an asymmetry on the local directions of the reconstructed events. These asymmetries on the times and local directions of the reconstructed events produce anisotropies on the absolute arrival directions of the events in $\mathcal{S}_{\mathsf{obs}}$. The ANTARES visibility of the Universe with upward-going events and the distribution in the equatorial coordinates followed by the events in $\mathcal{S}_{\mathsf{obs}}$ are shown in figure 7.1. The latter shows the effects of the non uniformity in the times and local coordinates of the reconstructed events. It has been produced from $\sim 10^4$ "scrambled" versions of $\mathcal{S}_{\mathsf{obs}}$. Scrambling $\mathcal{S}_{\mathsf{obs}}$ consists on generating a new sky map $\mathcal{S}_{\mathsf{scr}}$ with exactly the same number of events as $\mathcal{S}_{\mathsf{obs}}$. For each event in $\mathcal{S}_{\mathsf{scr}}$, its absolute coordinates are built by choosing randomly the local coordinates of an event in $\mathcal{S}_{\mathsf{obs}}$, and by choosing randomly the arrival time of another event in $\mathcal{S}_{\mathsf{obs}}$. This process allows to build a new sky map where the distribution of the events in absolute coordinates accounts for the time and directional asymmetries introduced during the data taking.

On the other hand, the distribution of the arrival directions of cosmic neutrinos is characterised by two features that make it possible to distinguish them from the atmospheric background. In first place, the arrival directions of cosmic neutrinos are expected to be clustered around the locations of their sources increasing the number of anisotropies in the spatial distribution of the recorded sample with respect to the atmospheric level, assuming that more than one neutrino is detected from the same source. In second place, cosmic neutrinos are expected to present a harder energy spectrum than the atmospheric background. Since the probability of interaction during their propagation through the Earth increases with their energy, the reconstructed directions of cosmic neutrinos are expected to follow a different distribution from that of the atmospheric ones. This is illustrated in figure 7.2, where the relative acceptance for a cosmic neutrino flux characterized by an E^{-2} energy spectrum is compared to that of an atmospheric flux and to the events in $\mathcal{S}_{\mathsf{obs}}$.

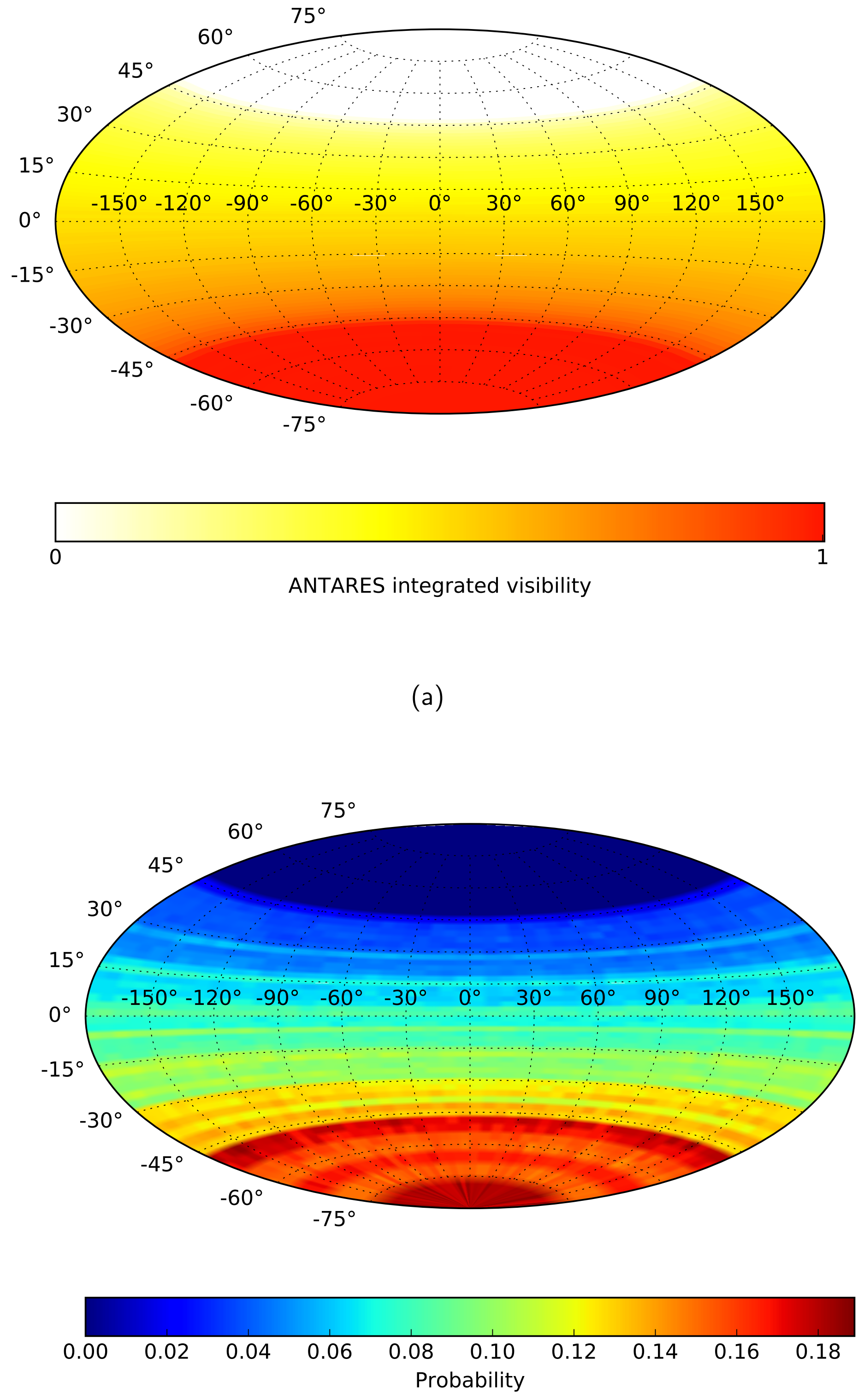

(a)

(b)

Figure 7.1: (a) ANTARES integrated visibility. (b) Distribution followed by $\mathcal{S}_{\text{obs}}$.

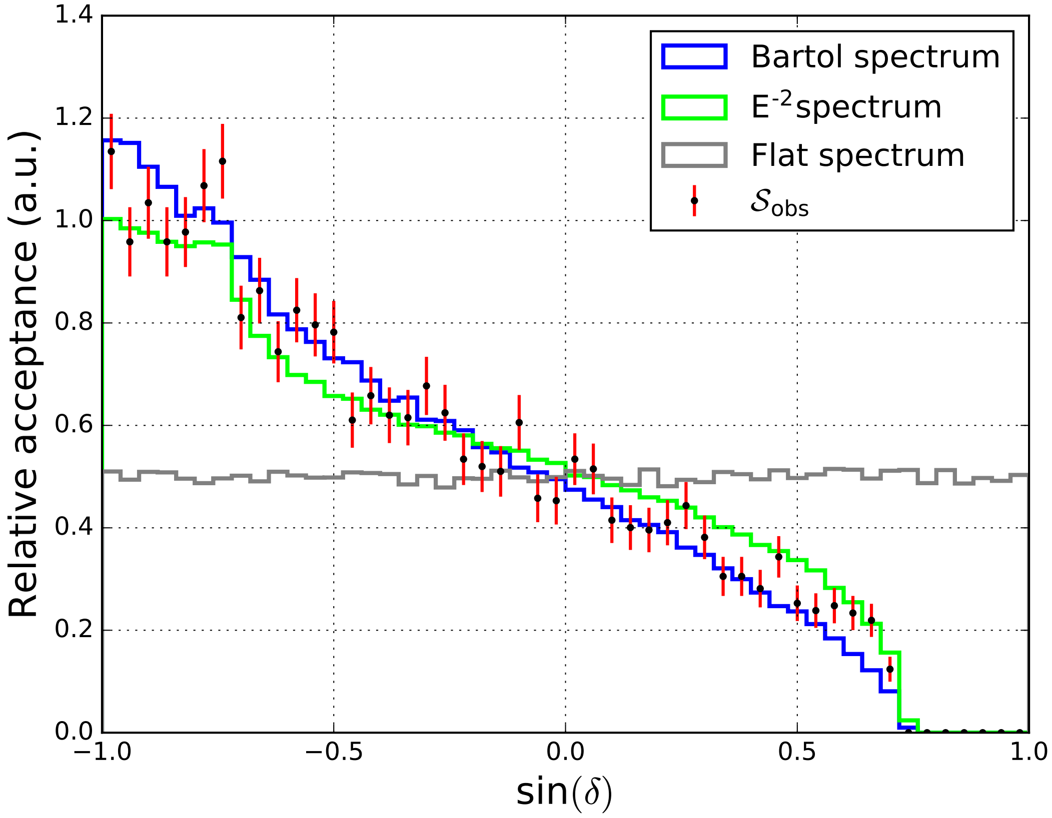

Figure 7.2: Relative acceptance as a function of the declination. The blue and green curves correspond to an atmospheric and a cosmic neutrino fluxes respectively, and have been computed from Monte Carlo simulations. The black dots show the normalized acceptance of 5243 the events in $\mathcal{S}_{\mathrm{obs}}$.

In a sky map dominated by atmospheric background, the excess of anisotropies introduced by a cosmic neutrino flux could be small enough not to affect the global spatial distribution of the whole set of events, making it impossible to identify them. In other words, the distribution shown in figure 7.1b is compatible with sky maps that contain weak anisotropies produced by signal events at different angular scales, and with purely atmospheric samples.

The 2 point correlation method provides with a test statistic that allows to identify an excess of anisotropies at different angular scales.

7.2 The 2 point correlation analysis

The 2 point correlation analysis is used to search for an excess of anisotropies in $\mathcal{S}_{\text{obs}}$ with respect to the expected level of anisotropies present in sky maps that contain only background events. This search is done at different angular scales by the use of the 2 point correlation distribution, which is the distribution computed by counting the number of pairs of events N_{p} in $\mathcal{S}_{\text{obs}}$ as a function of their mutual angular distances $\Delta\Omega$. The main steps of the method are the following:

1. Building the 2 point correlation distribution under the null hypothesis, characteristic from sky maps where only background events are present.
2. Choosing a test statistic λ that is related to an excess of anisotropies with respect to the background. This quantity is computed from the 2 point correlation distribution.
3. Finding the distribution of λ under the background only hypothesis, $f(\lambda|H_0)$ and the critical values $\lambda_{3\sigma}$ and $\lambda_{5\sigma}$.
4. Finding the value of the test λ_{obs} corresponding to the observations by comparing the 2 point distribution of $\mathcal{S}_{\text{obs}}$ to the background one computed in the 1st step. A comparison of λ_{obs} to the critical values $\lambda_{3\sigma}$ and $\lambda_{5\sigma}$ allows to know whether an excess of anisotropies with respect to the background is present in $\mathcal{S}_{\text{obs}}$ or not.

The rest of this section deals with the first three steps, while the results of the analysis for the events in $\mathcal{S}_{\text{obs}}$ are presented in chapter 9

7.2.1 The 2 point correlation distribution

Figure 7.3 shows the 2 point correlation distribution for the events in $\mathcal{S}_{\text{obs}}$, together with the 2 point correlation distribution that represents the background-only sky maps, which is used as a reference with which to compare the data. The reference distribution is built by averaging the 2 point correlation distributions of $\sim 10^5$ background-like sky maps. Each of these maps contains 5243 events (the same number of events as $\mathcal{S}_{\text{obs}}$), whose coordinates are randomly sampled from the distribution in figure 7.1b. As already mentioned, this distribution contains the information about the systematic asymmetries introduced by the status of the detector and the environmental conditions during the data taking. Therefore, sampling the events from this distribution ensures that their spatial distribution follows that of the atmospheric background that is present in $\mathcal{S}_{\text{obs}}$. At the same time, a possible excess of anisotropies present in the observations is removed due to the randomization process. The reference distribution is shown in figure 7.3 together with the 2 point distribution of the observed events $\mathcal{S}_{\text{obs}}$.

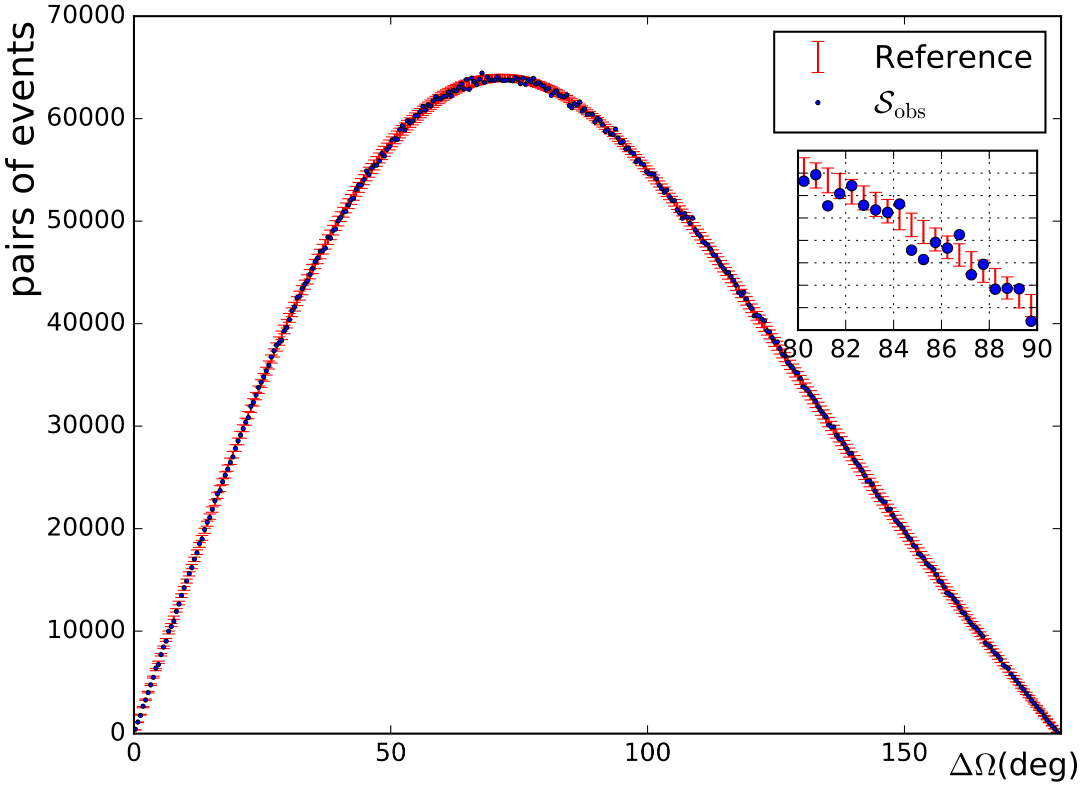

Figure 7.3: The 2 point correlation distribution. The blue points represents the distribution of the data in $\mathcal{S}_{\rm obs}$, and the red bars represent the reference distribution. The size of the bars represents the standard deviation with respect to the mean at each bin, and are centred in the mean values.

The data are represented by the blue points in figure 7.3, and the reference curve is represented by the red bars which are centred on the mean value of the distribution at each bin. The size of these bars represents the standard deviation with respect to the mean at each angular scale, of the $\sim 10^5$ simulated sky maps.

7.2.2 The test statistic λ

The test statistic should represent the differences between the 2 point correlation distribution of $\mathcal{S}_{\text{obs}}$ and the reference 2 point correlation distribution. The comparison between these distributions shown in figure 7.3 is done bin by bin, by computing the quantity

$$\alpha_i = \frac{|N_p^{\text{obs}}(\Omega_i) - N_p^{\text{bg}}(\Omega_i)|}{\sigma(\Omega_i)} \tag{7.1}$$

where $N_p^{\text{obs}}(\Omega_i)$ and $N_p^{\text{bg}}(\Omega_i)$ are the numbers of pairs of events found at the angular scale Ω_i in the data and reference distributions respectively, and σ_i is the standard deviation of the background with respect to the mean at that angular scale. Therefore, the quantity α_i represents the difference with respect to the background of the numbers of pairs of events at each angular scale. Since these differences are expected to grow with an increase of the level of anisotropies, the test statistic is chosen to be the maximum of these differences,

$$\lambda = \max\{\alpha_i\} \tag{7.2}$$

7.2.3 background λ distribution

Once the test statistic has been chosen, it is necessary to find its p.d.f. under the background hypothesis. This is done by comparing the 2 point distribution of each of the simulated background sky maps with the reference distribution and computing the value of λ for each of them. Figure 7.4 shows $f(\lambda|H_0)$ obtained from 10^4 background-like maps. Since a huge number of simulations would be necessary to reproduce the tail of this distribution, an extrapolation of an exponential fit has been done. This extrapolation is showed as a blue dashed line, and the fit as a red continuous line. The critical values of λ can be easily found by computing the cumulative version of this distribution, which is shown in the left.

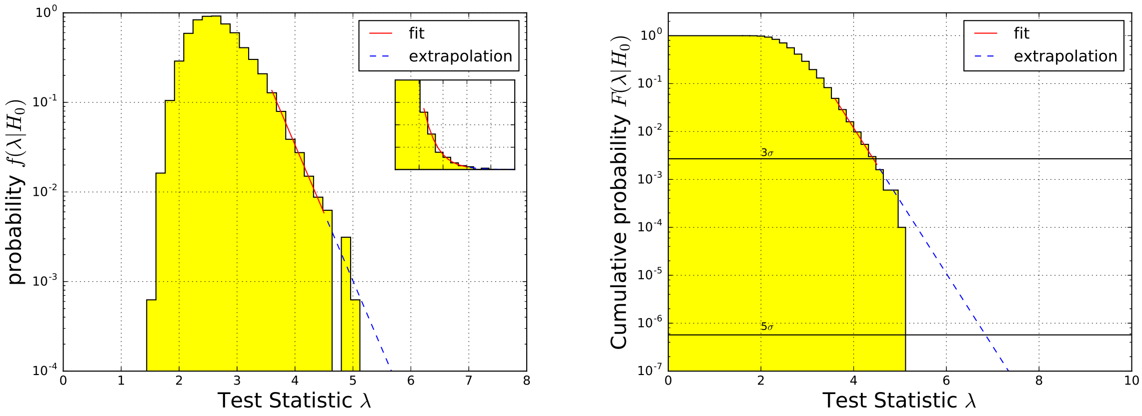

(a) (b)

Figure 7.4: Probability density function of the test statistic, inferred from equation 7.2. The values of λ are obtained by comparing the 2 point correlation distribution of $\sim 10^4$ background-like sky maps with the reference distribution. Figure 7.4a represents the probability density function. Due to a lack of statistics, it was not possible to reproduce the tail of the distribution and it was extrapolated from an exponential fit. The red line shows the fit, and the blue line the extrapolation. Figure 7.4b shows its integral which can be used to identify the critical values of the test $\lambda_{3\sigma}$ and $\lambda_{5\sigma}$.

7.3 Setting up the framework for the 2 point correlation analysis

The most special feature about the 2 point correlation distribution is that each bin contains information of the full sky at a different angular scale. This makes the method suited for a model independent search of anisotropies produced by sources of undefined sizes and morphologies, and this is the reason why this analysis is developed in the statistical framework of goodness of fit tests, where the test statistic λ is not optimised for the detection of signal from a particular source. Nevertheless, given how the method has been presented in section 7.2, there are some technical aspects which can have a general impact on the performance of the analysis, and which are worth exploring. This section is dedicated to study three aspects of the analysis: The binning of the 2 point correlation distribution, its representation, and an additional cut on the events in $\mathcal{S}_{\text{obs}}$, which selects only the most energetic events in the sample.

After giving a description of how these features can influence the result of the analysis, its discovery potential for the detection of different kinds of sources is computed under different configurations defined by the binning, representation and energy cut.

7.3.1 Tunning the 2 point correlation distribution

Binning

The bins in the 2 point correlation distribution shown in 7.3 have an equal size in angular distance $\Delta\Omega$, which corresponds to 0.5 degrees.

The bin size has been chosen to be of the order of the median angular resolution of ANTARES for track-like events. This quantity has been introduced in section 3.3.1, and its value for track like events is shown in figure 3.6. It is computed from Monte Carlo simulations as the median of the distribution of the angular distances between the true directions of the generated particles and the reconstructed ones. Its value for track-like events after applying the cuts on Λ and β that define $\mathcal{S}_{\text{obs}}$, has a value of ~ 0.38 (see ref. [11]).

If this analysis was to be applied for the search of a specific type of source, an optimal bin size could be chosen by looking for the value large enough such that all the pairs of signal events produced by the source would fall into the same bin, and small enough such that the number of pairs of background events in that bin would be the minimum possible. Since nevertheless, the analysis is meant to be model independent, no other considerations have been made about the bin width, than choosing it of the order of the resolution of the instrument.

An interesting aspect to consider about the binning is whether it is more convenient to bin the 2 point correlation distribution with bins that span the same solid angle instead of bins that span the same angular distance. Figure 7.3 may result counter intuitive if is not interpreted correctly. At first sight, it may seem that the most probable angular distance between pairs of events which are uniformly distributed in a sphere is $\sim 70^{\circ}$, but this is not true. The peak around 90° in figure 7.3 appears naturally as a solid angle effect, because the solid angle corresponding to each bin in angular distance Ω_i, which varies with the angular distance according to $2\pi(\cos\Omega_{i-1} - \cos\Omega_i)$, has its maximum value at 90°. If the choice of the binning is done such that every bin subtends the same solid angle, the shape of the 2 point distribution should change towards a flatter shape where all the bins contain roughly the same number of pairs. Since the test statistic is built from a comparison of all the bins in the 2 point distribution, one could expect this comparison to be fairer if all the bins contain the same statistics (at least, in order of magnitude).

From the point of view of the binning, two different configurations of the 2 point distribution are considered. One in which the bins have equal size in angular distance, of 0.5°, and another in which the bins have equal size in $\cos\Delta\Omega$, where the bin corresponding to the smallest angular scale subtends an angular distance of $\sim 0.5^{\circ}$.

Representation

By representation of the 2 point distribution, one means whether the differential or the cumulative distribution of pairs of events is used. One could reasonably guess that the best choice is to use the cumulative representation of the 2 point distribution, based on a naive argument. Depending on the morphology of the neutrino sources, the pairs of signal events may fall into different bins of the differential 2 point distribution, producing a small excess with respect to the background at each bin. If on the contrary a cumulative representation of the 2 point distribution is used, the excesses produced at each angular scale would be integrated, leading to the largest possible excess at the highest angular scale spanned by the source. In addition, another advantage of using a cumulative representation of the 2 point distribution has been pointed in reference [10]: by cumulating the numbers of pairs at the different angular scales, the statistical fluctuations of the background with respect to the mean would be reduced at the highest angular scales, since under-fluctuations and over-fluctuations at different angular scales would be compensated. Therefore, the test statistic would be more sensitive to the addition of one pair of events at high angular scales under the cumulative representation than under the differential representation of the 2 point distribution.

From the point of view of the representation, the choice of the cumulative and differential distributions of pairs of events are tested.

Figure 7.5 shows the reference 2 point correlation distributions corresponding to the 4 configurations described in this section, which correspond to the combination of using a cumulative and differential representation with a bins of equal size in angular distance and in solid angle. The green points represent the mean at each angular scale, and the red band represents the standard deviation with respect to the mean $\sigma(\Omega)$, at each angular scale. The width of the band at each angular scale and for each configuration is represented in figure 7.6.

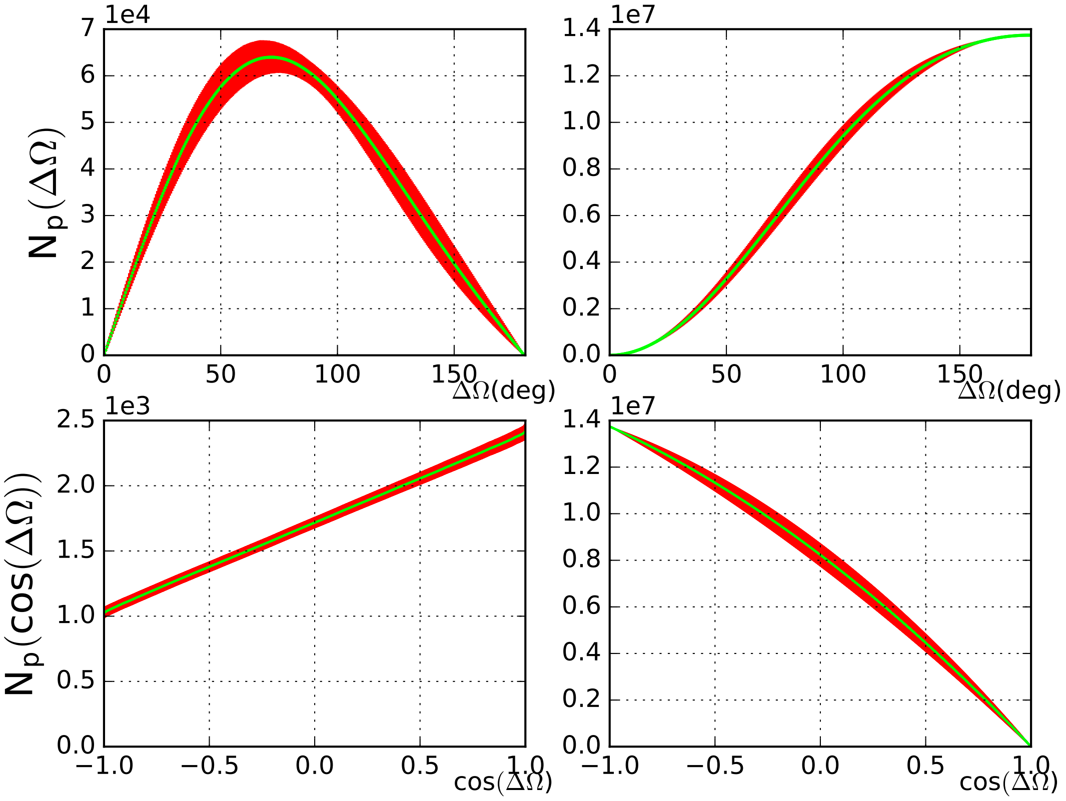

Figure 7.5: The reference 2 point correlation distributions under the 4 configurations considered here. The green dots represent the mean values at each scale, and the width of the red band represents the standard deviation with respect to the mean at each angular scale.

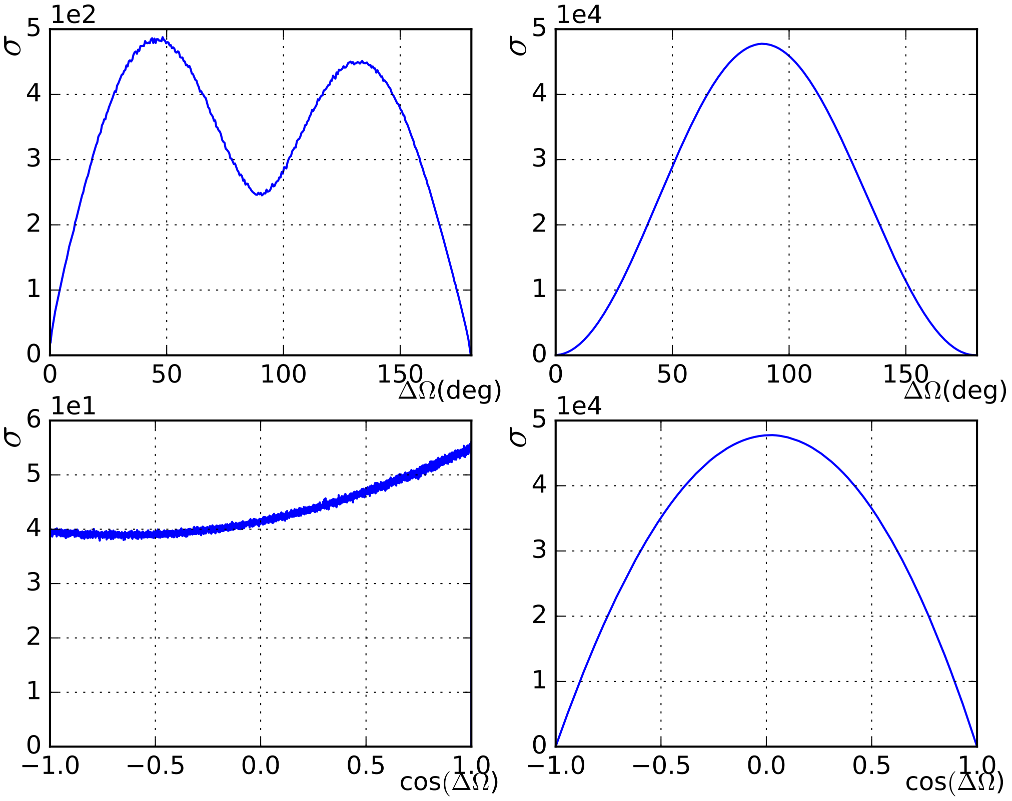

Figure 7.6: Values of the standard deviation with respect to the mean of the 2 point correlation distribution at each angular scale for each of the 4 configurations considered in this study.

7.3.2 Using the energy of the events

Finally, a selection of the most energetic events in $\mathcal{S}_{\text{obs}}$ is considered. Since cosmic neutrinos are expected to be distributed according to a harder energy spectrum than the atmospheric ones, the use of the information on the energy of the events is an attractive input for the analysis that may increase its sensitivity to the presence of cosmic neutrinos. The information about the energy used in this work, is encoded in the N_{hit} energy estimator, which is defined as the number of optical modules used in the reconstruction of the event. Since the amount of Cherenkov light emitted by a charge particle depends on its energy, and a minimum amount of photoelectrons is required in an OM to trigger a hit, N_{hit} can be used as a proxy of the energy of the events. Figure 7.7 shows the normalized N_{hit} distributions for cosmic neutrinos distributed according to an E^{-2} energy spectrum and atmospheric neutrinos, as obtained from Monte Carlo simulations. The normalized N_{hit} distribution of the events in $\mathcal{S}_{\text{obs}}$ is also shown.

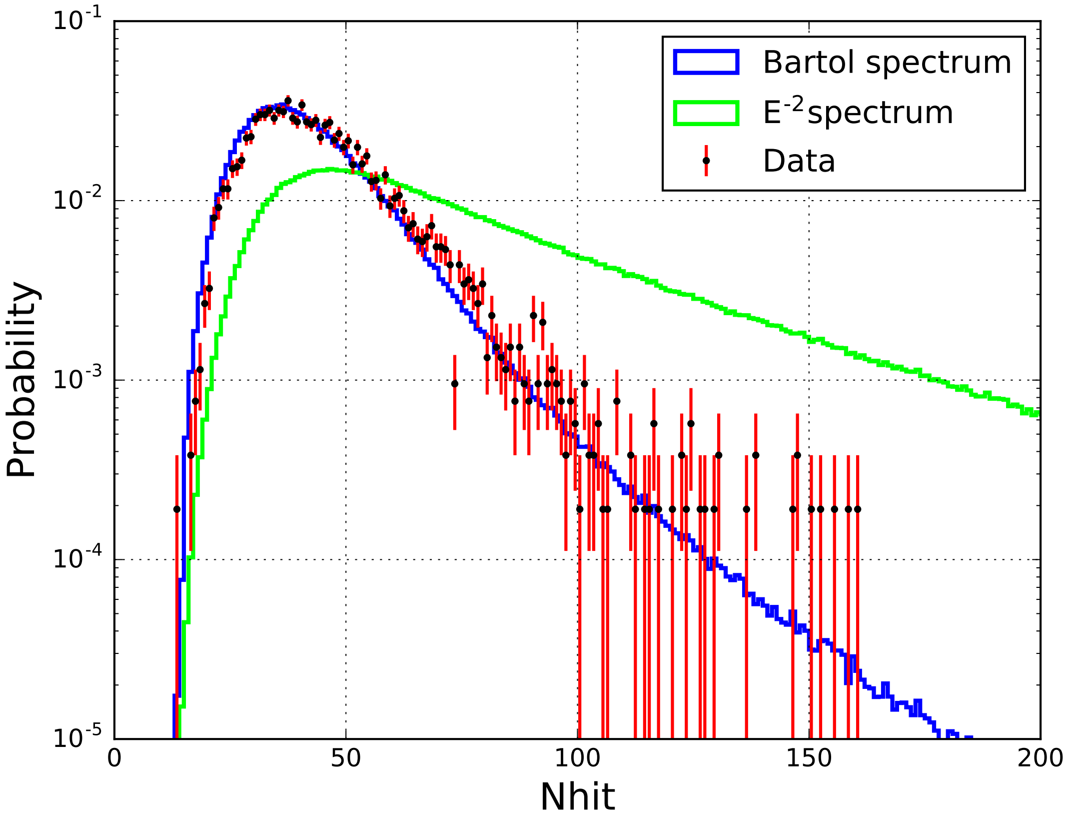

Figure 7.7: Normalised distributions of the number of hits. The blue and green curves correspond to an atmospheric and a cosmic neutrino fluxes respectively, and have been computed from Monte Carlo simulations. The black dots show the normalized distribution of 5243 the events in $\mathcal{S}_{\text{obs}}$.

In ref [10], the two point correlation method was applied to the track-like events reconstructed by ANTARES during the period from 2007 to 2010, by using a cumulative representation of the 2 point distribution, with bins of equal size in angular distance. In addition, the contribution of each pair ij of events to the 2 point distribution was modified by applying a weight $\omega_{ij} = \omega_i \omega_j$, where ω_i and ω_j are individual weights associated to each event, and which are computed from $N_{\textsf{hit}}$ as follows

$$\omega_i = \int_0^{N^i_{\textsf{hit}}} dN_{\textsf{hit}} \int_0^{N^i_{\textsf{hit}}} f(N_{\textsf{hit}}|\textsf{Bartol}) dN_{\textsf{hit}} \tag{7.3}$$

where $f(N_{\textsf{hit}}|\textsf{Bartol})$ is the normalized distribution of hits under the atmospheric flux hypothesis. The results show that the use of weights enhance the discovery power of the analysis for a point-like source. Nevertheless, during the development of this work it has been identified that the use of weights presents a problem: If one wants to build a reference 2 point distribution equivalent to the one shown in figure 7.3 by including weights, it is necessary to generate a value of $N_{\textsf{hit}}$ for each event in the $\sim 10^5$ simulated background sky maps. This can be done easily by sampling a number from the distribution $f(N_{\textsf{hit}}|\textsf{Bartol})$ shown in figure 7.7. By following this procedure and by using weights like the one given in equation 7.3, the 2 point correlation distribution corresponding to each simulated background sky map would have a different integral. If one interprets the integral of the 2 point distribution as the total number of pairs of events in the sky map, one can conclude that the use of weights changes the total number of events in each simulated sky map. In the case that a significant difference were found in the data with respect to the background, it wouldn't therefore be possible to state whether this difference is produced by a clustering of events at a certain angular scale, or by an artificial excess of events in the analysed sample.

In this work, a different approach is followed with respect to the use of the energy. In order to test the impact that the usage of the $N_{\textsf{hit}}$ estimator has on the performance of the 2 point correlation analysis, an additional cut is applied on the sample $\mathcal{S}_{\textsf{obs}}$ by selecting the events with the highest values of $N_{\textsf{hit}}$. As a first attempt of testing this approach, the value of $N_{\textsf{hit}}$ that defines the cut has been chosen arbitrarily to be $N_{\textsf{hit}} = 50$, where the normalised atmospheric and cosmic distributions in figure 7.7 cross each other. A total of 1555 events in $\mathcal{S}_{\text{obs}}$ pass this cut. In order to avoid the problem of producing background samples with a different number of events each at the time of building the reference 2 point distribution, a total number of 5243 events are simulated for each background realization, where the value of N_{hit} for each event is sampled from the $f(N_{\text{hit}}|\text{Bartol})$ distribution. Then, the 2 point distribution is computed as the distribution of angular distances of the 1555 events with the highest values of N_{hit}.

7.4 Performance of the 2 point correlation analysis

In this section, the performance of the 2 point correlation analysis is tested under the different configurations presented in section 7.4. To do so, the discovery power of the method is computed for different types of sources of signal and compared for each of the configurations shown in figure 7.5:

1. Differential representation and bins of equal size in angular distance.
2. Differential representation and bins of equal size in solid angle.
3. Cumulative representation and bins of equal size in angular distance.
4. Cumulative representation and bins of equal size in solid angle.

In addition, each of these configurations is tested with and without the cut on the N_{hit} energy estimator mentioned in section 7.3.2. The sources of signal considered for this study are are just toy models whose morphologies resemble to those of potential neutrino sources. In particular, three different source morphologies are studied. A point-like source, the galactic plane, and a diffuse flux. Since the motivation of this chapter is just technical, the parameters that define the signal emission from the sources are chosen arbitrarily. Figure 7.8 shows three background-like sky maps where a certain amount of events have been replaced by events distributed in the previously mentioned sources.

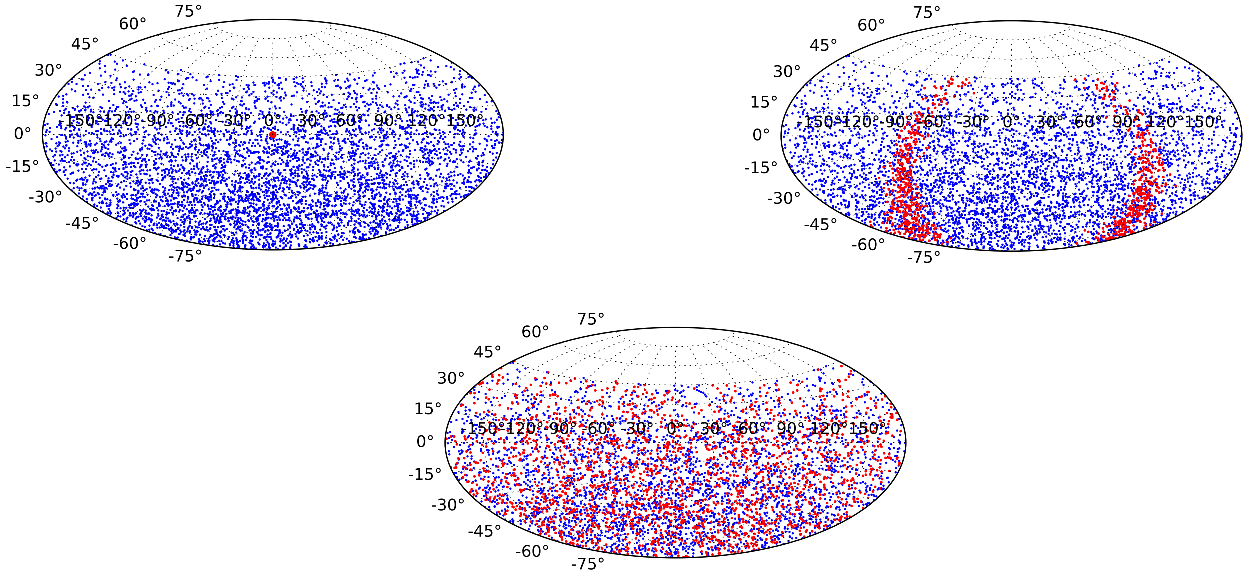

Figure 7.8: Sky maps showing in equatorial coordinates, the three kinds of source morphologies considered in this study: a point source centred in (0,0), a diffuse flux of neutrinos whose declinations follow an E^{-2} acceptance, and neutrinos in the galactic plane.

The single point source has been chosen to be located at the equatorial coordinates (0,0), and the events in the galactic plane have been injected according to the convolution of the ANTARES visibility and a distribution galactic coordinates which is uniform in galactic longitude, and follows a gaussian distribution in galactic latitude centred in the galactic plane with a $\sigma = 5\,\mathrm{deg}$. The diffuse flux, which is undistinguishable by naked eye from the atmospheric background, consists on signal events whose right ascensions follow a uniform distribution between 0 and 2π, and whose declinations are sampled from the relative acceptance for an E^{-2} spectrum shown in figure 7.2.

The discovery power of the 2 point correlation analysis to a certain neutrino source that produces N_ν reconstructed neutrinos in ANTARES is computed as follows:

1. First, the background distribution of the test statistic $f(\lambda|H_0)$, is computed as described in section 7.2.3, according to the chosen configuration of the 2 point distribution. Note that this distribution may also vary with the cut on N_{hit}.

2. Around 10^4 sky maps containing a number N_ν of signal events each are simulated, and the value of the test statistic is computed for each of them, as explained in section 7.2.3.

    - A sky map containing N_ν signal neutrinos $\mathcal{S}(N_\nu)$ is generated from a background-like sky map by reallocating N_ν randomly chosen events in new positions defined by the morphology of the source. The result is a new sky map that contains an excess of anisotropies with respect to the atmospheric background. In addition, a value of N_{hit} sampled from the cosmic distribution shown in figure 7.7 is assigned to each signal event
    - The 2 point distribution for $\mathcal{S}(N_\nu)$ is computed and compared to the reference in order to obtain the value of λ. If the cut on N_{hit} is applied, the 2 point distribution of $\mathcal{S}(N_\nu)$ is computed only with the 1555 events with the highest values of N_{hit}. Note that some of the injected signal events may be removed from the sample.

3. After performing the previous step, $\sim 10^4$ values of λ are obtained from which $f(\lambda|\mathcal{S}(N_\nu))$ can be computed.

4. From $f(\lambda|\mathcal{S}(N_\nu))$ and $f(\lambda|H_0)$, the discovery power of λ for $\mathcal{S}(N_\nu)$ is computed at a 3σ confidence level, by integrating $f(\lambda|\mathcal{S}(N_\nu))$ from $\lambda_{3\sigma}$ to ∞.

Figure 7.9 shows $f(\lambda|H_0)$ computed for the cumulative representation of the 2 point distribution where the bins have equal size in $\Delta\Omega$. Also $f(\lambda|\mathcal{S}(N_\nu))$ is shown for several values of N_ν, corresponding to a point source located in the equatorial coordinates (0,0). One can see that the higher is the number of reconstructed signal events in the sky map, higher is the difference between $f(\lambda|H_0)$ and $f(\lambda|\mathcal{S}(N_\nu))$, and therefore, higher is the discovery power of the test.

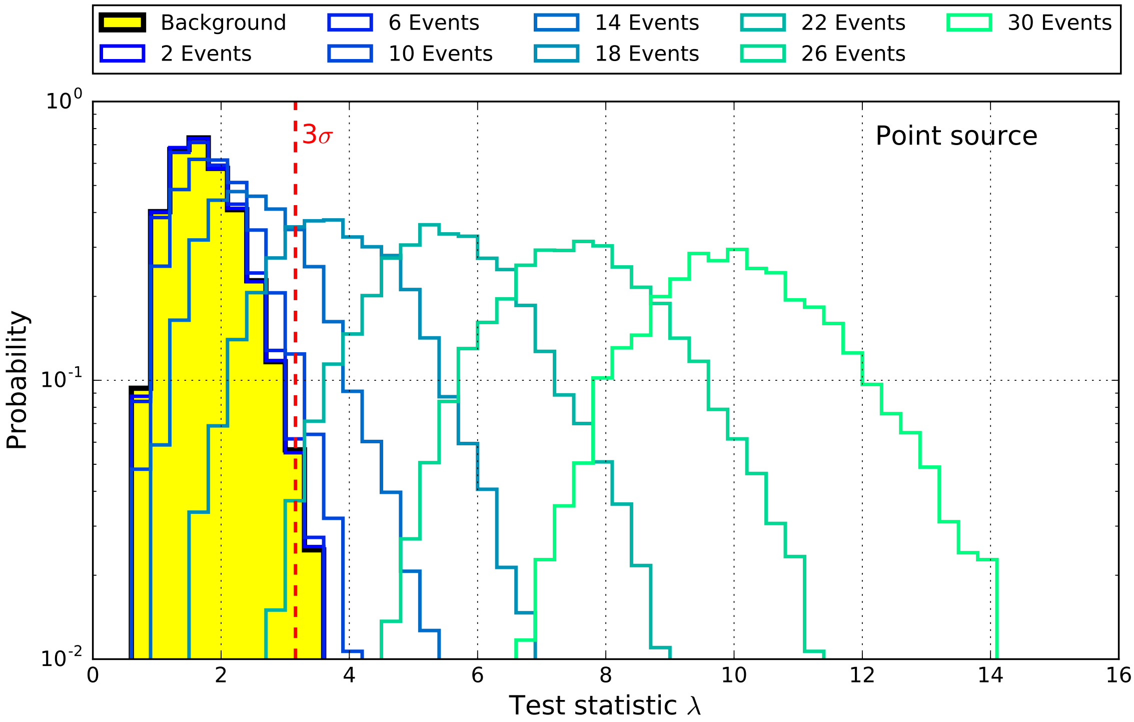

Figure 7.9: Distribution of the test statistics under the background hypothesis, and for a point source located in the equatorial coordinates (0,0), from which different amounts of reconstructed events are simulated

This process has been carried out for the three types of sources shown in figure 7.8, and for each of the configurations of the 2 point correlation distribution. In addition, this process has also been carried out with and without a cut on the number of hits. The results are shown in figure 7.10.

From the point of view of the cut on the number of hits, one can see that it works quite well for the point source and the galactic plane, while its effect is very bad for the diffuse flux. This can be easily understood. For a single point source, around 16 events are needed to produce a 3σ effect with a 50% probability without cutting on the number of hits. This number of events represents a small fraction of the total sample of 5243 events. When the cut on the number of hits is applied, the 3688 events with the lowest values of N_{hit} are removed from the sample. The chance of removing a signal event is small, since in the events injected in the point source have in average, a higher value for N_{hit} than the background events. Therefore, one can expect the same amount of signal events to be clustered around the source's position after applying the cut, while the amount of background events is significantly reduced. A similar argument can explain the improvement in the discovery potential for the events around the galactic plane. The fall on the discovery power for the diffuse flux is produced by a lack of statistics. The spatial distribution of the signal events in this case is so close to that of the background, that after applying the cut on N_{hit}, there are not enough events to distinguish if their distribution in declination follows the green or the blue curve in figure 7.2. On the other hand, regarding the different configurations of the 2 point distribution, it is clear that the differential representation when the bins have equal size in solid angle produces worse results than the other configurations. This happens because the number of bins in this representation ~ 4000 is so big, that the pairs produced by the signal events are distributed in different bins, and therefore represent a weak excess at each bin with respect to the background. If on the other hand, a cumulative representation is used, each of these differences are integrated and produce a bigger effect in a single bin, enhancing the detectability of the source. Whether it is more convenient to use bins of equal size on angular distance or in solid angle is not completely clear from these results. For a point source, better results are obtained when the bins have equal size in angular distance, while for the galactic plane and a diffuse flux, the results are very similar.

For the next chapters, the chosen configuration for the 2 point correlation distribution is a cumulative representation where the bins are of equal size on angular distance.

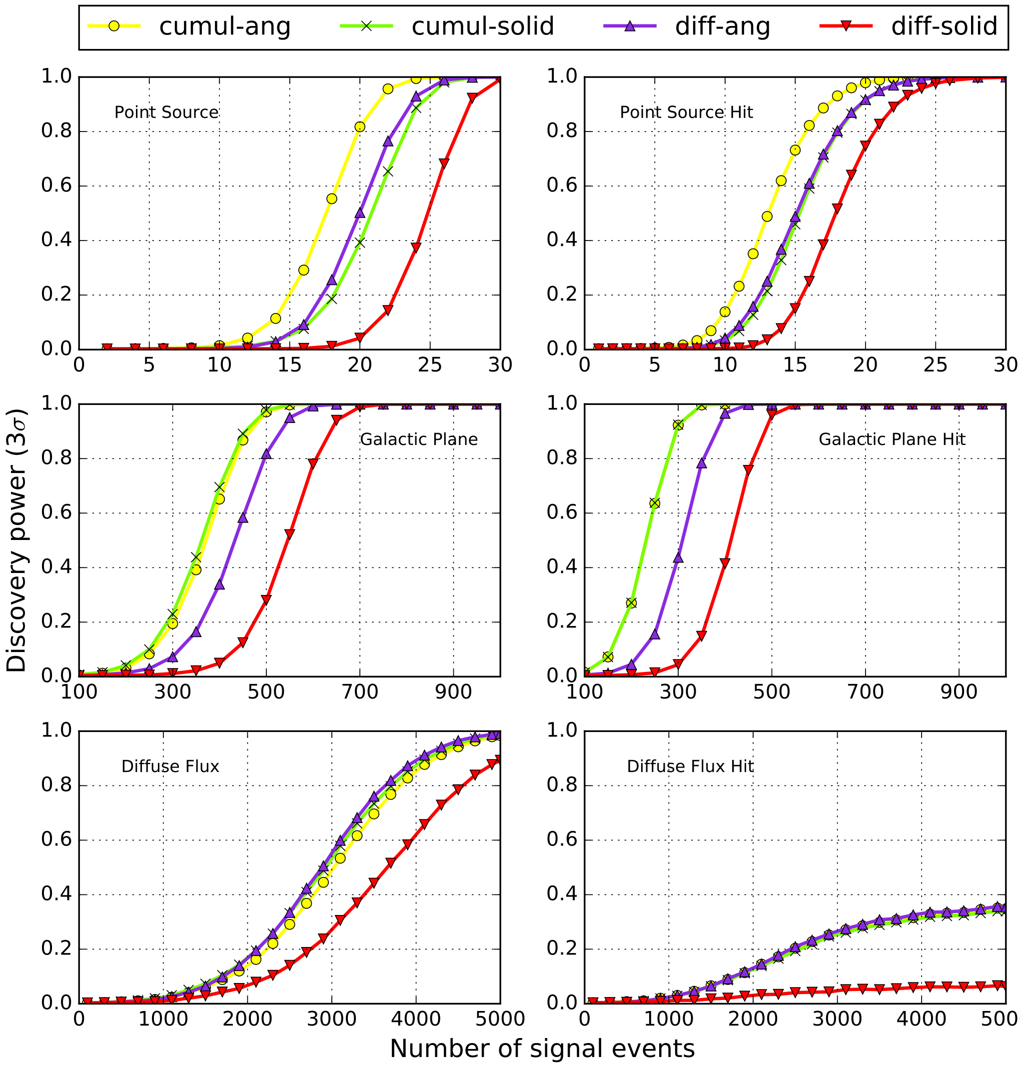

Figure 7.10: Discovery power of the 2 point correlation analysis under the different configurations of the 2 point distribution considered, for the three source types. The results with and without a cut on the number of hits are shown.

Chapter 8

Simulating neutrinos from AGN populations in ANTARES

8.1 Introduction

In chapter 2 a general description of the current knowledge about AGN is given based on the observations along the electromagnetic spectrum, and two scenarios are presented to describe the origin of high energy electromagnetic radiation. In the leptonic scenario, low energy photons are accelerated up to high energies by collisions with relativistic electrons while in the hadronic scenario high energy photons are produced in reactions of high energy protons with radiation or matter, in which high energy neutrinos are also expected to be produced. In the latter case, it is assumed that the diffusive shock acceleration mechanism of protons in the AGN jets produces a neutrino flux with an E^{-2} energy distribution[1]. Since there is not yet an observational evidence for the origin of the high energy electromagnetic radiation, none of the previously mentioned mechanisms should be discarded. A priori, both could be present in the same source, or just one of them. Therefore, one could expect a

---

[1] Note that this is a conventional approximation used in many analyses that is motivated by the 2nd order Fermi acceleration mechanism. the value of the spectral index may vary from -2.

fraction of the AGN present in the Universe to be neutrino sources. The current chapter deals with the simulation of neutrinos coming from AGN populations and their detection with the ANTARES neutrino telescope.

8.2 The general strategy

Several ingredients are necessary to simulate neutrinos from an AGN population. Roughly speaking, an AGN population is defined by the number of neutrino-emitter AGN N^{ν}_{AGN} and the number of neutrinos N^{det}_{ν} that ANTARES is expected to detect from each of them. The latter quantity depends on the neutrino emission from AGN through the neutrino luminosity L_{ν}, which is defined as the total energy emitted per unit time in neutrinos. Since no experimental information about L_{ν} or N^{ν}_{AGN} is available, they are assumed to be related to their electromagnetic counterparts, for which indeed there exist models based on experimental data. In particular, these quantities are estimated from AGN observations in the X-ray band.

Below I summarize the steps of the procedure that I have developed for simulating neutrinos from AGN populations in ANTARES:

1. **Definition of the number of neutrino sources in the population** Studies of the Swift/BAT and Chandra X-ray observations ([18], [84]), show a strong evidence that the observed X-ray properties of AGN change with their cosmological epoch. Notably, the X-ray luminosity distribution (i.e. the number of AGN emitting X-rays with a given luminosity L_X is found to depend on the redshift z. This dependence is used in section 8.3 to derive an AGN density $\rho_X(L_X, z)$ in the phase space defined by L_X and z. In this work the density of neutrino emitter AGN is assumed to be proportional to the density of X-ray emitter AGN,

$$\rho_{\nu} = \eta \cdot \rho_X \tag{8.1}$$

   where η is a proportionality factor that is allowed to vary. The density can be integrated in a given range of redshift and X-ray luminosity to find the number of neutrino sources in the population as a function of η, L_X and z,

$$N^{\nu}_{\mathsf{AGN}}(\eta, L_X, z) = \eta \int \rho(L_X, z) dL_X dz \tag{8.2}$$

2. **Neutrino detection from an AGN** For an AGN that produces a neutrino flux at the Earth given by $\phi^{\oplus}_{\nu}$, ANTARES is expected to detect a number of neutrinos N^{det}_{ν} that is related to $\phi^{\oplus}_{\nu}$ through the ANTARES acceptance $\mathcal{A}(E, \delta)$. This is a quantity that accounts for the detector's response to a neutrino flux and depends on its energy spectrum and on the declination (δ). $\phi^{\oplus}_{\nu}$ depends in turn on the AGN neutrino luminosity L_{ν} and on its luminosity distance $r_L(z)$. Here, the neutrino and X-ray luminosities are assumed to be proportional

$$L_{\nu} = k \cdot L_X, \tag{8.3}$$

   where k is another proportionally parameter allowed to vary. This allows to write the number of detected neutrinos as a function of z and L_X,

$$N^{\mathsf{det}}_{\nu} = N^{\mathsf{det}}_{\nu}(k, L_X, z) \tag{8.4}$$

3. **Population simulation** Finally a sky map containing a fraction of signal neutrinos detected from an AGN population is simulated as a function of the parameters η and k. First, the number of sources in the population is calculated, and for each of them a number of detected neutrinos is generated, which is related to the AGN X-ray emission properties through the parameter k. With this information a sky map $\mathcal{S}(\eta, k)$ is built from a background sky map $\mathcal{S}_{\mathsf{bg}}$ by replacing randomly chosen background events with events corresponding to the AGN neutrinos so that the total number of detected neutrinos in the sky map remains constant. Each of the neutrinos from an AGN is injected within a 2D gaussian point spread function (p.s.f.) centred in the location of the source, that is distributed according to the ANTARES acceptance for an E^{-2}

spectrum.

8.3 Number of AGN in the Universe

The number density of AGN can be computed from their luminosity function which is defined as the number of AGN per unit comoving volume and per unit luminosity interval. In the X-ray band it is called X-ray luminosity function (XLF) and written as

$$\Phi(L_X, z) = \frac{d^2N}{dV_c dL_X} \tag{8.5}$$

In this work, the procedure followed in ref. [59] is used to compute the AGN number density. In this reference the results of studies done in AGN populations observed by Swift/BAT on one hand [18] and Chandra on the other [84] are used. In the former study, the observations of blazars by Swift/BAT are used to compute the XLF for blazars and for the blazar subclasses FSRQ and BL Lac. The used sample contains data for 38 blazars with redshifts in the range $0.03 < z < 4.0$, 12 of which are identified with BL Lac objects and the rest 26 being FSRQ. In [84], the XLF for AGN is computed by using data from 682 AGN observed in the X-ray band by Chandra. This sample contains both, radio loud and radio quiet objects with redshifts up to $z \sim 5$. In both studies data are fitted to a parametric functional form to obtain the XLF as a function of z and L_X. The results obtained are the following.

The Swift/BAT blazar sample was used to derive the XLF for blazars, FSRQ and BL Lac objects. The XLF for Blazars and FSRQ is described by

$$\Phi(L_X, z) = \frac{A}{\ln(10)\mathcal{L}(L_X, z)} \left[\left(\frac{\mathcal{L}(L_X, z)}{L_*} \right)^{\gamma_1} + \left(\frac{\mathcal{L}(L_X, z)}{L_*} \right)^{\gamma_2} \right]^{-1} \Theta_{CF} \tag{8.6}$$

while the XLF for BL Lac objects is given by

$$\Phi(L_X, z) = \frac{A}{\mathcal{L}(L_X, z)} \left(\frac{\mathcal{L}(L_X, z)}{L_*} \right)^{1-\gamma_2} \Theta_{CF} \tag{8.7}$$

In both cases $\mathcal{L}(L_X, z)$ describes the cosmological evolution of the X-ray emission from AGN,

$$\mathcal{L}(L_X, z) = \frac{L_X}{(1+z)^{v_1+v_2 z}} \tag{8.8}$$

On the other hand, the XLF for radio galaxies is estimated from the Chandra sample by considering that these objects constitute the 10% of the total sample. It is described by

$$\Phi(L_X, z) = \frac{A}{\ln(10) L_X}\left[\left(\frac{L_X}{L_*}\right)^{\gamma_1} + \left(\frac{L_X}{L_*}\right)^{\gamma_2}\right]^{-1} \Theta_{CF}\,\xi(L_X, z) \tag{8.9}$$

In this case the cosmological evolution of the X-ray emission is contained in the function $\xi(L_X, z)$ which is given by

$$\xi(z, L_\mathrm{X}) = \begin{cases} (1+z)^{v_1} & [z \leqslant z_*(L_\mathrm{X})] \\ e(z_*(L_\mathrm{X}))\left[\dfrac{1+z}{1+z_*(L_\mathrm{X})}\right]^{v_2} & [z > z_*(L_\mathrm{X})] \end{cases}, \tag{8.10}$$

and

$$z_*(L_\mathrm{X}) = \begin{cases} z_\mathrm{c}\left[\dfrac{L_\mathrm{X}}{L_\mathrm{c}}\right]^{\alpha} & (L_\mathrm{X} < L_\mathrm{c}) \\ z_\mathrm{c} & (L_\mathrm{X} \geqslant L_\mathrm{c}) \end{cases}. \tag{8.11}$$

Table 8.1 shows a summary of the parameters that define the XLF of these 4 families of objects. Following ref. [59] the AGN space density is computed as

$$\rho_X(L_X, z) = \frac{d^2N}{dL_X dz} = \Phi(L_X, z) \cdot \frac{dV_c}{dz} \tag{8.12}$$

Figure 8.1 shows the density for the 4 families of objects as a function of L_X and z. In each case, L_X varies within the range provided by observations and z is considered up to values of $z = 10$. Note that the AGN with the highest observed redshift corresponds to $z \sim 7$. An estimation of the number of objects of each class in these redshift and luminosity ranges can be calculated by integrating the density and are

Table 8.1: Parameters that allow to calculate the AGN density for the different families according to [18] [84] and [59].

Model	$(A, \log A)$	$(L_*, \log L_*)$	(γ_1)	(γ_2)	(υ_1)	(υ_2)	(z_c)	$(\log L_c)$	(α)	Θ_{CF}
RG	-6.077^a	44.33	2.15	1.10	4.00	-1.5	1.9	44.6	0.317	1
Blazar	1.379×10^{-7}	1.81^b	-0.87	2.73	3.45	-0.25	–	–	–	400
FSRQ	0.175×10^{-7}	2.42^b	$< -50.0^c$	2.49	3.67	-0.30	–	–	–	400
BL Lac	0.830×10^{-7}	1.0^b	–	2.61	-0.79	–	–	–	–	400

Notes. [a]The value represents $\log A$. [b]The value represents L_*, where the luminosities have units of $L_{44} = 10^{44}$ erg s^{-1}. [c]In these calculations used $\gamma_1 = -50.0$ is used.

- **Blazars:** $8.6 \cdot 10^8$
- **Radio Galaxies:** $9.2 \cdot 10^7$
- **FSRQ:** $2.6 \cdot 10^7$
- **BL Lac:** $2.2 \cdot 10^5$

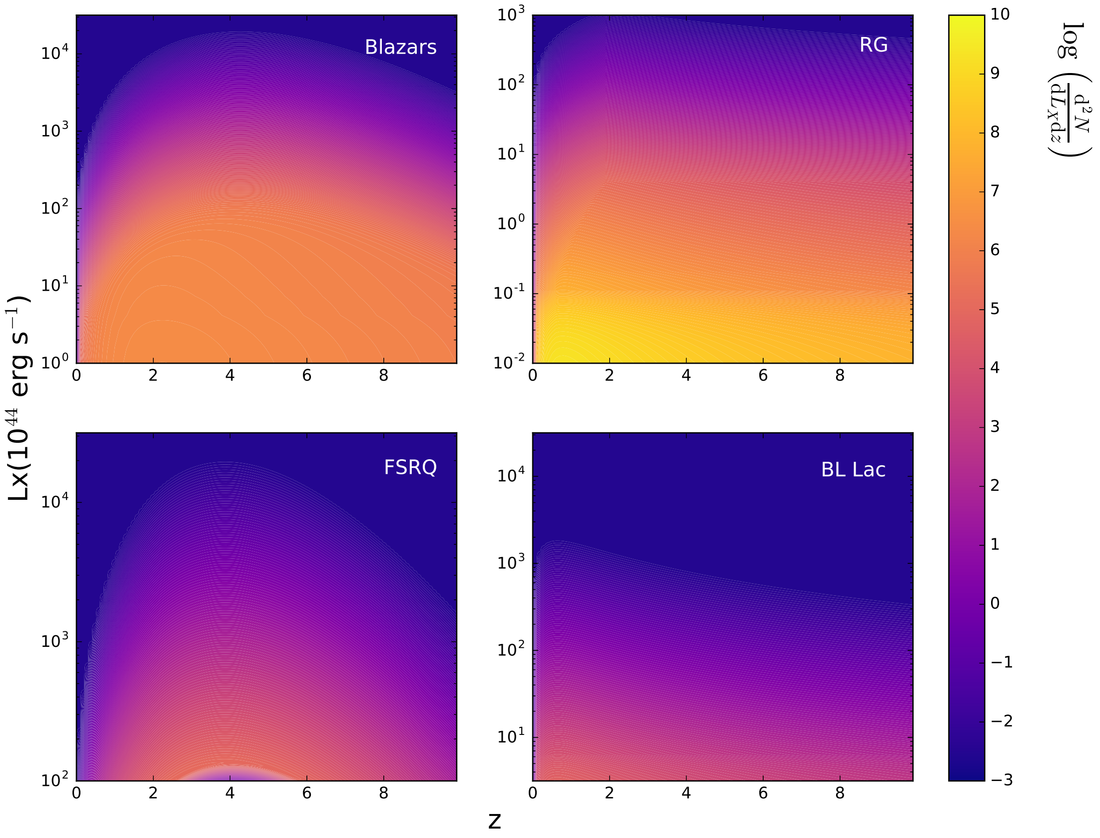

Figure 8.1: AGN density in the phase space z , L_X

8.4 AGN neutrinos in ANTARES

8.4.1 Detected neutrinos from an AGN

The number of detected neutrinos that a source is expected to produce in ANTARES can be found by recalling the definition of the effective area $\mathcal{S}_{\text{eff}}$, which is the ratio between the rate of detected neutrinos and the neutrino flux produced by the source at the Earth,

$$\mathcal{S}_{\mathsf{eff}}(\delta, E_\nu) = \frac{R_\nu(E_\nu, \delta)}{\phi_\nu^\oplus(E_\nu, \delta)} \tag{8.13}$$

where $\phi_\nu^\oplus$ has units of $(GeV^{-1}cm^{-2}s^{-1})$, and R_ν has units of $GeV^{-1}s^{-1}$. An estimation of the number of neutrinos that ANTARES is expected to detect during a time period Δt, with energies $E_{\mathsf{min}} < E < E_{\mathsf{max}}$, from a source at a certain declination δ can be obtained by computing the integral

$$N_\nu^{\mathsf{det}} = \int_{E_{\mathsf{min}}}^{E_{\mathsf{max}}} \mathcal{S}_{\mathsf{eff}}(\delta, E_\nu)\phi_\nu^\oplus(E_\nu)dEdt \tag{8.14}$$

For sources emitting neutrinos with a spectral energy distribution given by an E^{-2} power-law, the neutrino flux at the Earth can be written as $\phi_\nu^\oplus = \phi_0^\oplus \cdot E^{-2}$ where $\phi_0^\oplus$ is called the normalization flux of the source at the Earth and has units of $(GeV \cdot cm^{-2} \cdot s^{-1})$. Using this expression in 8.14, the number of detected neutrinos can be rewritten as

$$N_\nu^{\mathsf{det}} = \phi_0 \langle A \rangle_\delta \tag{8.15}$$

where $\langle A \rangle_\delta$ is called the acceptance at the declination δ, and has units of $(GeV^{-1} \cdot cm \cdot s)$.

N_ν^{det} can be computed as a function of the intrinsic properties of a source by relating $\phi_0^\oplus$ with the source luminosity. For an AGN at a redshift z and characterized by a neutrino luminosity L_ν, the amount of energy arriving at the Earth per unit time can be written as

$$\varepsilon = \frac{L_\nu}{4\pi r_L^2(z)} \tag{8.16}$$

where $r_L(z)$ is the luminosity distance, given by

$$r_L(z) = (1+z) \cdot c \int_0^z \frac{dz'}{H_0\sqrt{(1+z)^2(1+\Omega_M z) - 2(2+z)\Omega_\Lambda}} \tag{8.17}$$

if the source emits neutrinos with an $\sim E^{-2}$ spectrum, equation 8.16 can be rewritten as

$$\frac{L_\nu}{4\pi r_L^2(z)} = \int_{E_{\text{min}}}^{E_{\text{max}}} E\phi_\nu^\oplus dE = \int_{E_{\text{min}}}^{E_{\text{max}}} E\phi_0^\oplus E^{-2} dE = \phi_0^\oplus \text{log}\left(\frac{E_{\text{max}}}{E_{\text{min}}}\right) \tag{8.18}$$

Assuming that the neutrino luminosity relates to the X-ray luminosity by a proportionality constant as defined in equation 8.3, the expected number of events for a source at redshift z and with X-ray luminosity L_X can be written as

$$N_\nu^{\text{det}} = \frac{kL_X}{4\pi r_L^2(z)} \langle A \rangle \left[\text{log}\left(\frac{E_{\text{max}}}{E_{\text{min}}}\right)\right]^{-1} \tag{8.19}$$

where $\langle A \rangle$ is the average value of the acceptance for all the declinations. Figure 8.2 shows N_ν^{det} in the considered range for L_X and z for $k = 1$. Note that this number depends on the chosen energy range. In this work, the range 1GeV$< E < 1$PeV is considered.

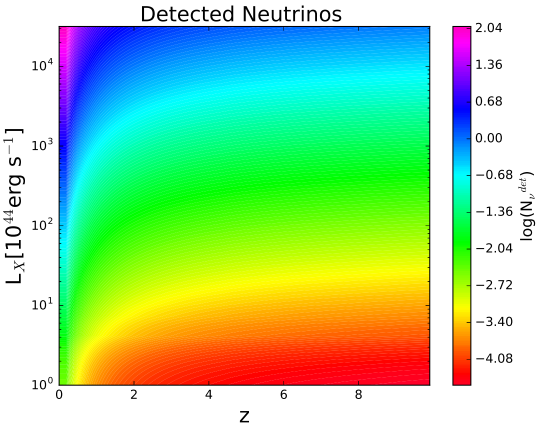

Figure 8.2: Number of detected neutrinos by ANTARES as a function of the redshift and X-ray luminosity, as computed by equation 8.19 for k=1

8.4.2 The mean detected neutrino distribution

For each source N_ν^{det} should be simulated so that the distribution of detected neutrinos for all the sources in the population is consistent with the AGN luminosity and redshift distribution in the Universe. This can be achieved by sampling a value of L_X and z for each source from the density distribution 8.1, and using them to compute N_ν^{det} from equation 8.19. Nevertheless, this process is expensive in terms of computation time and a different approach is used. Instead of using a distribution of AGN in L_X and z as the ones shown in figure 8.1, these distributions together with equation 8.19 are used to build a distribution of AGN as a function of the mean number of detected neutrinos $\langle N_\nu^{\text{det}} \rangle$. This allows to sample a value of $\langle N_\nu^{\text{det}} \rangle$ for each AGN in the population, which in turn can be used to sample N_ν^{det} from a Poisson distribution. This procedure is less expensive in computation time than sampling z and L_X for each source, and then solving 8.19. The distribution of AGN in $\langle N_\nu^{\text{det}} \rangle$ is built by the following procedure:

1. The phase space (L_X, z) is divided into a high number of bins ($\sim 10^4$) where each bin is characterized by 2 points $(L_X^{\text{min}}, z^{\text{min}})_{ij}$ and $(L_X^{\text{max}}, z^{\text{max}})_{ij}$, and where the bins are small enough that the AGN density can be considered constant inside of each bin.

2. The number of AGN contained inside the bin (ij) is computed by integrating the density,

$$(N_{\text{AGN}})_{ij} = \int_{ij} \rho dL_X dz \tag{8.20}$$

3. The mean number of detected neutrinos for an AGN in the bin (ij) is computed as

$$\langle N_\nu^{\text{det}} \rangle_{ij} = \frac{\int_{ij} \rho N_\nu^{\text{det}} dL_X dz}{\int_{ij} \rho dL_X dz} \approx \frac{1}{\Delta L_X \Delta z} \int_{ij} N_\nu^{\text{det}} dL_X dz \tag{8.21}$$

   where the approximation that the density is constant in the bin has been used and $\Delta L_X \Delta z$ is the area of the bin (ij).

4. A distribution is built with $\langle N_\nu^{\text{det}} \rangle$ in the X axis. For each bin (ij), the number of entries of the distribution at $\langle N_\nu^{\text{det}} \rangle_{ij}$ is increased by $(N_{AGN})_{ij}$.

The $\langle N_\nu^{\text{det}} \rangle$ distribution for the 4 AGN families are shown in figure 8.3 for different values of k, and normalized to 1.

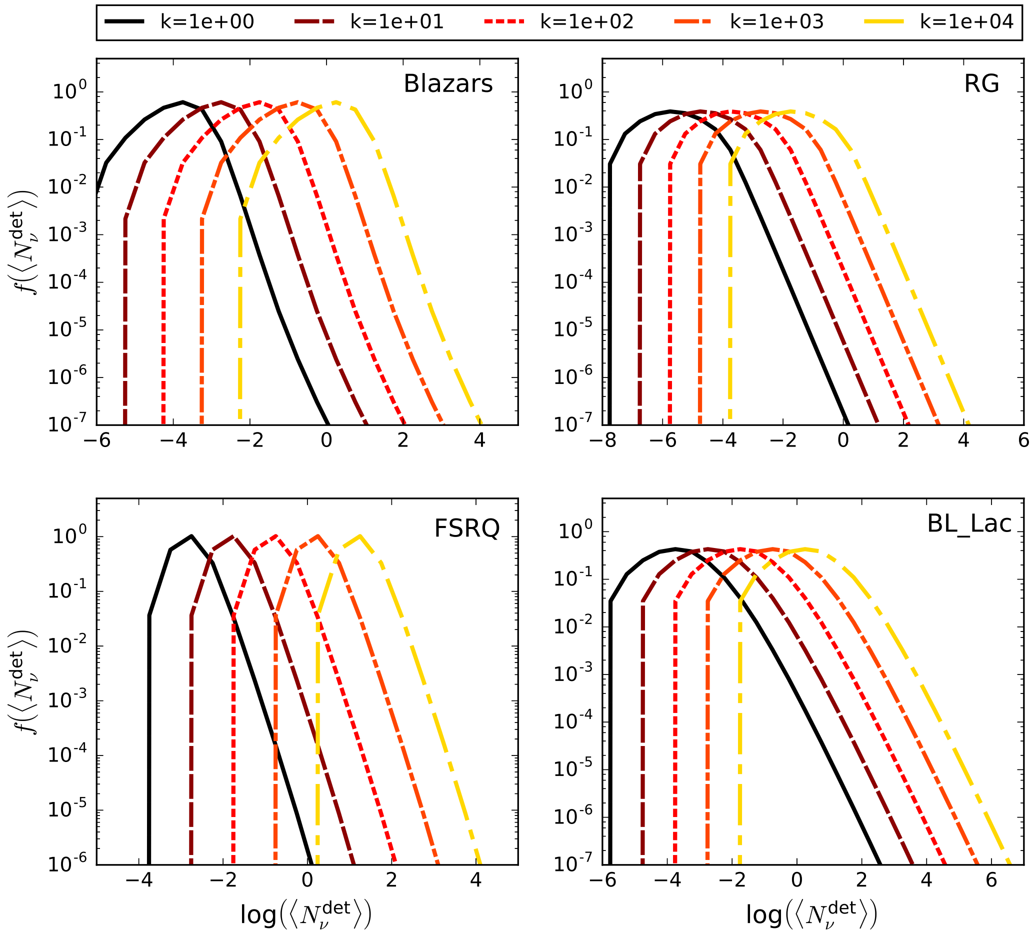

Figure 8.3: Probability density functions of the mean number of detected neutrinos for each AGN class.

8.5 Simulating a population

Simulating an AGN population characterized by the parameters η, k consists in generating a sky map $\mathcal{S}(\eta, k)$ that contains background events and signal events corresponding to sources in the population. The simulation process follows the steps below

1. A number of sources N_S is determined by the choice of η, as a fraction of the total

number of AGN that are X-ray emitters in the considered range of L_X and z.

2. A background-like sky map $\mathcal{S}_{\mathsf{bg}}$ is generated as described in 7.1.

3. For each source in the population,

    (a) The source location in the right ascension and declination (α, δ) is generated from a flat distribution

    (b) $\langle N_\nu^{\mathsf{det}} \rangle$ is sampled from the distribution as the ones shown in 8.3, corresponding to the choice of k.

4. Since the ANTARES visibility is not uniform in declination, a visibility weight is computed for each source and applied to the number of neutrinos that it produces in ANTARES as a function of its declination. For the i^{th} source in the population, this weight is calculated as

$$(\omega_v)_i = \frac{\mathcal{A}(\delta)_i}{\mathcal{F}(\delta)_i} \frac{N_S}{\sum_{j=N_S} \frac{\mathcal{A}(\delta)_j}{\mathcal{F}(\delta)_j}} \tag{8.22}$$

    where $\mathcal{A}(\delta)$ and $\mathcal{F}(\delta)$ represent the ANTARES acceptance distribution in declination calculated for an E^{-2} spectrum, and a flat acceptance, corresponding to the averaged acceptance over the full sky. The ratios in equation 8.22 are calculated at the declination of each source.

5. For each source, N_ν^{det} is sampled from a Poisson distribution,

$$(N_\nu^{\mathsf{det}})_i = P(\langle N_\nu^{\mathsf{det}} \rangle_i \cdot (\omega_v)_i) \tag{8.23}$$

6. The position of each neutrino in the source is generated from a 2D gausian distribution centred in the source's coordinates

7. As a result from the previous steps, a collection of coordinates of the signal neutrinos is obtained, $\{(\alpha, \delta)_\nu\}$. For each of the signal neutrinos, a neutrino in $\mathcal{S}_{\mathsf{bg}}$ is removed

from its position and reallocated in the signal neutrino's coordinates.

Chapter 9

Search for neutrinos from AGN populations with ANTARES

9.1 Introduction

In chapter 7, the 2 point correlation analysis has been presented as method for searching for an excess of anisotropies in background dominated sky maps. It is a model independent method, and therefore it is not optimised for the detection of any particular source of anisotropies. The study presented in section 7.4 shows that nevertheless, the 2 point correlation analysis is sensitive to anisotropies produced by sources of different morphologies, on the contrary to the majority of the other analysis methods such as the likelihood based search for point sources. The goal of this work is to exploit the versatility of the 2 point correlation analysis by searching for signal from populations of faint sources. In particular, this is done for populations of AGN which are simulated as described in chapter 8.

In section 8.5, the simulation of a sky map containing anisotropies produced by AGN populations characterized by the parameters η and k is described. These parameters represent respectively the number X-ray emitter AGN that are also neutrino emitters, and the proportionality between their luminosity in X-rays and in neutrinos. Different combinations of these parameters produce populations of different kinds. Populations with low values of η and high values of k will contain a low number of sources which present a strong neutrino emission, and populations with a high value of η and a low value of k will present with large numbers of faint sources. In section 9.2, the conditions under which a certain couple (η, k) produce populations that represent a realistic physical situation are explored. One should also bare in mind that within the set of all the possible couples (η, k) that represent realistic populations, not all of them are worth to be analysed. For instance, certain couples may represent populations that wouldn't produce any detected neutrino in the ANTARES detector, or populations for which the number of detected neutrinos is too low to produce a statistically significant signal. By accounting for these considerations, an area of the phase space defined by η and k is defined for each AGN type, which will be explored with the 2 point correlation analysis. For the different points in this area, the discovery power of the 2 point correlation analysis is computed by following the procedure described in chapter 7. This is presented in section 9.3.

Finally, in section 9.4 the results of the 2 point correlation analysis applied to the ANTARES data set $\mathcal{S}_{\text{obs}}$ are shown, with and without applying a cut on the N_{hit} energy estimator. Since none of these results are statistically significant, the existence of populations characterized by certain combinations (η, k) can be excluded. Since the parameter k is directly related to the mean number of detected neutrinos produced by each source in the population, a mean value of the flux per source in the populations can be computed for each couple (η, k), and the excluded region can be compared to the limits on the point source flux that have been previously set by IceCube or ANTARES.

9.2 Choosing the ranges for η and k

The amount of possible combinations of the parameters η and k is a priori very large. Since nevertheless these parameters have a physical meaning, the area of the phase space that they define can be constrained to those values of η and k that represent populations which are realistic from a physical point of view, and which are detectable by the 2 point correlation analysis.

The first criterion to consider is related to the total number of sources in the population, which is defined by the parameter η (remember that this parameter is defined as the proportion of AGN emitting in the X-ray band, that also emit neutrinos). Here, the range of this parameter is constrained by assuming that there are no more AGN that emit neutrinos than AGN that emit electromagnetic radiation in the X-ray band, and by assuming that at least one AGN emitting in the X-ray band is also a neutrino emitter. Based on these assumptions, the parameter η is constrained to the range $\sim 1/N^{\mathsf{X}}_{\mathsf{AGN}} < \eta < 1$[1]. The parameter k is chosen according to the overall signal that a population will produce in ANTARES. It has been shown in section 7.4, that when if a single point source produces more than ~20 neutrinos, the 2 point correlation would detect its presence (see figure 7.10). In order to save computing time, those populations which produce at least one source with at least 20 signal events are not analysed. In addition to this, populations that would produce a large amount of detected neutrinos compared to the total number of events in $\mathcal{S}_{\mathsf{obs}}$ are regarded as unrealistic, since a significantly large fraction of the reconstructed events is expected to be atmospheric neutrinos. In this work, a minimum of 70% of atmospheric neutrinos is required in the sample. Since $\mathcal{S}_{\mathsf{obs}}$ has a total of 5243 events, only those populations producing less than 1573 signal events are considered. From figure 7.10, one can already advance that if these 1573 events are distributed as a diffuse flux, the 2 point correlation analysis cannot detect them. Therefore, the couples (η, k) that represent populations where each source produces at most one detected neutrino are not considered. Similarly, the couples (η, k) which don't produce signal events are also discarded.

---

[1] I've expressed the lower limit of η as an approximate quantity, $\sim 1/N^{\mathsf{X}}_{\mathsf{AGN}}$. The actual value that I've used for this bound is $1/\mathcal{O}(N^{\mathsf{X}}_{\mathsf{AGN}})$, where $\mathcal{O}(N^{\mathsf{X}}_{\mathsf{AGN}})$ represents the order of magnitude of $N^{\mathsf{X}}_{\mathsf{AGN}}$. For instance, the total amount of blazars in the considered ranges of redshift and luminosity is $8.6 \cdot 10^8$ and the minimum value of η considered here is 10^{-8}. This means that the population with the lowest number of blazars considered here, has 8 blazars. As one will see in section9.4 this doesn't affect the final conclusions of the study.

The choice of the parameters η and k is done according to the following criteria:

1. Couples (η, k) which produce more detected neutrinos than the 30% of the total number of events in $\mathcal{S}_{\mathsf{obs}}$ should satisfy

$$\eta \cdot N_{\mathsf{AGN}}^{\mathsf{X}} \cdot \int \langle N_{\nu}^{\mathrm{det}} \rangle f(\langle N_{\nu}^{\mathrm{det}} \rangle) d\langle N_{\nu}^{\mathrm{det}} \rangle > 1573 \tag{9.1}$$

2. Couples (η, k) that produce 0 detected neutrinos must satisfy

$$(1 - E(1))^{\eta \cdot N_{\mathsf{AGN}}^{\mathsf{X}}} > 0.9 \tag{9.2}$$

   where $E(1)$ is the expected value for 1 source to produce at least 1 detected neutrino, that can be calculated as

$$E(1) = \int f(\langle N_{\nu}^{\mathrm{det}} \rangle) \cdot P(\langle N_{\nu}^{\mathrm{det}} \rangle)_1 d\langle N_{\nu}^{\mathrm{det}} \rangle \tag{9.3}$$

   where $P(\langle N_{\nu}^{\mathrm{det}} \rangle)_1$ represents the Poisson distribution with mean value $\langle N_{\nu}^{\mathrm{det}} \rangle$, integrated for values higher than 0. In other words, it is the probability that a random sampling from a Poisson distribution with mean $\langle N_{\nu}^{\mathrm{det}} \rangle$ will produce a number higher than 0.

3. Similarly, couples (η, k) for which each source produces less than 2 neutrinos can be found by requiring analysed.

$$E(2) = \int f(\langle N_{\nu}^{\mathrm{det}} \rangle) \cdot P(\langle N_{\nu}^{\mathrm{det}} \rangle)_2 d\langle N_{\nu}^{\mathrm{det}} \rangle > 0.9 \tag{9.4}$$

4. Couples (η, k) that produce at least 20 neutrinos satisfy,

$$E(20) = \int f(\langle N_{\nu}^{\mathrm{det}} \rangle) \cdot P(\langle N_{\nu}^{\mathrm{det}} \rangle)_{20} d\langle N_{\nu}^{\mathrm{det}} \rangle > 0.9 \tag{9.5}$$

Figure 9.1 shows $P(\langle N_\nu^{\rm det}\rangle)_1$, $P(\langle N_\nu^{\rm det}\rangle)_2$ and $P(\langle N_\nu^{\rm det}\rangle)_{20}$ together with the pdf for $\langle N_\nu^{\rm det}\rangle$ for BL Lac populations characterised by two different values of k, and figure 9.2 shows the considered region in the phase space (η, k) for each AGN class. In each case, the dark blue area represents those AGN populations with at least one powerful AGN. One can see that for BL Lac, which are the least abundant objects, the region for which many faint sources would produce a high number of detected neutrinos is very small in comparison with the rest of the cases.

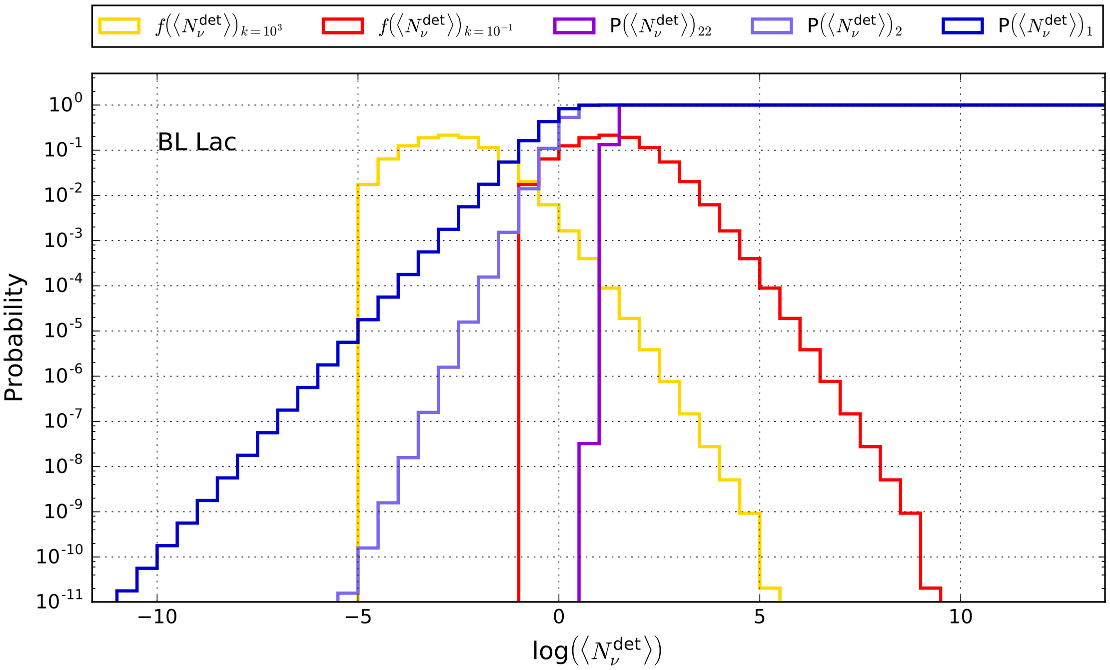

Figure 9.1: Probability distribution of the mean number of detected neutrinos for BL Lac objects (yellow and red curves), together with the probability that a Poisson distribution of mean $\langle N_\nu^{\rm det}\rangle$ produces more than 1,2 and 20 detected neutrinos respectively.

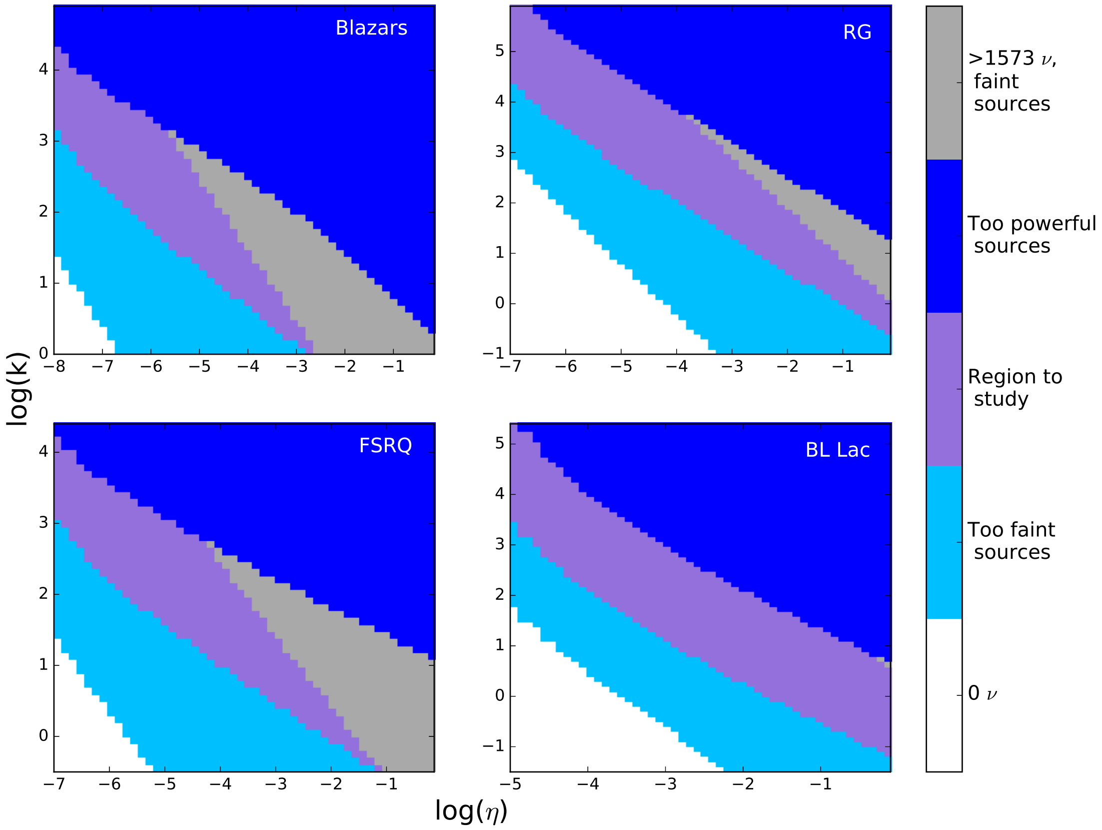

Figure 9.2: Parameters to study with the 2 point correlation analysis (purple area). The dark blue area corresponds to the set of parameters for which at least one powerful AGN would be present in the population. The gray area indicates those parameters for which a population that being composed by a high number of faint sources, would produce too many detected neutrinos. The light blue and the white and white areas, show those parameters for which each of the sources would produce no more than a single detected neutrino and 0 neutrinos respectively.

9.3 ANTARES discovery power for AGN populations

For each of the couples (η, k) represented with red color in figure 9.2, the discovery potential of the 2 point correlation analysis has been calculated following the method described in section 7.4. The results are shown in figure 9.3

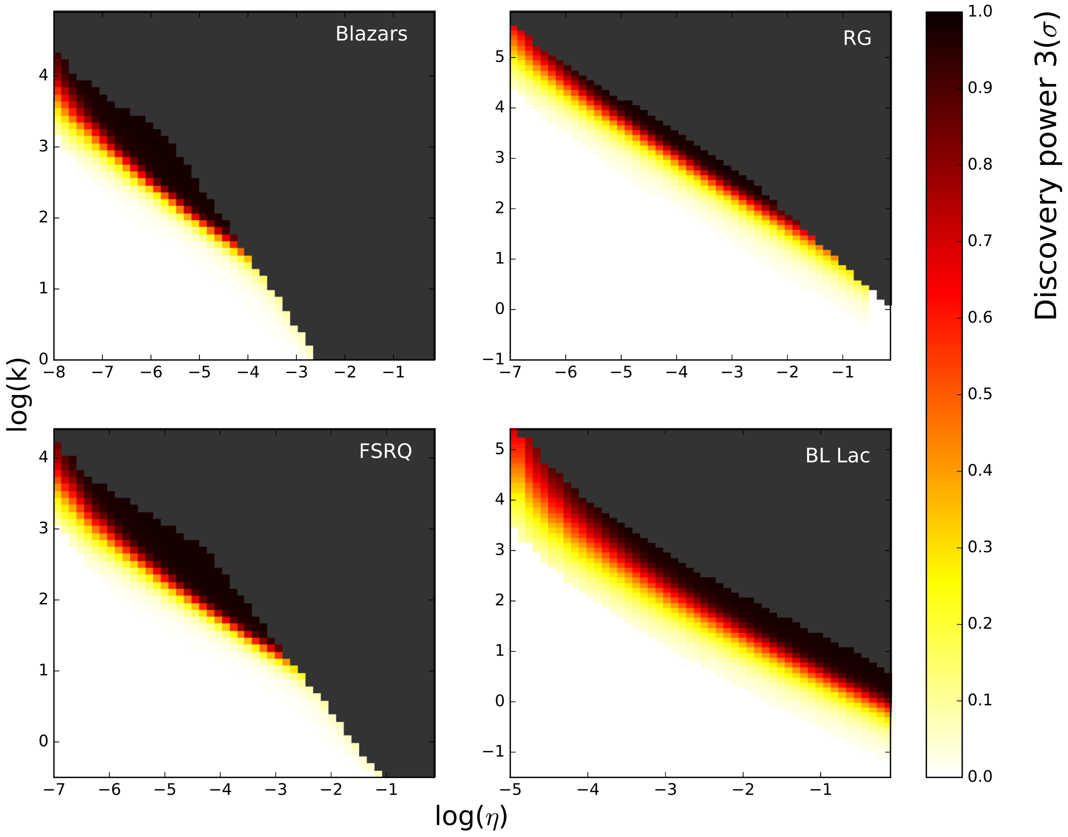

Figure 9.3: Discovery power of the two point correlation for populations of different AGN classes defined by different values of the parameters η and k.

9.4 Results

After performing the 2 point correlation analysis with the observed events $\mathcal{S}_{\text{obs}}$, a p-value of 0.027 is found without a cut on the number of hits, and the result is therefore not statistically significant to reject the background only hypothesis. With a cut on the number of hits, the corresponding p-value is 0.49, which is neither statistically significant.

When the analysis of the observed data does not produce a statistically significant result, the observed value of the test λ_{obs} can be used to exclude the existence of models of sources of signal. For the AGN populations, all the combinations (η, k) for which a value of the test higher than λ_{obs} would be observed in at least a 90% of the cases, are said to be excluded with a 90% confidence level. The values of η and k which are excluded by the 2 point correlation analysis are shown in figure 9.4.

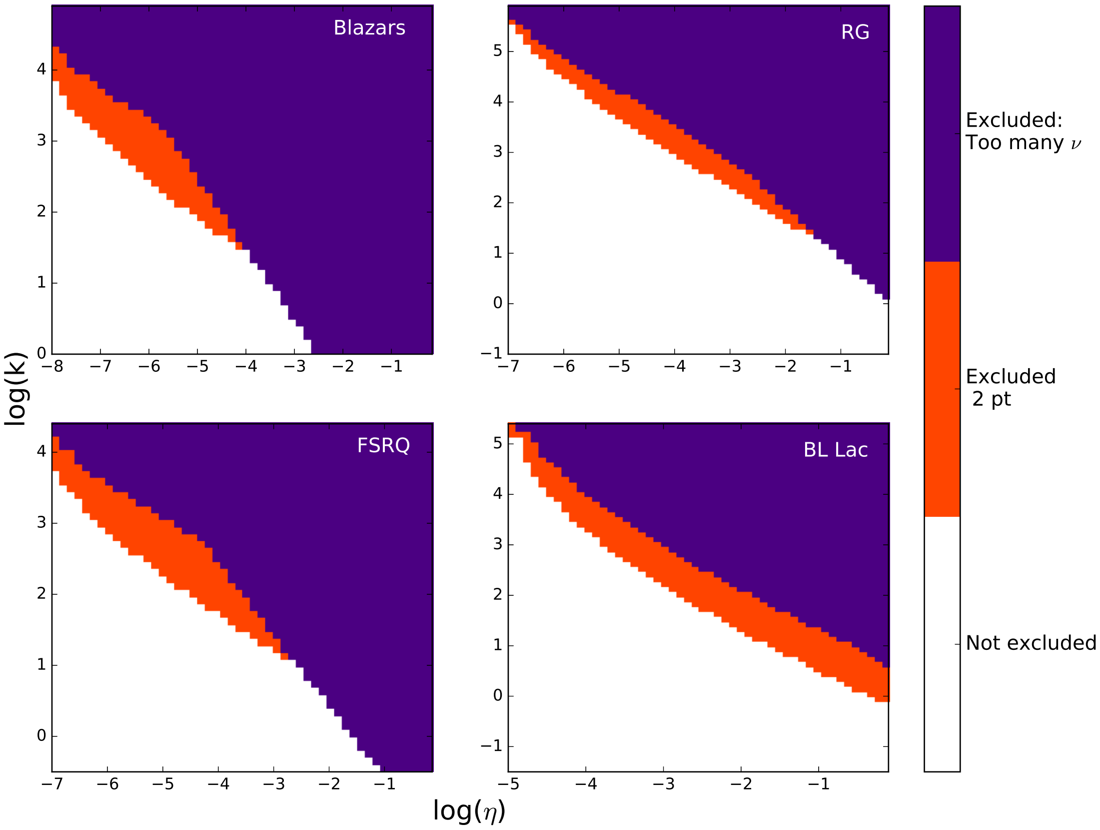

Figure 9.4: 90 % confidence level upper limits set on the phase space (η, k) for the different classes of AGN. The orange area represents the parameters that have been excluded by the 2 point correlation analysis, and the purple area corresponds to those populations for which a too high number of neutrinos would be detected.

As it is mentioned in the introduction to this final chapter, the limits shown in figure 9.4 can be expressed as limits to a mean neutrino flux ϕ_0 from a point-like source. Since the parameter k is directly related to the mean number of detected neutrinos from an AGN as it is shown in figure 8.3, this parameter can be related to a mean neutrino flux emitted from an AGN, by using the acceptance as it is described in section 8.4.

Figure 9.5 shows for each AGN class, the region of the phase space (η, k) that has been considered in this analysis. The gray color scale shows the mean flux per source which is independent of the parameter η, and which increases with the value of k. Note that the correspondence between the values of k and ϕ_0 is different for each AGN class because the relation between k and the mean number of detected neutrinos per source depends on the distribution of sources in z and L_X, which is different for each AGN class as it has been explained in chapter 8. This figure also shows the upper limits set by the 2 point correlation analysis in the parameter space (η, k) as a magenta dashed line, and the boundary (black dashed line) of the region which corresponds to AGN populations that would produce too many detected neutrinos in ANTARES, and which can be safely considered as excluded. Additionally, upper limits on the neutrino flux from a point source are shown for IceCube (yellow), ANTARES (red) and a combined analysis using both data sets (green) are shown. These values have been extracted from reference [1], where a search for point sources is performed with the ANTARES and IceCube data sets separately, and with a combination of both. The search method consists on finding the most significant cluster in a given sky region, and the search was performed for different declination values in the range $-1.0 < \sin(\delta) < 0$. The corresponding lines in figure 9.5 show the median values over all the declinations for each of the data sets for an E^{-2} energy spectrum.

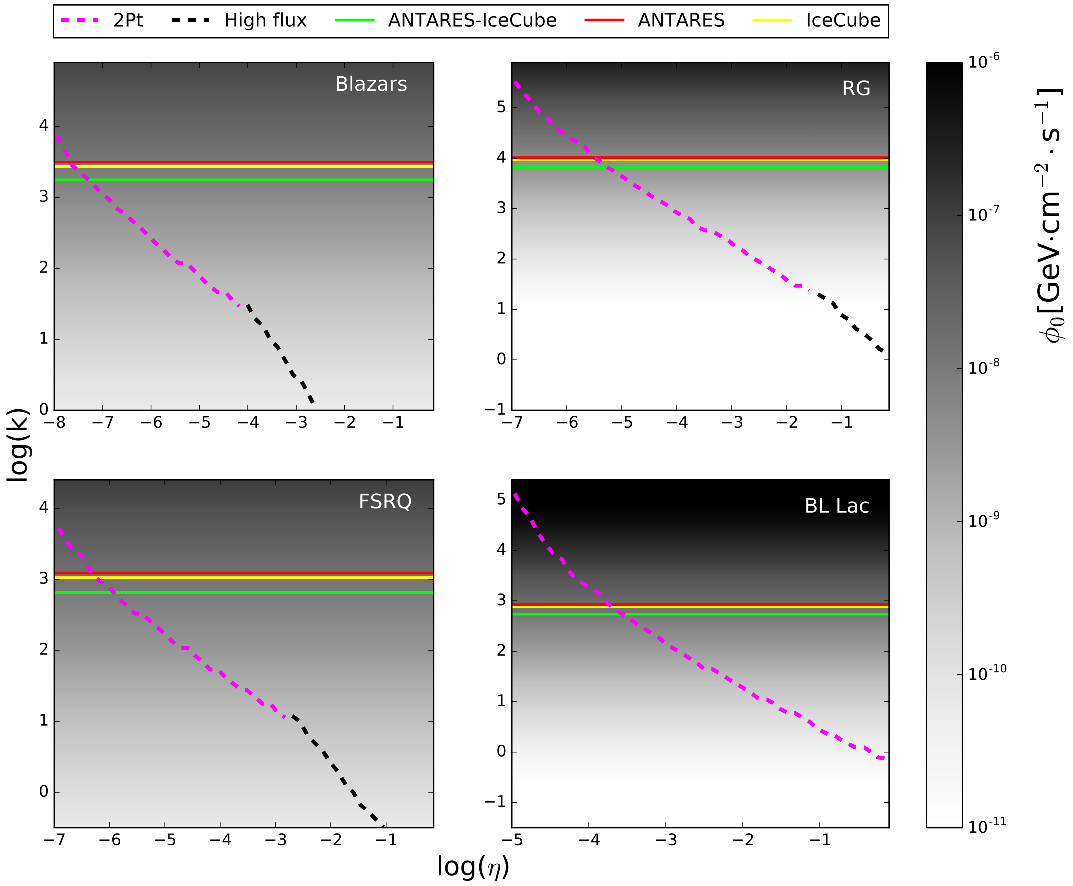

Figure 9.5: 90 $\%$ confidence level upper limits set on the phase space (η, k) for the different classes of AGN. The magenta line shows the limits set by the 2 point correlation analysis. The gray color scale represents the mean flux per source for each point in the parameter space, and the colored lines show the limits to a point source flux set by IceCube and ANTARES. The black dashed line, shows the boundary of the region where a too high number of neutrinos would be detected by ANTARES, which in this work is consireded to be excluded.

The comparison of these limits with the limits calculated here with the 2 point correlation analysis, confirms some of the results shown in reference [10], where it is shown that the likelihood based search is more sensitive to a single point source than the 2 point correlation analysis. This is reflected in the limits for the lowest values of the parameter η, which are less stringent for the 2 point correlation analysis. In addition, this plot also shows that the

2 point correlation analysis provides with much better limits for a point source flux, when populations of weak point sources are considered.

9.5 Conclusions

In this last part, the 2 point correlation analysis has been presented in chapter 7 and its discovery power has been tested under different configurations and for different types of sources. Since this method is able to detect an excess of anisotropies produced by sources of different morphologies, it has been used to search for neutrinos produced by populations of AGN. In chapter 8, a method has been developed to simulate fake data samples containing neutrinos produced by populations of AGN. This method is based on observations of AGN in the X-ray band of the electromagnetic spectrum, and relies on the definition of two parameters related to the physics of AGN. The parameter k defines the ratio between the neutrino and X-ray luminosity of AGN, and the parameter η which defines the fraction of AGN, which emitting X-rays, also emit neutrinos.

By using the 2 point correlation analysis, the discovery power of the ANTARES neutrino telescope has been studied for different values of these two parameters and for different AGN classes. The absence of a statistically significant departure from background in the ANTARES 2007-2012 data set has allowed to constrain the space defined by η and k for each AGN class. In addition, these results also show the complementarity of the 2 point correlation analysis and the standard likelihood based search for point sources: while the latter is more sensitive to a single point source, the former is sensitive to collective effects.

Acknowledgements

Doing this thesis wouldn't have been possible without the help of many people who I want to thank.

First, I want to thank my advisor Antoine Kouchner, and my coadvisor Bruny Baret for accepting me as their student. Their contribution to my work during these three years has been really important. Besides giving me the opportunity of going to the APC and doing my PhD with him and his working group, Antoine started helping me even before I signed my contract, by searching for me a place where to live in Paris. He didn't just manage to get me a room in Cité Universitaire (where I had a really good time), but also came with me to visit it, and helped me to deal with all the administrative issues. Gestures like this are very difficult to forget and I'm really thankful for them, but Antoine's help does not end there. During this period I've also had his constant and unconditional support both in the personal and in the academical sides, and this support became particularly important for me during the last and toughest months of my PhD. During my last summer in Paris, when I was working alone in the lab and I had almost no contact with anybody, Antoine was always ready to discuss with me either by mail, by phone or by video conference. Being on holidays, he used to check on me almost every day and that was really helpful. Without his help, I wouldn't have been able to write this thesis, and without his advice I wouldn't have been able to produce the work described here. For reasons like these, I'm really happy that I had Antoine as my PhD advisor. Thanks to a continuous interaction with Bruny at the beginning of my thesis, I learned how to use the tools that are required to work on experimental particle physics, as well as the specific technicalities related to neutrino astrophysics and ANTARES. This happened after many hours of sitting together in front of my computer, during which, I know, that Bruny also learned very useful things for his daily life such as typing English with a French keyboard configured to write as a Spanish one. Besides learning from him the most technical stuff, Bruny's help was fundamental for me to develop the different parts of my thesis, but without any doubt, the most important think I've learned from Bruny is how one should not play darts. I also want to thank Bruny for the amount of time we shared together drinking tea in the lab and beer outside the lab, during which, he became a good friend.

Another person who I want to thank is Véronique van Elewyck, for taking care of me when I first arrived at the APC. Vero helped me to open a bank account, to inscribe to the University, and to look for French courses. When I arrived to Paris I didn't speak a single word of French, and those courses helped me to start learning something, but there is nothing as useful as a language immersion program to really learn a language. I had the pleasure of following such an immersion with Vero as a teacher in La Seyne-sur-Mer during our ANTARES shift. Although the conversations there were the most ridiculous conversations that one can imagine, my french level really improved there, and that allowed me to have a more comfortable life in Paris. I also thank Vero for taking me out to have fun in Paris, and for the nice time that we spent in Japan during the TeVPa conference. And of course, I thank her for her comments about the manuscript, that helped me to improve this work.

Colleagues are important when one starts a new job, and colleagues are even more important if one arrives to a new city without knowing anybody, like it was my case when I arrived to Paris. I was very lucky that one of the first people who I worked with was Alexandre Creusot. Since I arrived at the APC Alex treated me as a friend, and that was a priceless sensation. I have very good memories from my first ANTARES collaboration meetings, where I shared a lot of time with him, and also of the uncountable Friday afternoons that we spent having beers next to the lab after work. Even though our plan for playing role games was not successful, I still believe that one day we will play!

Other very important colleagues that one usually finds in a job are the office mates. In my case, I've had the pleasure of sharing my office for a long time with two very good friends, Alexis Coleiro and Salvatore Galatà. Both of them have helped me a lot during this time. Having Salvo working in front of me was really important because he attended me every time I had an issue, and his constant help made my work to progress a lot. He has been interested on my work and on my progress even after his contract finished. During this time we didn't just share the office, but also the cantine and trips to collaboration meetings and conferences. All this time together has brought too many good and funny moments, some of which can be represented by a set of keywords: Salvo, If you're reading this, I want to thank you for things like: *echo $PATH, bon appetit et bonne journee, let's have a tea, LD_LIBRARY_PATH, the water is on the table, guillotine, hedgewars, riz du jour, lipton, segmentation fault, lotelito, mayflower, ROOT, PYTHONPATH, oolong, let's go to eat, qstats, enjoy your breakfast, biopark, Bouvier*. Alexis has also been really important during these years. He always showed interest on my work and gave me advice whenever I needed it. Until the very end of my PhD, he has been supporting me and I'm really thankful for that. Thanks to talking with him everyday, my level of French improved a lot. By working together, we managed to produce nice things such as fancy plots showing the ANTARES visibility, but without any doubt, our greatest contribution to science was to protect every member from the APC laboratory from a biological weapon located in our office: After a big effort we managed to empty and disinfect a fridge that didn't just contain plenty of yogurts which "best before" date had passed at least 6 years before, but which also contained several kilograms of butter distributed in many small (and opened) packs, rotten lemons covered by a green layer of mushrooms, as well as several other kinds of organic matter which advanced decomposition stage made it impossible to identify them with any known kind of food. Unfortunately there is something that we didn't manage to do: despite of all the efforts from Alexis, Salvo and I, we never managed to grow a single plant in our office. The only thing we grew instead, was a colony of soil flies that stayed flying in our office and annoying us until they became extinct, thanks, in part, to Bruny's technological inventions. Even if there's no future for us as gardeners, we've had a lot fun and I've learned many things related to physics with you. Thanks for everything.

I also want to thank Etienne Parizot for his contribution to my thesis. Discussing with him has been fundamental for the development of the physics analysis described in the last chapters of this work, and also to deal with some unexpected issues that arose near the end of the PhD. I appreciate him a lot for his interest on my work, for his great ideas, and for attending me always with a smile. It has been a privilege to work with him.

The other member of my thesis committee was Fabian Schussler, who also gave me valuable advice during these three years. In addition to that, his previous work was the starting point of my work, and his explanations at the beginning were helpful for me to reproduce his results. As a member of the ANTARES collaboration, he has also been the referee of my physics analysis and his comments and ideas have contributed as well to the final results.

From the ANTARES collaboration, I also want to thank Annarita Margiotta and Dorothea Samtleben who are the respective coordinators of the Monte Carlo and of the point source search working groups of the ANTARES collaboration, where I've developed my work. I thank both of them for their constant help, interest and support. It has been a pleasure to work with them. Additionally, I want to thank Annarita for being referee of this work (it was a pity that she couldn't attend the public defence)and Dorothea, for accepting being a member of the jury in the defence of this work.

Other members of the ANTARES collaboration with who I've interacted during these years, and whose names I wish to highlight here are Clancy James, Thomas Eberl, and Maurizio Spurio. I want to thank them for their time, and for sharing with me their knowledge and experience.

I also want to write a few words about the rest of the members of the ANTARES group in the APC laboratory. Cyril Lachaud has been a good friend, and he has always given good advice to me. Thanks Cyril. I also want to thank for their friendship during this time to Corinne Donzaud and Bertrand Vallage, who I met during my first days in the lab, and who have also made very useful comments about my work in our group meetings. It has been a pleasure to meet and discuss with Joao Coelho who has also given me very useful comments. Besides becoming a friend, his cross checks have been fundamental to confirm that I was on the correct path and that sometimes, science hides more secrets than it appears... Thank you Joao! Thanks as well to the other PhD students in the group, Simon Bourret, Theodore

Avgitas, and Thimothée Gregoire for the time that we've shared together. I wish you the best for the rest of your theses! Finally, I want to thank Julien Aublin for his collaboration during the final sprint of my thesis. Even if he became a member of the group almost when I finished my thesis and we didn't spend much time together, I know that he would have been a great office mate! Thanks Julien! Although they are not members from the ANTARES group, I also want to thank my corridor mates in the lab, Sabine Tesson, Martine Laird-Bardissa and Denis Allard for making the work environment such a nice and friendly place. Thanks to Denis also for answering my questions about cosmic rays!

Thanks as well to the other members of the jury, Isabelle L'Henry-Yvon, and Juan Antonio Aguilar. Isabelle was referee of my thesis, and I thank her for her careful reading of the manuscript and for her report. Juanan's comments were very useful to finalize this manuscript. Thank you both!

And, of course, I want to thank my mom Rosa Ruiz, for all the efforts that she has always made for me.

Bibliography

[1] The ANTARES Neutrino Telescope : Contributions to the 34th International Cosmic Ray Conference (ICRC 2015, The Hague). In *Proceedings, 34th International Cosmic Ray Conference (ICRC 2015): The Hague, The Netherlands, July 30-August 6, 2015*, 2015.

[2] *The Pierre Auger Observatory: Contributions to the 34th International Cosmic Ray Conference (ICRC 2015)*, 2015.

[3] M. G. Aartsen et al. Evidence for High-Energy Extraterrestrial Neutrinos at the IceCube Detector. *Science*, 342:1242856, 2013.

[4] M. G. Aartsen et al. First observation of PeV-energy neutrinos with IceCube. *Phys. Rev. Lett.*, 111:021103, 2013.

[5] M. G. Aartsen et al. IceCube-Gen2: A Vision for the Future of Neutrino Astronomy in Antarctica. 2014.

[6] M. G. Aartsen et al. Observation of High-Energy Astrophysical Neutrinos in Three Years of IceCube Data. *Phys. Rev. Lett.*, 113:101101, 2014.

[7] M. et al. Ackermann. The Third Catalog of Active Galactic Nuclei Detected by the Fermi Large Area Telescope. *apj*, 810:14, September 2015.

[8] S. Adrian-Martinez et al. Search for Cosmic Neutrino Point Sources with Four Year Data of the ANTARES Telescope. *Astrophys. J.*, 760:53, 2012.

[9] S. Adrian-Martinez et al. The Positioning System of the ANTARES Neutrino Telescope. *JINST*, 7:T08002, 2012.

[10] S. Adrian-Martinez et al. Searches for clustering in the time integrated skymap of the ANTARES neutrino telescope. *JCAP*, 1405:001, 2014.

[11] S. Adrian-Martinez et al. Searches for Point-like and extended neutrino sources close to the Galactic Centre using the ANTARES neutrino Telescope. *Astrophys. J.*, 786:L5, 2014.

[12] S. Adrian-Martinez et al. High-energy Neutrino follow-up search of Gravitational Wave Event GW150914 with ANTARES and IceCube. *Phys. Rev.*, D93(12):122010, 2016.

[13] S. Adrián-Martínez et al. ANTARES Constrains a Blazar Origin of Two IceCube PeV Neutrino Events. *Astron. Astrophys.*, 576:L8, 2015.

[14] M. Ageron et al. ANTARES: the first undersea neutrino telescope. *Nucl. Instrum. Meth.*, A656:11–38, 2011.

[15] J. A. Aguilar et al. Performance of the front-end electronics of the ANTARES neutrino telescope. *Nucl. Instrum. Meth.*, A622:59–73, 2010.

[16] J. A. Aguilar et al. Time Calibration of the ANTARES Neutrino Telescope. *Astropart. Phys.*, 34:539–549, 2011.

[17] S. P. Ahlen et al. Arrival time distributions of very high-energy cosmic ray muons in MACRO. *Nucl. Phys.*, B370:432–444, 1992.

[18] M. Ajello et al. The Evolution of Swift/BAT blazars and the origin of the MeV background. *Astrophys. J.*, 699:603–625, 2009.

[19] A.Morel. *Optical properties of pure water and pure sea water*. Academic Press, 1974.

[20] P. Antonioli, C. Ghetti, E. V. Korolkova, V. A. Kudryavtsev, and G. Sartorelli. A Three-dimensional code for muon propagation through the rock: Music. *Astropart. Phys.*, 7:357–368, 1997.

[21] V. Aynutdinov et al. The BAIKAL neutrino experiment: Physics results and perspectives. *Nucl. Instrum. Meth.*, A602:14–20, 2009.

[22] John N. Bahcall. Solar models and solar neutrinos: Current status. *Phys. Scripta*, T121:46–50, 2005.

[23] David J L Bailey. Calculation of effective muon ranges and application to overall effective areas. 2001.

[24] David J L Bailey. Computation of maximum and effective muon ranges. 2002.

[25] David J L Bailey. Genhen v5r1 : Software Documentation. 2002.

[26] Paul H. Barrett, Lowell M. Bollinger, Giuseppe Cocconi, Yehuda Eisenberg, and Kenneth Greisen. Interpretation of cosmic-ray measurements far underground. *Rev. Mod. Phys.*, 24:133–178, Jul 1952.

[27] John F. Beacom, Patrick Crotty, and Edward W. Kolb. Enhanced signal of astrophysical tau neutrinos propagating through earth. *Phys. Rev. D*, 66:021302, Jul 2002.

[28] Y. Becherini, A. Margiotta, M. Sioli, and M. Spurio. A parameterisation of single and multiple muons in the deep water or ice. *Astroparticle Physics*, 25(1):1 – 13, 2006.

[29] Julia K. Becker. High-energy neutrinos in the context of multimessenger physics. *Phys. Rept.*, 458:173–246, 2008.

[30] Julia K. Becker and Peter L. Biermann. Neutrinos from active black holes, sources of ultra high energy cosmic rays. *Astropart. Phys.*, 31:138–148, 2009.

[31] V. Beckmann and C. Shrader. *Active Galactic Nuclei*. Physics textbook. Wiley, 2012.

[32] Christoph Berger et al. Experimental Study of Muon Bundles Observed in the Frejus Detector. *Phys. Rev.*, D40:2163, 1989.

[33] P. Binétruy. Cosmology and Gravitation: the grand scheme for High-Energy Physics. In *Proceedings, 2012 European School of High-Energy Physics (ESHEP 2012): La Pommeraye, Anjou, France, June 06-19, 2012*, pages 217–291, 2014.

[34] R. Boissay, S. Paltani, and C. Ricci. A hard X-ray view of the soft-excess in AGN. In *The Extremes of Black Hole Accretion*, page 74, July 2015.

[35] G. Carminati, M. Bazzotti, S. Biagi, S. Cecchini, T. Chiarusi, A. Margiotta, M. Sioli, and M. Spurio. MUPAGE: a fast atmospheric MUon GEnerator for neutrino telescopes based on PArametric formulas. 2009.

[36] R. Chini, E. Kreysa, and P. L. Biermann. The nature of radio-quiet quasars. *Astron. Astrophys.*, 219:87–97, July 1989.

[37] D. Chirkin and W. Rhode. All lepton propagation Monte Carlo. In *29th International Cosmic Ray Conference (ICRC 2005) Pune, India, August 3-11, 2005*, 2005.

[38] Dmitry Chirkin and Wolfgang Rhode. Muon Monte Carlo: A High-precision tool for muon propagation through matter. 2004.

[39] C.Mobley. *Light and Water: Radiative Transfer in Natural Waters*. Academic Press, 1994.

[40] ANTARES Collaboration. Contributions to the 33st International Cosmic Ray Conference (ICRC 2013, Rio de Janeiro). In *Proceedings, 33rd International Cosmic Ray Conference (ICRC2013): Rio de Janeiro, Brazil, July 2-9, 2013*, 2013.

[41] M Dentler. Investigation of the One-Particle Approximation in the Antares simulation package km3. Nov 2012.

[42] M. D'Onofrio, P. Marziani, and J.W. Sulentic. *Fifty Years of Quasars: From Early Observations and Ideas to Future Research*. Astrophysics and Space Science Library. Springer, 2012.

[43] A. Einstein. Theorie der Opaleszenz von homogenen Flussigkeiten und Flussigkeitsgemischen in der Nähe des kritischen Zustandes. *Ann. d. Phys*, 338:1275–1298, 1910.

[44] M. Elvis, T. Maccacaro, A. S. Wilson, M. J. Ward, M. V. Penston, R. A. E. Fosbury, and G. C. Perola. Seyfert galaxies as X-ray sources. *MNRAS*, 183:129–157, April 1978.

[45] C. Tamburini et. al. Deep-Sea Bioluminescence Blooms after Dense Water Formation at the Ocean Surface. *PLOS*, 8:–, 2013.

[46] E. Fermi. On the origin of the cosmic radiation. *Phys. Rev.*, 75:1169–1174, Apr 1949.

[47] Ronald Fisher. *Statistical methods for research workers*. Oliver and Boyd, Edinburgh, 1970.

[48] C. Forti, H. Bilokon, B. d'Ettore Piazzoli, T. K. Gaisser, L. Satta, and T. Stanev. Simulation of atmospheric cascades and deep underground muons. *Phys. Rev.*, D42:3668–3689, 1990.

[49] Raj Gandhi, Chris Quigg, Mary Hall Reno, and Ina Sarcevic. Neutrino interactions at ultrahigh energies. *Phys. Rev. D*, 58:093009, Sep 1998.

[50] Carlo Giunti. Neutrino Flavor States and Oscillations. *J. Phys.*, G34:R93–R109, 2007.

[51] Noemie Globus, Denis Allard, and Etienne Parizot. A complete model of the cosmic ray spectrum and composition across the Galactic to extragalactic transition. *Phys. Rev.*, D92(2):021302, 2015.

[52] Kenneth Greisen. End to the cosmic ray spectrum? *Phys. Rev. Lett.*, 16:748–750, 1966.

[53] Mukund Gupta. Calculation of radiation length in materials. Technical Report PH-EP-Tech-Note-2010-013, CERN, Geneva, Jul 2010.

[54] Aart Heijboer. *Track reconstruction and point source searches with ANTARES*. PhD thesis, Amsterdam U., 2004.

[55] A. M. Hillas. The Origin of Ultrahigh-Energy Cosmic Rays. *Ann. Rev. Astron. Astrophys.*, 22:425–444, 1984.

[56] S. Hony et al. The Spitzer discovery of a galaxy with infrared emission solely due to AGN activity. *Astron. Astrophys.*, 531:A137, 2011.

[57] D. et al Horns. Nucleonic gamma-ray production in vela x. *A and A*, 451:51–54, jun 2006.

[58] G. Ingelman, A. Edin, and J. Rathsman. LEPTO 6.5: A Monte Carlo generator for deep inelastic lepton - nucleon scattering. *Comput. Phys. Commun.*, 101:108–134, 1997.

[59] Idunn B. Jacobsen, Kinwah Wu, Alvina Y. L. On, and Curtis J. Saxton. High-energy neutrino fluxes from AGN populations inferred from X-ray surveys. *Mon. Not. Roy. Astron. Soc.*, 451(4):3649–3663, 2015.

[60] Hylke B. J. Koers and Peter Tinyakov. Relation between the neutrino flux from Centaurus A and the associated diffuse neutrino flux. *Phys. Rev.*, D78:083009, 2008.

[61] O.V. Koplevich. Small-parameter model of optical properties of sea water. *Ocean Optics*, 19, 1983.

[62] V. Kulikovskiy. *Neutrino Astrophysics with the ANTARES Telescope*. Theses. Springer Theses, 2015.

[63] Annalisa Labbate, Teresa Montaruli, and Igor A Sokalski. GENHEN v6: ANTARES neutrino generator extension to all neutrino flavors and inclusion of propagation through the Earth. 2004.

[64] P. Lipari and T. Stanev. Propagation of multi - TeV muons. *Phys. Rev.*, D44:3543–3554, 1991.

[65] Abraham Loeb and Eli Waxman. The Cumulative background of high energy neutrinos from starburst galaxies. *JCAP*, 0605:003, 2006.

[66] A. Marcowith, G. Henri, and G. Pelletier. Gamma-ray emission of blazars by a relativistic electron-positron beam. *mnras*, 277:681–699, November 1995.

[67] H. L. Marshall, H. Tananbaum, Y. Avni, and G. Zamorani. Analysis of complete quasar samples to obtain parameters of luminosity and evolution functions. *Astrophys. J.*, 269:35–41, June 1983.

[68] I. F. Mirabel and L. F. Rodriguez. A Superluminal source in the galaxy. *Nature*, 371:46–48, 1994.

[69] Andrii Neronov and Dmitry Semikoz. Neutrinos from Extra-Large Hadron Collider in the Milky Way. *Astropart. Phys.*, 72:32–37, 2016.

[70] H. Netzer. *The Physics and Evolution of Active Galactic Nuclei*. Cambridge University Press, 2013.

[71] J. Neyman and E. S. Pearson. On the problem of the most efficient tests of statistical hypotheses. *Philosophical Transactions of the Royal Society of London A: Mathematical, Physical and Engineering Sciences*, 231(694-706):289–337, 1933.

[72] K. A. Olive et al. Review of Particle Physics. *Chin. Phys.*, C38:090001, 2014.

[73] T. Petzold. Volume Scattering Functions for Selected Ocean Waters. *Scripps Inst. Oceanogr*, 1972.

[74] Thierry Pradier. Coincidences between Gravitational Wave Interferometers and High Energy Neutrino Telescopes. *Nucl. Instrum. Meth.*, A602:268–274, 2009.

[75] P. Buford Price. Implications of optical properties of ocean, lake, and ice for ultrahigh-energy neutrino detection. *Appl. Opt.*, 36(9):1965–1975, Mar 1997.

[76] Georg G. Raffelt. Supernova neutrino oscillations. *Phys. Scripta*, T121:102–105, 2005.

[77] Soebur Razzaque, Peter Meszaros, and Eli Waxman. Neutrino tomography of gamma-ray bursts and massive stellar collapses. *Phys. Rev.*, D68:083001, 2003.

[78] C. S. Reynolds. Compton Reflection and Iron Fluorescence in Active Galactic Nuclei and Galactic Black Hole Candidates. In J. Poutanen and R. Svensson, editors, *High Energy Processes in Accreting Black Holes*, volume 161 of *Astronomical Society of the Pacific Conference Series*, page 178, 1999.

[79] Claudio Ricci. Active galactic nuclei at hard x-ray energies: absorption, reflection and the unified model, 12/08 2011. ID: unige:19474.

[80] Alfred Weigert Rudolf Kippenhahn. *Stellar Structure and Evolution*. Astronomy and Astrophysics Library. Springer, 1996.

[81] Eugenio Scapparone. HEMAS: A Monte Carlo code for hadronic, electromagnetic and TeV muon components in air shower. In *Simulation and analysis methods for large neutrino telescopes. Proceedings, Workshop, Zeuthen, Germany, July 6-9, 1998*, pages 238–246, 1998.

[82] P. Schneider. *Extragalactic Astronomy and Cosmology: An Introduction*. SpringerLink : Bücher. Springer Berlin Heidelberg, 2014.

[83] Stefan Schonert, Thomas K. Gaisser, Elisa Resconi, and Olaf Schulz. Vetoing atmospheric neutrinos in a high energy neutrino telescope. *Phys. Rev.*, D79:043009, 2009.

[84] J. D. Silverman et al. The Luminosity Function of X-ray Selected Active Galactic Nuclei: Evolution of Supermassive Black Holes at High Redshift. *Astrophys. J.*, 679:118, 2008.

[85] M. Smoluchowski. Molekular-kinetische Theorie der Opaleszenz von Gasen im kritischen Zustande, sowie einiger verwandter Erscheinungen. *Ann. d. Phys*, 330:205–226, 1908.

[86] M. Spurio. Constraints to a Galactic Component of the Ice Cube cosmic neutrino flux from ANTARES. *Phys. Rev.*, D90(10):103004, 2014.

[87] M. Spurio. *Particles and Astrophysics: A Multi-Messenger Approach*. Astronomy and Astrophysics Library. Springer International Publishing, 2014.

[88] F. W. Stecker, C. Done, M. H. Salamon, and P. Sommers. High-energy neutrinos from active galactic nuclei. *Phys. Rev. Lett.*, 66:2697–2700, 1991. [Erratum: Phys. Rev. Lett.69,2738(1992)].

[89] F. W. Stecker, C. Done, M. H. Salamon, and P. Sommers. Erratum: "high-energy neutrinos from active galactic nuclei" [phys. rev. lett. **66** , 2697 (1991)]. *Phys. Rev. Lett.*, 69:2738–2738, Nov 1992.

[90] L. Titarchuk and Y. Lyubarskij. Power-Law Spectra as a Result of Comptonization of the Soft Radiation in a Plasma Cloud. *Astrophysical Journal*, 450:876, September 1995.

[91] W. J. Tomlinson and C. Lin. Optical wavelength-division multiplexer for the 1-1.4-micron spectral region. *Electronics Letters*, 14:345–347, May 1978.

[92] Y. Ueda, M. Akiyama, K. Ohta, and T. Miyaji. Cosmological Evolution of the Hard X-Ray Active Galactic Nucleus Luminosity Function and the Origin of the Hard X-Ray Background. *Astrophys. J.*, 598:886–908, December 2003.

[93] C. Megan Urry. AGN unification: An Update. *ASP Conf. Ser.*, 311:49, 2004.

[94] C. Megan Urry and Paolo Padovani. Unified schemes for radio-loud active galactic nuclei. *Publ. Astron. Soc. Pac.*, 107:803, 1995.

[95] Zbigniew Was. TAUOLA for simulation of tau decay and production: perspectives for precision low energy and LHC applications. *Nucl. Phys. Proc. Suppl.*, 218:249–255, 2011.

[96] Eli Waxman and John N. Bahcall. High-energy neutrinos from cosmological gamma-ray burst fireballs. *Phys. Rev. Lett.*, 78:2292–2295, 1997.

[97] Eli Waxman and John N. Bahcall. High-energy neutrinos from astrophysical sources: An Upper bound. *Phys. Rev.*, D59:023002, 1999.

[98] Eli Waxman and John N. Bahcall. Neutrino afterglow from gamma-ray bursts: Similar to 10**18-eV. *Astrophys. J.*, 541:707–711, 2000.

[99] B. Wilkes. Spectral Energy Distributions of Quasars and AGN. In G. T. Richards and P. B. Hall, editors, *AGN Physics with the Sloan Digital Sky Survey*, volume 311 of *Astronomical Society of the Pacific Conference Series*, page 37, June 2004.

[100] G. T. Zatsepin and V. A. Kuzmin. Upper limit of the spectrum of cosmic rays. *JETP Lett.*, 4:78–80, 1966. [Pisma Zh. Eksp. Teor. Fiz.4,114(1966)].

[101] Christian Zier and Peter L. Biermann. Binary black holes and tori in AGN. 2. Can stellar winds constitute a dusty torus? *Astron. Astrophys.*, 396:91–108, 2002.